Highly doubly excited states of helium under periodic driving and the formation of nondispersive wave packets

Alejandro González Melan

July 3, 2018

Universidad del Valle
Facultad de Ciencias Naturales y Exactas
Physics Department

Highly doubly excited states of helium under periodic driving and the formation of nondispersive wave packets



Alejandro González Melan

Advisor
Javier Madroñero Pabón
Dr. Rer. Nat.

Submitted in part fulfilment of the requirements
for the degree of Doctor en Ciencias - Física
Cali, July 3, 2018

a mi madre y a mi esposa

Abstract

We provide a full characterization of two-electron nondispersive wave packets found in the Floquet spectrum of driven helium. These quantum objects which propagate along periodic trajectories of the classical three-body Coulomb problem without dispersion have been identified early within large numerical calculations on one- and two-dimensional models.

In this thesis, we present an efficient treatment to describe the dynamics of doubly excited states of helium under electromagnetic driving. With this approach, we are able to identify the resonance states of helium that play the fundamental role in the formation of these nondispersive wave packets, which allows us to give for the first time, theoretical evidence of their existence in three-dimensional helium.

Furthermore, we compute the entanglement of doubly excited states of planar helium. We also discuss the effect of a periodic driving by an external field on entanglement. In particular, we focus on the entanglement of two-electron nondispersive wave packets.

Resumen

Presentamos una completa caracterización de los paquetes de onda no dispersivos de dos electrones encontrados en el espectro de Floquet para el átomo de helio. Estos objetos cuánticos que se propagan sin dispersión a lo largo de trayectorias periódicas del problema coulombiano clásico de tres cuerpos, han sido identificados anteriormente empleando grandes cálculos numéricos en modelos de una y dos dimensiones.

En esta tesis presentamos un método eficiente para describir la dinámica de estados doblemente excitados de helio forzado por un campo electromagnético. Con este enfoque podemos identificar los estados resonantes de helio que juegan un papel fundamental en la formación de estos paquetes de onda no dispersivos, lo cual nos permite dar por primera vez evidencia teórica de su existencia en helio tres dimensional.

Adicionalmente, calculamos el entrelazamiento en estados doblemente excitados de helio planar. También discutimos el efecto que tiene sobre el entrelazamiento un forzamiento periódico externo. En particular nos enfocamos en el entrelazamiento en paquetes de onda no dispersivos.

Contents

1 Introduction **1**

2 Theoretical and numerical framework **5**

2.1 Generalities 5

2.1.1 Hamiltonian 5

2.1.2 Spectral properties of helium 6

2.1.3 Complex rotation method 8

2.2 Planar treatment of the two-electron atom 10

2.2.1 Regularization of the 2D helium Hamiltonian 10

2.2.2 Matrix representation 12

2.2.3 Construction of the basis 12

2.2.4 Convergence of the method 13

2.3 Three-dimensional two-electron atom model 16

2.3.1 Expansion for the wave function 16

2.3.2 Matrix representation 18

2.3.3 Convergence of the method 19

2.4 Helium atom under periodic driving 21

2.4.1 Floquet theory 21

2.4.2 Numerical treatment 22

2.5 Quantum entanglement in helium 24

2.5.1 Entanglement measure 25

3 Frozen planet states of helium **27**

3.1 Classical frozen planet configuration 27

3.2 Frozen planet states of 2D and 3D helium 29

4 Nondispersive wave packets (NDWP) in helium **37**

4.1 Driven frozen planet configuration 37

4.2 Nondispersive wave packets in 2D helium 38

4.2.1 Identification of NDWP below the 6th ionization threshold 38

4.2.2 Principal characteristics of NDWP below the 6th ionization threshold 40

4.2.3 Basic ingredients in the formation of NDWP 46
4.2.4 Identification of NDWP below other ionization thresholds 49
4.3 Nondispersive wave packets in 3D helium 51
4.3.1 Some comments on the experimental identification of NDWP . . 54

5 Quantum entanglement in planar helium **57**
5.1 Entanglement in bound and doubly excited states 57
5.2 Quantum entanglement in NDWP 60

6 Summary and outlook **67**
6.1 Summary 67
6.2 Outlook 68

A Appendix **69**
A.1 Lanczos algorithm 69
A.2 Electronic density in configuration space 70
A.3 Husimi distributions 72
A.4 Expectation value of $\cos\theta_{12}$ 72

B Appendix **73**
B.1 Unnatural parity states 73
B.2 Oscillator strengths 73

Bibliography **85**

1 Introduction

The correlated electron dynamics, that plays an important role in non-equilibrium processes in atomic [1,2], molecular [3–5] and solid state physics [6–8], has awaked the interest of the scientific community in controlling the electronic dynamics [9,10]. This is not an easy task since the dynamical processes in the atomic and molecular world occur very fast. For instance, the time it takes an electron in the hydrogen atom to complete the shortest orbit is 152 as. Current advances in this direction are surprising: it is possible, e.g., to image the motion of the two electrons in the helium atom and even to control its dynamics with the help of attosecond pulses [11]. Nevertheless, further advances require a better understanding of the electronic dynamics in the quantum regime, and the physics of few-electron atoms interacting with electromagnetic fields has attracted large experimental and theoretical attention. In this regard, the interaction of light with the helium atom is of special interest, because, despite being the simplest example for a multi-electron atom, its dynamics is nonintegrable even from the classical point of view [12].

The helium atom is a three-body problem with gravitational forces replaced by attractive and repulsive Coulomb interactions. The classical dynamics of helium is in general irregular and chaotic with only small regions of regular motion in phase space [13] which implies the destruction of good quantum numbers in the quantum description [14] and a chaotic structure of the spectrum. The loss of integrability, due to the electron-electron interaction, caused that the application of Bohr's quantization postulates to the helium atom in the early days of quantum mechanics could not succeed [12,15,16]. Only with the development of modern semiclassical methods in the second half of the 20th century [17,18] and the subsequent semiclassical quantization of helium [19–21], the relation between the non-integrability of the quantum system and the classical mixed regular-chaotic dynamics was established [14]. Up to date, various theoretical investigations have improved our understanding of two-electron atoms ranging from semiclassical (see [14] for a review) to quantum mechanics including relativistic corrections [11,22–29].

Since the first experiment by Madden and Codling in 1963 [30], where doubly excited states of two-electron atoms have been identified as highly correlated states that cannot be in general described by a simple model based on independent-particle quantum numbers, doubly and highly excited states of helium have attracted the interest of theoreticians and experimentalists. Particularly, the energy regime near the total fragmentation threshold represents a paradigm for electronic correlations in atomic

physics. In this regime —which is indeed the semiclassical one in two-electron atoms— the underlying classical chaotic dynamics should influence the quantum spectrum of highly doubly excited states, manifested as semiclassical scaling laws for the fluctuations of excitation cross sections [31] or signatures of quantum chaos such as Ericson fluctuations [32, 33].

Strong electronic correlations are found in highly asymmetrically doubly excited states of helium which are associated with the highly correlated classical frozen planet configuration [34,35]. Theoretical studies for one-dimensional [36,37] and planar helium [38,39] suggest that under near-resonantly periodic driving these states transform into two-electron nondispersive wave packets (NDWP) [40]. However, until now, no evidence of the existence of these objects has been found in full three-dimensional calculations.

A clear understanding of the dynamics of driven helium represents a theoretical and numerical challenge. Nevertheless, current advances in ultrafast molecular probing, attosecond science, and extreme-ultraviolet nonlinear optics [41–43] have motivated the development of many theoretical methods to describe the electronic dynamics in atoms, molecules and solids driven by laser pulses (see [44] for a review). Numerical simulations of the electronic dynamics require the solution of the time-dependent Schrödinger equation (TDSE). This is easily achieved within the single-active electron approximation [45, 46], where only a single electron is studied and the influence of the others is represented by an effective potential. However, when two or more electrons are involved in the dynamics and their correlations are taken into consideration, this becomes a computational challenge.

For the direct numerical integration of the TDSE, there are two principal approaches that provide an exact description for the case of He, H_2, and Li: The grid or time-dependent close-coupling method [47–51] and the spectral method [23,52–56]. In the grid method, the angular part of the wave function is expanded in bipolar spherical harmonics [57] and then substituted into the TDSE to derive a set of coupled partial differential equations called the time-dependent close-coupling equations, which are solved by discretization of the radial wave function on a finite-difference grid. On the other hand, the spectral method consists of two steps. First, the atomic Hamiltonian is diagonalized in a basis of products of radial one-electron functions and bipolar spherical harmonics, where, the radial functions can be for instance Coulomb-Sturmian functions [58, 59] or B-splines functions [60, 61]. Then, the total wave function is expanded in terms of field-free eigenstates and inserted into the TDSE to obtain a set of coupled first-order ordinary differential equations for the temporal evolution of the expansion coefficients. The extension of the above methods to more than two electrons is extremely problematic due to the exponential increase in computational cost and theoretical complexity. Thus, the

description of multi-electron dynamics requires the use of alternative methods like the multiconfiguration time-dependent Hartree-Fock method [62], or the time-dependent multiconfiguration self-consistent-field method [63–67].

In the present thesis, we are going to investigate the dynamics of driven doubly excited states of helium and the formation of nondispersive wave packets. We will present an efficient numerical treatment of driven helium which allows us to characterize NDWP in planar helium and to give for the first time, theoretical evidence for the existence of two-electron NDWP in three-dimensional helium. In addition, we are going to characterize the electronic correlations in terms of entanglement properties of doubly excited states of helium and the FPS which can lead to the formation of nondispersive wave packets.

In our approach to solve the TDSE describing the dynamics of a two-electron atom interacting with a periodic electromagnetic field, we use a spectral method combined with Floquet theory [68, 69]. The method is based on the solution of the TDSE in a basis set composed of eigenstates of the unperturbed Hamiltonian. The diagonalization of the atomic Hamiltonian in the planar case is achieved within the *ab initio* method described in [38, 39] which gives an accurate description of the system combining complex dilation, and the representation of the Hamiltonian in suitably chosen coordinates without adjustable parameters. For the unperturbed three-dimensional helium atom, the two-electron wave function is expanded in a configuration interaction (CI) basis [25, 70, 71] where the radial one electron functions are Coulomb-Sturmian functions with different nonlinear parameters for the description of each electron. This allows us to perform an efficient description of asymmetrically excited states, e.g., the frozen planet states, in a relatively small basis compare to standard CI approaches.

One of the advantages of this method for the investigation of driven helium is the significant reduction of the size of the matrices involved in the computations. Additionally but not less important is the possibility to identify the atomic states with the principal contribution to the formation of the NDWP.

Outline

Chapter 2

We introduce the general aspects of the helium atom including a description of the Hamiltonian, the spectral properties and the complex rotation method used to get access to the resonance states. We present the numerical approach to describe the unperturbed planar and three-dimensional helium atom, as well as our spectral type method for solving the time-dependent Schrödinger equation describing the helium atom under periodic driving. Finally, we present the entanglement measure used later to characterize the correlation properties of doubly excited states and nondispersive wave packets in planar helium.

Chapter 3

The basic properties of the classical frozen planet configuration are introduced, followed by the identification of frozen planet states of planar and three-dimensional helium for singlet and triplet symmetry with total angular momentum $L = 0$ and $L = 1$, in the energy regime up to the 7th ionization threshold.

Chapter 4

We present a general description of the driven frozen planet configuration and characterize nondispersive wave packets in planar helium, identifying the principal ingredients involved in their formation.

Finally, we give for first time theoretical evidence of the existence of nondispersive wave packets in three-dimensional helium, as well as a brief discussion about their experimental identification.

Chapter 5

We calculate entanglement measures for $^1\mathrm{S}$ and $^1\mathrm{P}$ bound and doubly excited states below the second, third and fourth ionization thresholds for planar helium. We also compute the entanglement of nondispersive wave packets produced by the near-resonant coupling between two frozen planet states.

We conclude the thesis with a summary and discussion of future perspectives. In addition, two appendices are included: **Appendix A** provides the description of the Lanczos algorithm, and some quantities like the the projection of the electronic density in configuration and phase space, and the expectation value of $\cos\theta_{12}$; in **Appendix B** we calculate unnatural parity states of Li^+ below the third and fourth ionization thresholds and oscillator strength for S $\rightarrow$ P and P $\rightarrow$ D transitions.

2 Theoretical and numerical framework

In this chapter, we present the theoretical and numerical framework used to describe the dynamics of the helium atom under periodic driving. In Section 2.1 we discuss the general aspects of the helium atom including a description of the Hamiltonian, the spectral properties and the complex rotation method used to get access to the resonance states. Sections 2.2 and 2.3 are dedicated to our approach to describe the unperturbed planar and three-dimensional helium atom, respectively. In each case, the matrix representation of the problem and its numerical implementation is presented. In Section 2.4, we introduce our spectral type method for solving the time-dependent Schrödinger equation describing the helium atom under periodic driving. Finally, Section 2.5 is devoted to present the entanglement measure which is later used to characterize the correlation properties of doubly excited states and nondispersive wave packets in planar helium.

2.1 Generalities

2.1.1 Hamiltonian

In the center of mass system, the dynamics of a two-electron atom is governed by the following Hamiltonian, given in atomic units[1] (a.u.) and neglecting relativistic effects

$$H_0 = \frac{\vec{p}_1^{\,2}}{2\mu} + \frac{\vec{p}_2^{\,2}}{2\mu} + \frac{\vec{p}_1 \cdot \vec{p}_2}{M} - \frac{Z}{r_1} - \frac{Z}{r_2} + \frac{\gamma}{r_{12}}\,, \tag{2.1}$$

where $\mu = \frac{m_e M}{m_e + M}$ is the reduced mass of the electrons, the parameter γ characterizes the electron-electron interaction, and M and Z represent the mass and charge of the nucleus, respectively (for helium $Z = 2$ and $\gamma = 1$). The positions of the electrons with respect to the nucleus are denoted by $\vec{r}_1$ and $\vec{r}_2$ (see Figure 2.1), and $\vec{p}_1$ and $\vec{p}_2$ their conjugate momenta. As the nucleus is much heavier than an electron, we can work in the infinite nucleus mass approximation, and the Hamiltonian (2.1) becomes

$$H_0 = \frac{\vec{p}_1^{\,2}}{2} + \frac{\vec{p}_2^{\,2}}{2} - \frac{Z}{r_1} - \frac{Z}{r_2} + \frac{\gamma}{r_{12}}\,. \tag{2.2}$$

[1] $\hbar \equiv e \equiv m_e \equiv 1$.

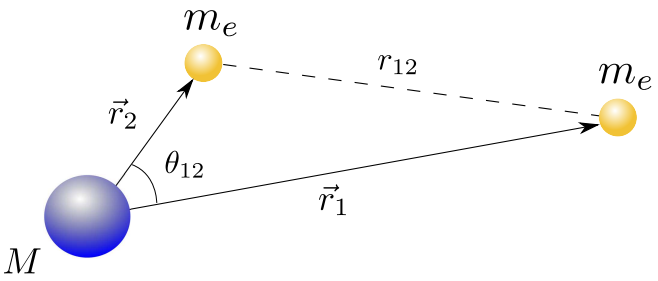


Figure 2.1.: The two-electron atom consists of a nucleus with mass with mass M and charge Z, and two electrons of mass m_e interacting through Coulomb forces. r_{12} is the interelectronic distance and θ_{12} the angle between the two electrons.

This Hamiltonian is spin-independent. Thus, the two-electron wave function $\Phi(q_1, q_2)$ can be written as $\Phi = \Psi(\vec{r}_1, \vec{r}_2)\chi(1,2)$, where $\Psi(\vec{r}_1, \vec{r}_2)$ and $\chi(1,2)$ correspond to the spatial and spin wave functions, respectively. The Pauli exclusion principle states that the wave function $\Phi(q_1, q_2)$ must be antisymmetric under the electron-electron exchange. Hence, the total wave function could be the product of a symmetric spatial wave function by an antisymmetric spin wave function, in that case, the wave function Φ is labeled as singlet state, or could be the product of an antisymmetric spatial wave function by a symmetric spin wave function which corresponds to a triplet state [72].

2.1.2 Spectral properties of helium

In the absence of the electron-electron interaction ($\gamma = 0$), the Hamiltonian (2.2) is just the sum of two hydrogen-like systems and can be solved analytically. In that case, the energy spectrum consists of continuum states above the single ionization thresholds (SIT) and bound states with energies

$$E^{L,M}_{N,n,l_1,l_2} = -\frac{2}{(N-\delta)^2} - \frac{2}{(n-\delta)^2}, \qquad N \leq n\,, \tag{2.3}$$

where L denotes the total orbital angular momentum, M its projection, and (N, l_1) and (n, l_2) are the principal quantum number and angular momentum of the inner and outer electron, respectively, with $\delta = 0.5$ for planar helium [73] and $\delta = 0$ for three-dimensional helium. As shown in Figure 2.2, the energies in Eq. (2.3) correspond to Rydberg series of bound states converging to the Nth single ionization threshold $I_N = -2/(N-\delta)^2$ and the series of the single ionization thresholds converges to the double ionization threshold (DIT).

A given state described by Hamiltonian (2.2) requires eight quantum numbers for its classification[2]. However, the rotational invariance and the fact that the total spin $\vec{S}$

[2]The wave function $\Phi = \Psi(\vec{r}_1, \vec{r}_2)\chi(1,2)$ describes six spatial and two spin degrees of freedom.

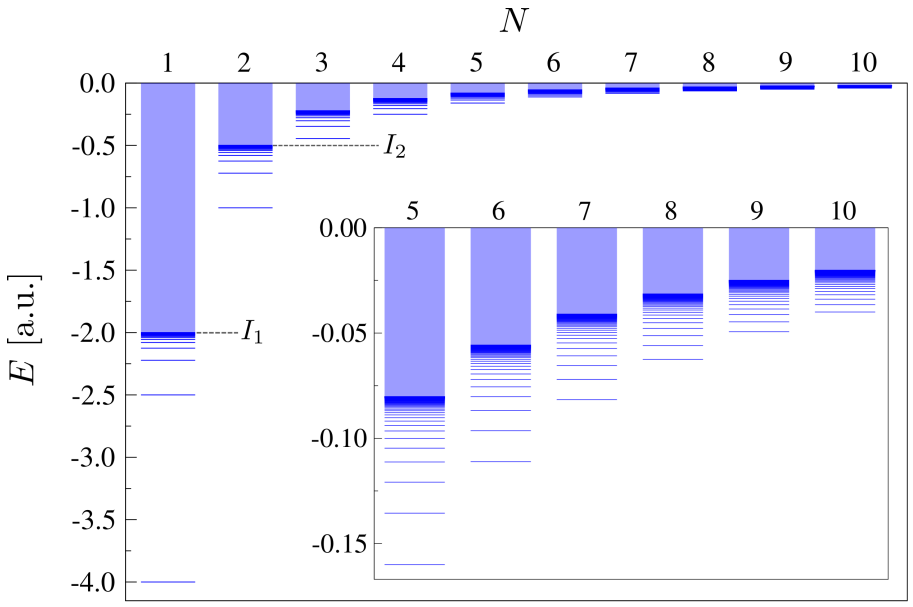


Figure 2.2.: Spectrum of helium without electron-electron interaction ($\gamma = 0$). The energy levels are organized in Rydberg series labeled by the principal quantum number N of the inner electron. The inset zooms the energy regime between the fifth and the tenth ionization threshold.

commutes with H_0 reduce to four the number of degrees of freedom, i.e., the total orbital angular momentum $\vec{L}$, the spin $\vec{S}$ and their respective projections are conserved quantities. The leftover nonseparable degrees of freedom are commonly given by approximate quantum numbers [74, 74–78]. In the commonly used spectral notation ${}^{2S+1}\mathrm{L}^{\pi}$, ($S = 0$) and ($S = 1$) describe singlet and triplet states, respectively, while $\pi = +1$ and $\pi = -1$ describe even (e) and odd (o) states, being $\pi = \pm 1$ the eigenvalues of the parity operator $\Pi : (\vec{r}_1, \vec{r}_2) \rightarrow (-\vec{r}_1, -\vec{r}_2)$.

The first experimental observation of doubly excited states of helium [30] revealed the fact that these strongly correlated states cannot be in general described by independent particle quantum numbers, since the electrons can occupy a number of quasidegenerate configurations. This can be seen in Figure 2.3, where part of the energy spectrum for ${}^{1}\mathrm{S}^{\mathrm{e}}$ states of helium including the electron-electron interaction ($\gamma = 1$) is depicted. Compared to the independent particle picture, the energy positions of the single ionization thresholds remain unaffected. However, the eigenenergies are significantly modified due to the interelectronic-interaction. Furthermore, doubly excited states couple to the continuum states of the lower lying series and transform into autoionizing resonance states with a finite lifetime.

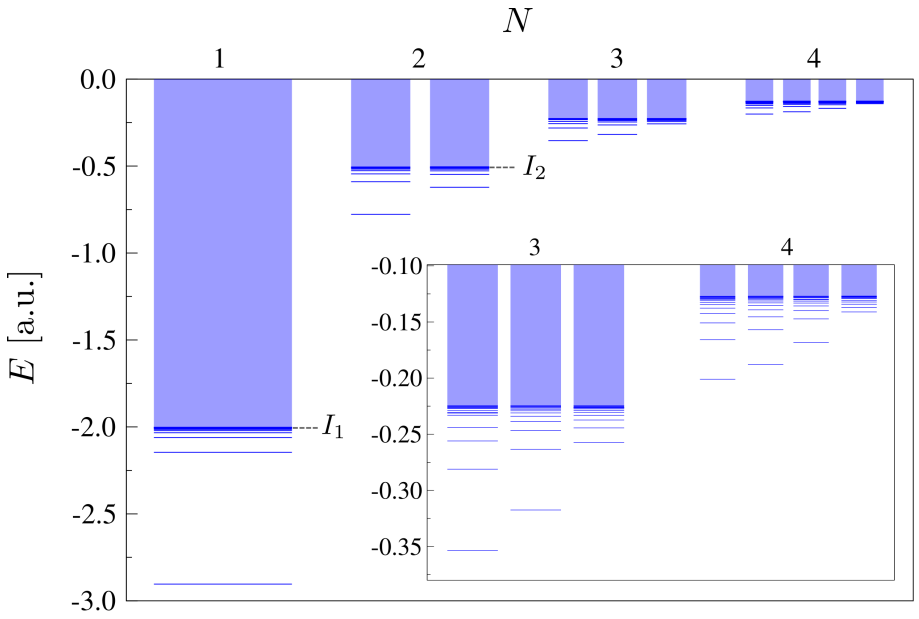


Figure 2.3.: Spectrum of helium for ${}^1\mathrm{S}^e$ states (data from [79]). The energy levels are organized in series labeled by the principal quantum number N of the inner electron. The subseries are organized according Herrick's classification [75, 76, 80]. The inset zooms the $N = 3$ and $N = 4$ series.

2.1.3 Complex rotation method

In the previous section, we have seen that doubly excited states in the spectrum of helium correspond to resonances embedded in the continua. To extract the energies and decay rates of these resonance states, we use the method of complex coordinate rotation (or complex scaling) [81].

The complex rotation by an angle θ is given by the non-unitary operator

$$R(\theta) = \exp\left(-\theta \frac{\vec{r}\cdot\vec{p} + \vec{p}\cdot\vec{r}}{2}\right). \tag{2.4}$$

The transformation of the coordinates and momenta is given by

$$\begin{aligned} \vec{r} &\rightarrow \vec{r}e^{\mathrm{i}\theta}, \\ \vec{p} &\rightarrow \vec{p}e^{-\mathrm{i}\theta}. \end{aligned} \tag{2.5}$$

The rotated Hamiltonian $H(\theta) = R(\theta)HR(-\theta)$ is no longer Hermitian, and its spectrum has the following properties [81–83] (see Figure 2.4):

- The bound states of H remain unchanged under the transformation.

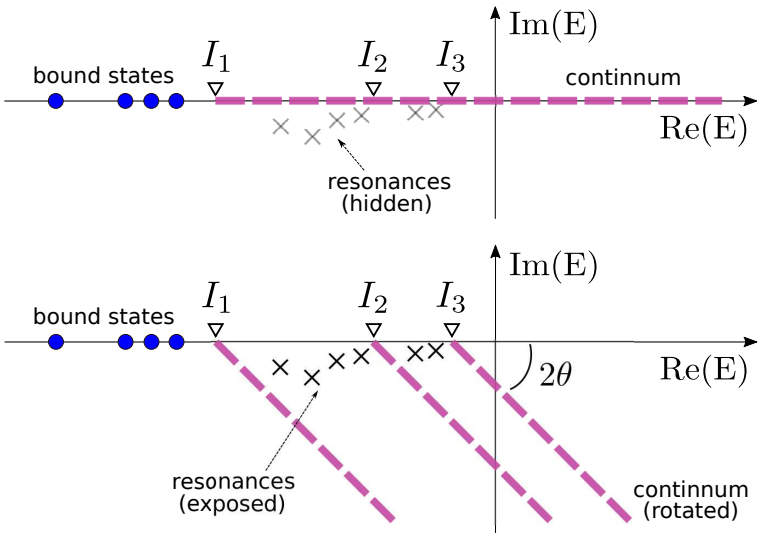


Figure 2.4.: Energy spectrum of the unrotated Hamiltonian H (top) and the complex rotated Hamiltonian $H(\theta)$ (bottom). Complex rotation uncovers the hidden resonances by rotating the continua around the ionization thresholds in the lower half plane, by an angle 2θ.

- The continuum states are rotated downwards by an angle 2θ with the real axis, around its individual threshold.
- Once the rotation angle θ is sufficiently large, the resonance states are “exposed" and are associated to complex eigenvalues $E_{i,\theta} = E_i - \mathrm{i}\Gamma_i/2$, where the real part corresponds to the energy E_i of the resonance, and the imaginary part contains the decay rate Γ_i, which is the inverse of the resonance lifetime.

The eigenvectors $|\Psi_{i,\theta}\rangle$ of the rotated Hamiltonian $H(\theta)$ are normalized for the scalar product

$$\langle\overline{\Psi_{i,\theta}}|\Psi_{j,\theta}\rangle = \delta_{ij}\,, \tag{2.6}$$

and satisfy the closure relation

$$\sum_i |\Psi_{i,\theta}\rangle\langle\overline{\Psi_{i,\theta}}| = 1\,, \tag{2.7}$$

where $\langle\overline{\Psi_{i,\theta}}|$ is the transpose of $\langle\Psi_{i,\theta}|$. Additionally, the projection operator on a real energy eigenstate $|\phi_E\rangle$, in terms of the eigenvectors of the rotated Hamiltonian, reads [84–86]

$$|\phi_E\rangle\langle\phi_E| = \frac{1}{2\pi\mathrm{i}}\sum_i \left\{ \frac{R(-\theta)|\Psi_{i,\theta}\rangle\langle\overline{\Psi_{i,\theta}}|R(\theta)}{E_{i,\theta} - E} - \frac{R(\theta)|\overline{\Psi_{i,\theta}}\rangle\langle\Psi_{i,\theta}|R(-\theta)}{\overline{E_{i,\theta}} - E} \right\}. \tag{2.8}$$

This projector will be useful in the computation of some important quantities in Appendix A.

2.2 Planar treatment of the two-electron atom

In this simplified model, the dynamics of the atom is confined to a plane. A comprehensive description of the representation we use for this model can be found in [38,39,73].

2.2.1 Regularization of the 2D helium Hamiltonian

The regularization of the Coulomb singularities in the Hamiltonian (2.2) is achieved by transforming the Cartesian coordinates of the electrons (x_1, y_1) and (x_2, y_2) to a set of parabolic coordinates, obtained after three coordinate transformations: a parabolic transformation

$$\mu_i = \sqrt{r_i + x_i}\,, \qquad \nu_i = \sqrt{r_i - x_i}\,, \tag{2.9}$$

followed by a rotation by $\pi/4$

$$\mu_\pm = \frac{\mu_1 \pm \mu_2}{\sqrt{2}}\,, \qquad \nu_\pm = \frac{\nu_1 \pm \nu_2}{\sqrt{2}}\,, \tag{2.10}$$

and a second parabolic transformation

$$x_\pm = \sqrt{r_\pm + \mu_\pm}\,, \qquad y_\pm = \sqrt{r_\pm - \mu_\pm}\,, \tag{2.11}$$

where $r_i = \sqrt{x_i^2 + y_i^2}$ $(i = 1, 2)$ and $r_\pm = \sqrt{\mu_\pm^2 + \nu_\pm^2}$. After these transformations, the expressions for the distances r_1, r_2 and r_{12} become polynomial functions in the new coordinates

$$\begin{aligned} r_1 &= \frac{1}{16}\left((x_+ - y_-)^2 + (x_- + y_+)^2\right)\left((x_+ + y_-)^2 + (x_- - y_+)^2\right), \\ r_2 &= \frac{1}{16}\left((x_+ - x_-)^2 + (y_+ + y_-)^2\right)\left((x_+ + x_-)^2 + (y_+ - y_-)^2\right), \\ r_{12} &= \frac{1}{4}\left(x_+^2 - y_+^2\right)\left(x_-^2 + y_-^2\right). \end{aligned} \tag{2.12}$$

The time-independent Schrödinger equation $H_0|\psi\rangle = E|\psi\rangle$ is regularized by multiplication with the *Jacobian* of the transformation

$$J = 16 r_1 r_2 r_{12}\,. \tag{2.13}$$

In this way, we obtain the generalized eigenvalue problem (GEVP)

$$\left(-\frac{1}{2}T + V\right)|\psi\rangle = EJ|\psi\rangle\,, \tag{2.14}$$

where

$$T = 16r_1r_2r_{12}(\nabla_1^2 + \nabla_2^2)\,, \tag{2.15}$$

$$V = -32r_2r_{12} - 32r_1r_{12} + 16r_1r_2\,. \tag{2.16}$$

It can be shown that the operators involved in this GEVP are polynomial functions of the parabolic coordinates and their partial derivatives [38]. This fact allows us to introduce a set of creation and annihilation operators defined by

$$\begin{aligned} a_{x_\pm} &= \frac{x_\pm + \mathrm{i}p_{x_\pm}}{\sqrt{2}}, \qquad a^\dagger_{x_\pm} = \frac{x_\pm - \mathrm{i}p_{x_\pm}}{\sqrt{2}}\,, \\ a_{y_\pm} &= \frac{y_\pm + \mathrm{i}p_{y_\pm}}{\sqrt{2}}, \qquad a^\dagger_{y_\pm} = \frac{y_\pm - \mathrm{i}p_{y_\pm}}{\sqrt{2}}\,. \end{aligned}$$

Then, we define the circular operators in the planes (x_+, y_+) and (x_-, y_-) as

$$\begin{aligned} a_1 &= \frac{a_{x_+} - \mathrm{i}a_{y_+}}{\sqrt{2}}, \qquad a_2 = \frac{a_{x_+} + \mathrm{i}a_{y_+}}{\sqrt{2}}\,, \\ a_3 &= \frac{a_{x_-} - \mathrm{i}a_{y_-}}{\sqrt{2}}, \qquad a_4 = \frac{a_{x_-} + \mathrm{i}a_{y_-}}{\sqrt{2}}\,, \end{aligned} \tag{2.17}$$

which satisfy the usual commutation relations

$$[a_i, a_j] = 0, \qquad [a_i^\dagger, a_j^\dagger] = 0, \qquad [a_i, a_j^\dagger] = \delta_{i,j}, \qquad i,j = 1,2,3,4.$$

In this way, we obtain a basis set of tensorial products of harmonic oscillator Fock states

$$|n_1n_2n_3n_4\rangle = |n_1\rangle \otimes |n_2\rangle \otimes |n_3\rangle \otimes |n_4\rangle\,, \tag{2.18}$$

where $n_i = a_i^\dagger a_i$. The appropriate symmetrization of this basis will be discussed in Section 2.2.3.

The major advantage of this representation is that the expressions for J, T and V are polynomial functions of finite degree of the circular operators a_i and $a_i^\dagger$. In this way, the matrix elements of the GEVP (2.14) can be calculated analytically [38], and are expressed in normally ordered (creation operators on the left [87]) monomial terms of the form $M = a_1^{\dagger\alpha_1}a_2^{\dagger\alpha_2}a_3^{\dagger\alpha_3}a_4^{\dagger\alpha_4}a_1^{\beta_1}a_2^{\beta_2}a_3^{\beta_3}a_4^{\beta_4}$, where α_i and β_i are integer numbers. Since the number of monomials in the GEVP is finite, the number coupled basis states is also finite. This determines a set of selection rules $\{\Delta n_1, \Delta n_2, \Delta n_3, \Delta n_4\}$, with $\Delta n_i = n_i - n_i'$,

if $\langle n_1 n_2 n_3 n_4 | M | n_1' n_2' n_3' n_4' \rangle \neq 0$. For the GEVP (2.14) all the selection rules satisfy $-4 \leq \Delta n_i \leq 4$ and $\Delta n_1 - \Delta n_2 + \Delta n_3 - \Delta n_4 = 0$.

2.2.2 Matrix representation

In addition to the complex rotation (see Section 2.1.3), we use a dilation by a positive real number α, given by the unitary operator [88]

$$D_\alpha = \exp\left(\mathrm{i}\log(\alpha)\frac{\vec{r}\cdot\vec{p}+\vec{p}\cdot\vec{r}}{2}\right). \tag{2.19}$$

Under complex rotation (2.4) and dilation (2.19), the Cartesian coordinates and momenta transform as

$$\begin{aligned} \vec{r} &\rightarrow \alpha\vec{r}e^{\mathrm{i}\theta}, \\ \vec{p} &\rightarrow \frac{1}{\alpha}\vec{p}e^{-\mathrm{i}\theta}. \end{aligned} \tag{2.20}$$

After complex rotation and dilation, the matrix representation of the generalized eigenvalue problem (2.14) reads

$$\mathbf{H}_0^\alpha(\theta)\mathbf{\Psi}_\theta = E_\theta \mathbf{J}\mathbf{\Psi}_\theta, \tag{2.21}$$

where

$$\mathbf{H}_0^\alpha(\theta) = -\frac{1}{2\alpha^2}\mathbf{T}e^{-2\mathrm{i}\theta} + \frac{1}{\alpha}\mathbf{V}e^{-\mathrm{i}\theta}, \tag{2.22}$$

with $\mathbf{T}$, $\mathbf{V}$ and $\mathbf{J}$ the matrix representations of (2.15), (2.16) and (2.13), respectively, and $\mathbf{\Psi}_\theta$ is the vector representation of the wave function.

2.2.3 Construction of the basis

The planar helium atom is invariant under rotations around an axis perpendicular to the plane, under the exchange symmetry P_{12} and under the parity Π. The system is also invariant under the reflections Π_x and Π_y with respect to the x and y axes, respectively, which are related to the total parity by $\Pi = \Pi_x\Pi_y = \Pi_y\Pi_x$. These symmetries commute with L_z^2 and anticommute with L_z. In this work the eigenstates of the planar helium atom are labeled by the absolute value $|l|$ of the angular momentum L_z, the exchange symmetry P_{12}, and the symmetry $\Pi_x = \pm 1$.

The symmetrization of the basis (2.18) with respect to P_{12} and L_z is given by [38, 73]

$$|n_1 n_2 n_3 n_4\rangle^+ = |n_1 n_2 n_3 n_4\rangle + |n_3 n_4 n_1 n_2\rangle. \tag{2.23}$$

Additionally, the basis can be adapted to the symmetry Π_x by the definition [38, 39]

$$|n_1 n_2 n_3 n_4\rangle^{+\epsilon_x} = |n_1 n_2 n_3 n_4\rangle^{+} + \epsilon_x |n_2 n_1 n_4 n_3\rangle^{+}, \tag{2.24}$$

where $\epsilon_x = \pm 1$. With this, the basis decomposes into the subspaces of even ($\epsilon_x = 1$) or odd ($\epsilon_x = -1$) states with respect to the symmetry Π_x, and of singlet and triplet states according to

$$\begin{aligned} &\text{Singlet states :} && n_1 - n_2 \equiv n_3 - n_4 \equiv 0 \pmod 4 \\ &\text{Triplet states :} && n_1 - n_2 \equiv n_3 - n_4 \equiv 2 \pmod 4 \end{aligned} \tag{2.25}$$

Due to the twofold symmetrization in (2.23) and (2.24), the unambiguous definition of the basis is achieved only if each quadruplet (n_1, n_2, n_3, n_4) satisfies one of the following conditions:

$$\begin{cases} |l| > 0 \quad \text{and} \quad \mathrm{n}_1 \geq \mathrm{n}_3, \\ |l| = 0 \quad \text{and} \quad \mathrm{n}_1 > \mathrm{n}_3 \quad \text{and} \quad \mathrm{n}_1 \geq \mathrm{n}_4 > \mathrm{n}_2, \\ \qquad\quad\;\; n_1 > n_3 \quad \text{and} \quad \mathrm{n}_1 > \mathrm{n}_2 > \mathrm{n}_4, \\ \qquad\quad\;\; n_1 > n_3 \quad \text{and} \quad \mathrm{n}_1 = \mathrm{n}_2, \\ \qquad\quad\;\; n_1 = n_3 \quad \text{and} \quad \mathrm{n}_2 > \mathrm{n}_4, \\ \qquad\quad\;\; n_1 = n_2 = n_3 = n_4, \end{cases} \tag{2.26}$$

where the case $n_1 = n_2 = n_3 = n_4$ is forbidden for the odd subspace ($\epsilon_x = -1$).

The numerical implementation requires the truncation of the infinite symmetrized basis, which is made according to

$$n_1 + n_2 + n_3 + n_4 \leq n_{\text{base}}\,, \tag{2.27}$$

with n_{base} a positive integer. This value determines the dimensions of the matrices $\mathbf{H}_0^{\alpha}(\theta)$ and $\mathbf{J}$ in (2.21), which due to the selection rules in (n_1, n_2, n_3, n_4), correspond to sparse banded matrices of bandwidth n_{larg} and size n_{tot}. For example, Table 2.1 shows the dimensions of the matrices for angular momentum $L = 0, 1, 2$ and singlet symmetry as a function of n_{base}.

2.2.4 Convergence of the method

As mentioned in the previous section, our numerical method requires the truncation of the basis. As a consequence, the spectrum of the truncated Hamiltonian is not anymore exact. The otherwise invariant spectrum of the dilated Hamiltonian $H^{\alpha} = D_{\alpha} H D_{\alpha}^{\dagger}$ exhibits a dependence on the dilation parameter α which can be used as a variational

	$L=0$		$L=1$		$L=2$	
n_{base}	n_{tot}	n_{larg}	n_{tot}	n_{larg}	n_{tot}	n_{larg}
150	9 500	1 248	18 620	2 427	18 492	2 418
200	22 100	2 181	43 525	4 261	43 353	4 262
250	42 656	3 363	84 289	6 618	84 073	6 616
300	73 150	4 810	144 819	9 502	144 559	9 497

Table 2.1.: Dimensions of the matrices for different values of n_{base} and angular momentum. For $L > 0$ the dimensions of the matrices are nearly twice that for $L = 0$.

parameter that has to be optimized [38]. There is also a dependence of the bound and resonance spectrum on the angle θ in the truncated rotated Hamiltonian. Therefore, all the numerical values obtained by diagonalization of the eigenvalue problem (2.21) need to be tested for convergence with respect to variation of the truncation parameter n_{base}, complex rotation angle θ and dilation parameter α.

As an example of the analysis of converged digits, in Table 2.2 we present the energy of the lowest four singly excited states of planar helium for singlet symmetry and $L = 0$, computed for complex rotation angle $\theta = 0$ and different values for n_{base} and the dilation parameter α. For the case of the first singly excited state we obtain a converged value for $n_{\mathrm{base}} = 150$, while for the second, third and four excited states the convergence is obtained for $n_{\mathrm{base}} = 200$, $n_{\mathrm{base}} = 250$ and $n_{\mathrm{base}} = 300$, respectively.

Table 2.3 shows the energy and decay rate of the first two $^1\mathrm{S}$ resonances of planar helium, calculated for $n_{\mathrm{base}} = 250$ and different values of the complex rotation angle θ and dilation parameter α. As in the previous case, we observe better convergence for the first state. To improve the convergence of highly excited states we need to consider greater values for n_{base}. However, for doubly excited states below the $N = 7$ ionization threshold we can obtain at least ten converged digits (which is enough for our calculations) with $n_{\mathrm{base}} = 300$.

(N,n)		$(1,2)$	$(1,3)$	$(1,4)$	$(1,5)$
n_{base}	α	$-E$ [a.u.]	$-E$ [a.u.]	$-E$ [a.u.]	$-E$ [a.u.]
150	0.3	8.250 463 875 378 51	8.085 842 790 643 53	8.042 862 620 015 93	8.022 578 201 073 78
	0.4	8.250 463 875 378 53	8.085 842 792 776 75	8.042 910 996 887 38	8.025 658 328 265 39
	0.5	8.250 463 875 378 53	8.085 842 792 685 37	8.042 910 854 148 08	8.025 644 598 299 92
200	0.3	8.250 463 875 378 53	8.085 842 792 777 34	8.042 911 010 601 17	8.025 663 009 973 67
	0.4	8.250 463 875 378 56	8.085 842 792 777 34	8.042 911 011 138 42	8.025 668 308 822 26
	0.5	8.250 463 875 378 53	8.085 842 792 777 34	8.042 911 011 059 16	8.025 668 270 988 73
250	0.3	8.250 463 875 378 53	8.085 842 792 777 34	8.042 911 011 138 66	8.025 668 309 608 42
	0.4	8.250 463 875 378 53	8.085 842 792 777 34	8.042 911 011 138 70	8.025 668 309 756 49
	0.5	8.250 463 875 378 51	8.085 842 792 777 35	8.042 911 011 138 62	8.025 668 309 682 81
300	0.3	8.250 463 875 378 50	8.085 842 792 777 34	8.042 911 011 138 67	8.025 668 309 756 60
	0.4	8.250 463 875 378 53	8.085 842 792 777 34	8.042 911 011 138 69	8.025 668 309 756 66
	0.5	8.250 463 875 378 52	8.085 842 792 777 35	8.042 911 011 138 69	8.025 668 309 756 48
Conv. value:		8.250 463 875 378 5	8.085 842 792 777 3	8.042 911 011 138 6	8.025 668 309 756

Table 2.2.: Energy values of the lowest four singly excited ^{1}S states of planar helium computed for complex rotation angle $\theta = 0$ and different values for n_{base} and dilation parameter α. Results without analysis of converged digits and converged values are shown.

		First resonance		Second resonance	
θ	α	$-E$ [a.u.]	$\Gamma/2$ [a.u.]	$-E$ [a.u.]	$\Gamma/2$ [a.u.]
0.20	0.3	1.411 496 328 143 06	0.001 241 734 388 91	1.027 047 552 808 61	0.000 251 801 476 01
	0.4	1.411 496 328 143 87	0.001 241 734 388 40	1.027 047 552 808 95	0.000 251 801 467 68
0.25	0.3	1.411 496 328 143 98	0.001 241 734 388 97	1.027 047 552 808 68	0.000 251 801 475 93
	0.4	1.411 496 328 143 99	0.001 241 734 388 65	1.027 047 552 814 16	0.000 251 801 458 17
0.30	0.3	1.411 496 328 143 98	0.001 241 734 388 97	1.027 047 552 808 67	0.000 251 801 475 92
	0.4	1.411 496 328 143 98	0.001 241 734 388 98	1.027 047 552 807 16	0.000 251 801 479 93
0.35	0.3	1.411 496 328 143 98	0.001 241 734 388 97	1.027 047 552 808 69	0.000 251 801 475 91
	0.4	1.411 496 328 143 99	0.001 241 734 388 97	1.027 047 552 805 93	0.000 251 801 473 81
0.40	0.3	1.411 496 328 143 98	0.001 241 734 388 97	1.027 047 552 808 69	0.000 251 801 475 93
	0.4	1.411 496 328 143 99	0.001 241 734 388 99	1.027 047 552 816 16	0.000 251 801 469 35
Conv. value:		1.411 496 328 143	0.001 241 734 388	1.027 047 552 8	0.000 251 801 4

Table 2.3.: Energies and decay rates of the first two ^{1}S resonances of planar helium computed for $n_{\mathrm{base}} = 250$ and different values for θ and α. Results without analysis of converged digits and converged values are shown.

2.3 Three-dimensional two-electron atom model

2.3.1 Expansion for the wave function

The description of the system is given by the time-independent Schrödinger equation

$$H_0\Psi(\vec{r}_1,\vec{r}_2) = E\Psi(\vec{r}_1,\vec{r}_2)\,, \tag{2.28}$$

where H_0 is the unperturbed Hamiltonian (2.2). The wave function $\Psi(\vec{r}_1,\vec{r}_2)$ is expanded in a configuration interaction basis [25, 54], for a given value of the total orbital angular momentum L and its projection M along the z-axis

$$\Psi^{L,M}(\vec{r}_1,\vec{r}_2) = \sum_{\epsilon_{12},\pi}\sum_{l_1,l_2}^{\pi}\sum_{s}\sum_{n_1,n_2}\psi^{l_1,l_2,L,M,\epsilon_{12}}_{\kappa_{1s},\kappa_{2s},n_1,n_2}\,\beta^{l_1,l_2}_{n_1,n_2}\,\mathcal{A}\,F^{l_1,l_2,L,M}_{\kappa_{1s},\kappa_{2s},n_1,n_2}(\vec{r}_1,\vec{r}_2)\,, \tag{2.29}$$

with

$$F^{l_1,l_2,L,M}_{\kappa_{1s},\kappa_{2s},n_1,n_2}(\vec{r}_1,\vec{r}_2) = \frac{S^{(\kappa_{1s})}_{n_1,l_1}(r_1)}{r_1}\frac{S^{(\kappa_{2s})}_{n_2,l_2}(r_2)}{r_2}\Lambda^{L,M}_{l_1,l_2}(\hat{r}_1,\hat{r}_2)\,, \tag{2.30}$$

where $\hat{r}\equiv(\theta,\phi)$ denotes the angular coordinates.

The quantity

$$\beta^{l_1,l_2}_{n_1,n_2} = 1+\left(\frac{1}{\sqrt{2}}-1\right)\delta_{n_1,n_2}\,\delta_{l_1,l_2}\,, \tag{2.31}$$

controls the redundancy in the basis, which may occur due to particle exchange, and the operator

$$\mathcal{A} = \frac{1+(-1)^{l_1+l_2-L}\epsilon_{12}P}{\sqrt{2}}\,, \tag{2.32}$$

projects onto singlet ($\epsilon_{12}=+1$) or triplet ($\epsilon_{12}=-1$) states, where P simultaneously exchanges (κ_{1s},n_1,l_1) with (κ_{2s},n_2,l_2). The symbol $\sum^{\pi}$ in Eq. (2.29) indicates that this sum depends on the parity π, where the distinction is made between natural parity states $\left(\pi=(-1)^L\right)$ and unnatural parity states $\left(\pi=(-1)^{L+1}\right)$ (see Appendix B.1).

The radial part of the wave function is described by one-electron Coulomb-Sturmian functions $S^{(\kappa)}_{n,l}(r)$ defined by [58, 59]

$$S^{(\kappa)}_{n,l}(r) = N^{\kappa}_{n,l}\,r^{l+1}e^{-\kappa r}L^{(2l+1)}_{n-l-1}(2\kappa r)\,, \tag{2.33}$$

which satisfy the orthogonality relation

$$\left\langle S^{(\kappa)}_{n,l}(r)\left|\frac{1}{r}\right|S^{(\kappa)}_{n',l}(r)\right\rangle \equiv \int_0^{\infty}dr\,S^{(\kappa)}_{n,l}(r)\frac{1}{r}S^{(\kappa)}_{n',l}(r) = \frac{\kappa}{n}\delta_{n',n}\,, \tag{2.34}$$

where l corresponds to the angular momentum, n is a radial index, κ is a dilation parameter, $L_m^{(\alpha)}(x)$ is an associated Laguerre polinomial and $N_{n,l}^{\kappa}$ the normalization constant

$$N_{n.l}^{\kappa} = \sqrt{\frac{\kappa(n-l-1)!}{n(n+l)!}}\,. \tag{2.35}$$

The angular part of the wave function is expanded in terms of bipolar spherical harmonics [57]

$$\Lambda_{l_1,l_2}^{L,M}(\hat{r}_1,\hat{r}_2) = \sum_{m_1,m_2} (-1)^{l_1-l_2+M}\sqrt{2L+1}\begin{pmatrix} l_1 & l_2 & L \\ m_1 & m_2 & -M \end{pmatrix} Y_{l_1,m_1}(\hat{r}_1)Y_{l_2,m_2}(\hat{r}_2)\,, \tag{2.36}$$

with orthonormalization relation

$$\int d\hat{r}_1 d\hat{r}_2\, \Lambda_{l_1,l_2}^{L,M\,*}(\hat{r}_1,\hat{r}_2)\Lambda_{l_1',l_2'}^{L',M'}(\hat{r}_1,\hat{r}_2) = \delta_{l_1,l_1'}\,\delta_{l_2,l_2'}\,\delta_{L,L'}\,\delta_{M,M'}\,, \tag{2.37}$$

where Y_{l_1,m_1} are the spherical harmonics and the 2×3 array in parentheses is the Wigner $3jm$-symbol [57].

To obtain an expression for the interelectronic distance r_{12} which is not an explicit coordinate in the CI approach, the method uses the multipole expansion of the electron-electron Coulomb repulsion

$$\frac{1}{r_{12}} = \sum_{q=0}^{\infty}\sum_{p=-q}^{q}\frac{4\pi}{2q+1}\frac{r_<^q}{r_>^{q+1}}Y_{q,p}^*(\hat{r}_1)Y_{q,p}(\hat{r}_2)\,, \tag{2.38}$$

where $r_< = \min(\mathrm{r}_1,\mathrm{r}_2)$ and $r_> = \max(\mathrm{r}_1,\mathrm{r}_2)$.

The Coulomb-Sturmian function $S_{n,l}^{\kappa}(r)$ coincides with the hydrogen radial eigenfunction when $\kappa = Z/n$. Therefore, the dilation parameter κ can be properly tuned to improve convergence of a given region of the spectrum. For a large (resp. small) parameter κ the corresponding Coulomb-Sturmian function $S_{n,l}^{\kappa}(r)$ have a short (resp. large) extend in space. Thus, for describing symmetrically excited states the expansion (2.29) uses equal parameters κ for all Coulomb-Sturmian functions (which is the general case for CI expansions involving this kind of radial functions). However, for asymmetrically excited states, e.g., the frozen planet states of Section 3.2, the description of the inner electron which is close to the nucleus requires Sturmian functions with large dilation parameter, while for the outer electron relatively far from the nucleus is described by Sturmian functions with small dilation parameter. In this way, the description of each electron with a different set of dilation parameters and Coulomb-Sturmian functions allows us to include in the expansion (2.29) only the essential basis functions, which reduces the basis size compare to standard CI approaches. For a given pair of angular momenta

(l_1, l_2), we can choose one or many sets of Coulomb-Sturmian functions characterized by the combination $\{\kappa_{1s}, N_{1s}^{\min}, N_{1s}^{\max}, \kappa_{2s}, N_{2s}^{\min}, N_{2s}^{\max}\}$ with $l_1 + N_{1s}^{\min} \leq n_1 \leq l_1 + N_{1s}^{\max}$ and $l_2 + N_{2s}^{\min} \leq n_2 \leq l_2 + N_{2s}^{\max}$. In addition, all terms leading to redundancies in the expansion (2.29) due to the products between Coulomb-Sturmian functions are excluded.

2.3.2 Matrix representation

After substitution of the wave function expansion (2.29) into (2.28), the time-independent Schrödinger equation in its matrix form is obtained by a multiplication from the left by $\beta_{n_1',n_2'}^{l_1',l_2'} \mathcal{A}' F_{\kappa_{1s}',\kappa_{2s}',n_1',n_2'}^{l_1',l_2',L',M'}(\vec{r}_1, \vec{r}_2)$ and an integration over the whole space on both spatial and angular coordinates, where the symmetrization operator $\mathcal{A}'$ acts on primed quantities. This leads to

$$\sum_{\epsilon_{12},\pi} \sum_{l_1,l_2}^{\pi} \sum_{s} \sum_{n_1,n_2} \beta_{n_1,n_2}^{l_1,l_2} \beta_{n_1',n_2'}^{l_1',l_2'} \psi_{\kappa_{1s},\kappa_{2s},n_1,n_2}^{l_1,l_2,L,M,\epsilon_{12}} \Big(H_{0\,\kappa_{1s},\kappa_{2s},n_1,n_2,\kappa_{1s}',\kappa_{2s}',n_1',n_2'}^{l_1,l_2,L,M,l_1',l_2',L',M'} - E S_{\kappa_{1s},\kappa_{2s},n_1,n_2,\kappa_{1s}',\kappa_{2s}',n_1',n_2'}^{l_1,l_2,L,M,l_1',l_2',L',M'} \Big) = 0\,, \tag{2.39}$$

where

$$H_{0\,\kappa_{1s},\kappa_{2s},n_1,n_2,\kappa_{1s}',\kappa_{2s}',n_1',n_2'}^{l_1,l_2,L,M,l_1',l_2',L',M'} = \int d\vec{r}_1\, d\vec{r}_2\, \mathcal{A}' F_{\kappa_{1s}',\kappa_{2s}',n_1',n_2'}^{l_1',l_2',L',M'\,*}(\vec{r}_1, \vec{r}_2) H_0 \mathcal{A} F_{\kappa_{1s},\kappa_{2s},n_1,n_2}^{l_1,l_2,L,M}(\vec{r}_1, \vec{r}_2)\,, \tag{2.40}$$

and

$$S_{\kappa_{1s},\kappa_{2s},n_1,n_2,\kappa_{1s}',\kappa_{2s}',n_1',n_2'}^{l_1,l_2,L,M,l_1',l_2',L',M'} = \int d\vec{r}_1\, d\vec{r}_2\, \mathcal{A}' F_{\kappa_{1s}',\kappa_{2s}',n_1',n_2'}^{l_1',l_2',L',M'\,*}(\vec{r}_1, \vec{r}_2) \mathcal{A} F_{\kappa_{1s},\kappa_{2s},n_1,n_2}^{l_1,l_2,L,M}(\vec{r}_1, \vec{r}_2)\,, \tag{2.41}$$

correspond to the matrix elements of the Hamiltonian matrix $\mathbf{H}_0$ and the matrix $\mathbf{S}$ representing the overlap, respectively.

Under the complex rotation (2.4) the Hamiltonian H_0 in (2.40) becomes

$$H_0(\theta) = T e^{-2\mathrm{i}\theta} + V e^{-\mathrm{i}\theta} + U e^{-\mathrm{i}\theta}\,, \tag{2.42}$$

where the kinetic term T, the nucleus-electrons interaction term V and the electron-electron repulsion term U are respectively given by

$$T = \frac{\vec{p}_1^{\,2}}{2} + \frac{\vec{p}_2^{\,2}}{2}, \qquad V = -\frac{Z}{r_1} - \frac{Z}{r_2}, \qquad U = \frac{1}{r_{12}}. \tag{2.43}$$

Finally, the Schrödinger equation writes as the generalized eigenvalue problem

$$\mathbf{H}_0(\theta) \mathbf{\Psi}_\theta = E_\theta \mathbf{S} \mathbf{\Psi}_\theta\,, \tag{2.44}$$

where $\mathbf{\Psi}_\theta$ is the vector representation of the wave function.

The calculation of the integrals (2.40) and (2.41) can be performed analytically, but its evaluation becomes very difficult due to the introduction of various sets of Coulomb-Sturmian functions with different dilation parameters. Nevertheless, since the elements involved in our calculations are polynomials, an efficient and accurate computation of these integrals is achieved with Gauss-Laguerre quadrature [70, 89]. The only exception is for the case of the electron-electron repulsion term $1/r_{12}$ given by the multipole expansion (2.38), whose matrix representation has to be calculated using recursive relations [90, 91]. A detailed description of the numerical computation of the matrix elements (2.40) and (2.41) is given by Eiglsperger [25, 71].

The Coulomb-Sturmian basis in the expansion (2.29) is complete when only one dilation parameter is considered. However, with the inclusion of many sets of dilation parameters the basis becomes overcomplete. This means that some eigenvalues of the overlap matrix $\mathbf{S}$ can be numerically zero, which causes numerical overflows whenever the inversion of the overlap matrix is required. To deal with this situation let us consider the $(n \times n)$ orthogonal matrix $\mathbf{T}$ which diagonalizes overlap matrix $\mathbf{S}$. Thus, $\mathbf{T}^t\mathbf{S}\mathbf{T} = \mathbf{s}$ where $\mathbf{s}$ is the diagonal matrix containing the eigenvalues of $\mathbf{S}$.

By rejecting the $n-p$ eigenvalues of $\mathbf{S}$ that are smaller than a certain cutoff of the order of 10^{-12}, the sizes of the matrices $\mathbf{T}$ and $\mathbf{s}$ reduce to $(n \times p)$ and $(p \times p)$, respectively. Then, defining the non symmetric $(n \times p)$ matrix $\mathbf{M} = \mathbf{T}\,\mathbf{s}^{-1/2}$ which satisfies $\mathbf{M}^t\mathbf{M} = \mathbf{s}^{-1}$ and $\mathbf{M}^t\mathbf{S}\mathbf{M} = \mathbb{1}$, the generalized eigenvalue problem (2.44) is rewritten as the ordinary eigenvalue problem

$$\tilde{\mathbf{H}}_0(\theta)\tilde{\mathbf{\Psi}}_\theta = E_\theta\tilde{\mathbf{\Psi}}_\theta\,, \tag{2.45}$$

where

$$\tilde{\mathbf{H}}_0(\theta) = \mathbf{M}^t\mathbf{H}_0(\theta)\mathbf{M}\,, \tag{2.46}$$

and

$$\tilde{\mathbf{\Psi}}_\theta = \mathbf{M}^{-1}\mathbf{\Psi}_\theta\,, \tag{2.47}$$

are respectively a $(p\times p)$ matrix and a $(p\times 1)$ vector. The diagonalization of the eigenvalue problem (2.45) is performed using the Lanczos algorithm (see Appendix A.1).

2.3.3 Convergence of the method

The basis expansion in (2.29) is truncated through the inclusion of a finite number of angular configurations (l_1, l_2), each one with a definite number of sets of Coulomb-Sturmain functions defined by $\{\kappa_{1s}, N_{1s}^{\min}, N_{1s}^{\max}, \kappa_{2s}, N_{2s}^{\min}, N_{2s}^{\max}\}$. The dilation parameters are chosen as $\kappa_{1s} \approx 2/N$ and $\kappa_{2s} \approx 2/n_s$, with N and n_s the excitations of the inner and

			$(N^{\max}, l^{\max})$					
N	k	n	$(20,20)$	$(35,20)$	$(20,10)$	$(50,10)$	Conv. value	Ref. data
2	1	2	0.777 859 288	0.777 866 287	0.777 859 120	0.777 865 731	0.777 86	0.777 867 636
		3	0.589 895 519	0.589 894 121	0.589 895 259	0.589 893 988	0.589 89	0.589 894 682
		4	0.544 881 668	0.544 881 365	0.544 881 502	0.544 881 277	0.544 881	0.544 881 618
		5	0.526 686 778	0.526 686 719	0.526 686 674	0.526 686 660	0.526 686	0.526 686 857
		6	0.517 641 034	0.517 641 029	0.517 640 966	0.517 640 988	0.517 641	0.517 641 112
		7	0.512 513 418	0.512 513 434	0.512 513 373	0.512 513 406	0.512 513 4	0.512 513 488
	-1	2	0.621 889 630	0.621 908 891	0.621 874 067	0.621 892 766	0.621 9	0.621 927 254
		3	0.548 080 087	0.548 082 997	0.548 078 277	0.548 080 125	0.548 08	0.548 085 535
		4	0.527 714 277	0.527 715 551	0.527 713 560	0.527 714 310	0.527 71	0.527 716 640
		5	0.518 103 005	0.518 103 681	0.518 102 647	0.518 103 032	0.518 10	0.518 104 252
		6	0.512 762 701	0.512 762 906	0.512 763 297	0.512 763 126	0.512 763	0.512 763 242
		7	0.509 483 621	0.509 483 355	0.509 483 498	0.509 483 113	0.509 483	0.509 483 569

Table 2.4.: Energies (in atomic units) for doubly excited ^{1}S states below the $N = 2$ ionization threshold obtained after diagonalization of (2.45). The states are organized according Herrick's classification [75,76,80] to be compared with reference data from [79]. Results without analysis of converged digits and converged values are shown.

the outer electron, respectively. The values for n_s determine the excitation of the outer electron in the energy region of interest, while $N_{1s}^{\min}$, $N_{1s}^{\max}$, $N_{2s}^{\min}$ and $N_{2s}^{\max}$ satisfy

$$N_{1s}^{\min} < N < N_{1s}^{\max}\,, \tag{2.48}$$

$$N_{2s}^{\min} < n_s < N_{2s}^{\max}\,. \tag{2.49}$$

Table 2.4 displays the energies of doubly excited ^{1}S states below the $N = 2$ ionization threshold. These values have been obtained after diagonalization of (2.45) with complex rotation angle $\theta = 0.15$ and $l_1^{\max} = l_2^{\max} = l^{\max}$, i.e., $(1 + l^{\max})$ angular configurations. In each case we use the sets $\{1.00, 1, N^{\max}, 1.00, 1, N^{\max}\}$, $\{1.00, 1, N^{\max}, 0.50, 1, N^{\max}\}$ and $\{1.00, 1, N^{\max}, 0.33, 1, N^{\max}\}$. In particular, these results have been tested with respect to the variation of the parameters $N^{\max}$ and $l^{\max}$. The numerical data presented in the rest of the work have also been subject to a stability analysis with respect to varying values of the dilation parameters κ_{1s} and κ_{2s}, and complex rotation angle θ. In our convergence analysis we have also found so far unreported states. We present them in Appendix B.1.

The data in Table 2.4 reveals that by increasing the excitation of the outer electron the convergence improves. This is due to the influence of the Kato cusp[3] [92, 93] which is more important for symmetrically excited configurations.

[3]This is a discontinuity of the derivative of the wavefunction at $r_{12} = 0$, which is not resolvable within our approach [71].

2.4 Helium atom under periodic driving

Now we consider the helium atom in presence of an external electromagnetic field. In the dipole approximation and neglecting relativistic effects, the Hamiltonian for the driven atom reads

$$\begin{aligned} H &= H_0 + F(x_1 + x_2)\cos(\omega t)\,, \\ H &= H_0 - \frac{F}{\mathrm{i}\omega}\left(\frac{\partial}{\partial x_1} + \frac{\partial}{\partial x_2}\right)\sin(\omega t)\,, \end{aligned} \tag{2.50}$$

in the position and velocity gauge, respectively [38]. Here, H_0 is the unperturbed Hamiltonian (2.2) and the field is linearly polarized along the x direction and periodic in time with amplitude F and frequency ω.

2.4.1 Floquet theory

Since the Hamiltonian (2.50) is periodic in time, with period $T = 2\pi/\omega$, the Floquet theorem [68, 69] guarantees that the solutions of the time-dependent Schrödinger equation

$$\mathrm{i}\frac{\partial}{\partial t}|\psi(t)\rangle = H|\psi(t)\rangle\,, \tag{2.51}$$

can be expressed as a superposition of time-periodic wave functions

$$|\psi(t)\rangle = \sum_i c_i e^{-\mathrm{i}\varepsilon_i t}|\phi_{\varepsilon_i}(t)\rangle, \qquad |\phi_{\varepsilon_i}(t+T)\rangle = |\phi_{\varepsilon_i}(t)\rangle\,,$$

where ε_i and $|\phi_{\varepsilon_i}(t)\rangle$ are the eigenvalues and eigenstates of the Floquet Hamiltonian $\mathcal{H}_F = H - \mathrm{i}\frac{\partial}{\partial t}$, called *quasienergies* and *Floquet states*, respectively.

The Floquet states are periodic in time, therefore, they can be expanded in Fourier series

$$|\phi_{\varepsilon_i}(t)\rangle = \sum_{k=-\infty}^{\infty} e^{-\mathrm{i}k\omega t}|\phi_{\varepsilon_i}^k\rangle\,. \tag{2.52}$$

In this way, the eigenvalue problem $\mathcal{H}_F|\phi_{\varepsilon_i}(t)\rangle = \varepsilon_i|\phi_{\varepsilon_i}(t)\rangle$, reduces to

$$(H_0 - k\omega)|\phi_{\varepsilon_i}^k\rangle + \mathcal{F}(|\phi_{\varepsilon_i}^{k+1}\rangle + \eta|\phi_{\varepsilon_i}^{k-1}\rangle) = \varepsilon_i|\phi_{\varepsilon_i}^k\rangle\,, \tag{2.53}$$

where $\eta = \pm$ in the position and velocity gauge, respectively, and

$$\mathcal{F} = \begin{cases} \frac{F}{2}(x_1 + x_2), & \text{in the position gauge,} \\ \frac{F}{2\omega}\left(\frac{\partial}{\partial x_1} + \frac{\partial}{\partial x_2}\right), & \text{in the velocity gauge.} \end{cases} \tag{2.54}$$

With the Floquet method, the time dependence has been eliminated, and we have a new quantum number k. In the limit of a large number of photons there is a one-to-one correspondence between the quasienergy spectrum of the Floquet Hamiltonian and the energy spectrum of an atom dressed by a quantized field [69, 94]. The amount of photons exchanged between the atom and the field is then given by the Floquet quantum number k.

2.4.2 Numerical treatment

In Section 2.4.1, we show that using Floquet theory, the TDSE (2.51) which describes the helium atom under periodic driving can be written as the eigenvalue problem (2.53), where the time dependence was eliminated and was introduced a new quantum number k. The matrix representation of Eq. (2.53) is given by

$$\mathbf{A}\Phi_i = \varepsilon_i \Phi_i \,, \qquad \mathbf{A} = \mathbf{H}_0 - k\omega \mathbb{1} + \mathbf{F} \,, \tag{2.55}$$

with Φ_i the column vector representing $|\phi_i^k\rangle$ and $\mathbf{F}$ the matrix representation of (2.54).

The general form of matrix $\mathbf{A}$ is depicted in Figure 2.5 (left). The matrix $\mathbf{H}_0$ is symmetric and has a block diagonal structure. On the other hand, the matrix $\mathbf{F}$ is symmetric in the position gauge but it is antisymmetric in the velocity gauge, with a block structure where only elements for which $\Delta L = \pm 1$ and $\Delta k = \pm 1$ are coupled.

The numerical implementation requires a truncation in the number of Floquet blocks and angular momenta included in the computation according to

$$k_{\min} \leq k \leq k_{\max}, \qquad L = 0, \ldots, L_{\max} \,. \tag{2.56}$$

In previous investigations of nondispersive wave packets in planar helium [39], equation (2.55) has been solved directly in the same harmonic oscillator basis presented in Section 2.2.3. In that basis, the block matrix $\mathbf{H}_0$ have only few terms different from zero due to the selection rules in (n_1, n_2, n_3, n_4). However, even for a small number of Floquet blocks and low values of angular momenta, the large size of the matrix $\mathbf{A}$ makes the computations time and memory consuming [39, 95]. As a consequence, it was not possible to provide a full picture of the NDWP or their decaying properties. For instance, for $n_{\text{base}} = 200$, $k_{\min} = -2$, $k_{\max} = 4$ and $L_{\max} = 3$ the matrix size is $n_{\text{tot}} = 521\,795$, while the RAM memory necessary to store the matrices is of the order of 430 GB.

In the three-dimensional case, where the matrices are given in the Sturmian basis of Section 2.3, the block matrix $\mathbf{H}_0$ is completely full. In such a way, the complete characterization of NDWP in planar helium and the generalization to the 3D case demands a reduction of the size of the matrices involved in the computations. This is

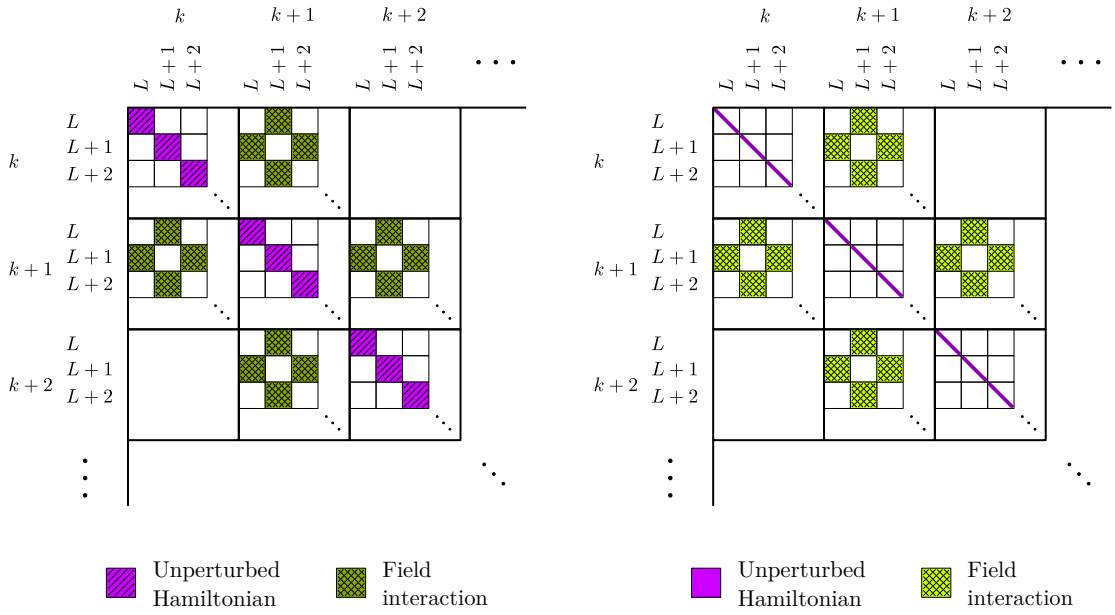


Figure 2.5.: Schematic block structure of the Hamiltonian matrices $\mathbf{A}$ (left) of the eigenvalue problem (2.55) and $\tilde{\mathbf{A}}$ (right) of the eigenvalue problem (2.59).

possible in the so-called atomic basis [70] (the basis in which the atomic Hamiltonian H_0 is diagonal).

Time-dependent Schrödinger equation in the atomic basis

Let us consider the atomic states $|\varphi_i^L\rangle$ which satisfy the time-independent Schrödinger equation

$$H_0|\varphi_i^L\rangle = \epsilon_i^L|\varphi_i^L\rangle\,, \tag{2.57}$$

where H_0 is the unperturbed Hamiltonian (2.2) and L is the total angular momentum. The solution of this equation for planar and three-dimensional helium is achieved using the approaches of Sections 2.2 and 2.3, respectively.

Once we have obtained the states $|\varphi_i^L\rangle$, we can define the atomic basis adapted to solve the eigenvalue problem (2.53) by

$$\{|\varphi_i^{L,k}\rangle\}, \qquad |\varphi_i^{L,k}\rangle = |k\rangle \otimes |\varphi_i^L\rangle\,, \tag{2.58}$$

where the identification of the Floquet quantum number k with the number of photons exchanged between the atom and the field discussed in Section 2.4.1 allows us to write the above tensor product.

In the basis (2.58), the eigenvalue problem (2.55) writes

$$\tilde{\mathbf{A}}\tilde{\Phi}_i = \varepsilon_i \tilde{\Phi}_i \,, \qquad \tilde{\mathbf{A}} = \mathbf{h}_0 - k\omega\mathbb{1} + \tilde{\mathbf{F}} \,, \tag{2.59}$$

where $\tilde{\Phi}_i$ is the solution vector in the atomic basis, $\mathbf{h}_0$ is the diagonal matrix containing the eigenvalues of $\mathbf{H}_0$, and the matrix $\tilde{\mathbf{F}}$ —which has the same structure of $\mathbf{F}$— contains the dipole elements involved in the computation of oscillator strengths in Appendix B.2. The general form of the matrix $\tilde{\mathbf{A}}$ is shown in Figure 2.5 (right). This matrix is sparser than the matrix $\mathbf{A}$ and does not have the singularities of the latter in the three-dimensional case due to the overcompleteness of the Coulomb-Sturmian basis (see Section 2.3.2).

As in the unperturbed system, the diagonalization of the eigenvalue problem (2.59) is performed using the Lanczos algorithm described in Appendix (A.1).

The principal features of this method, as we will see in Section 4.2, are the tremendous reduction in the size of the matrices (with all the benefits that this entails from the computational point of view) and the possibility to identify the atomic states involved in the formation of NDWP, which allows us to reduce the system to its very basic ingredients.

2.5 Quantum entanglement in helium

Entanglement is one of the most significant characteristics in the quantum mechanical description of multipartite systems [96] and plays an important role in understanding fundamental phenomena such as quantum correlations [97]. Motivated not only for the interest on the foundations of quantum mechanics but also for the possible technological applications in quantum information, quantum computing [98], quantum cryptography [99], and quantum teleportation [100] there has been an increasing activity in the entanglement properties in atomic systems. In this regard, the helium atom enjoys an important place. It is the simplest naturally available atomic species which contains the electron-electron interaction, and, therefore a natural candidate for the investigation of entanglement properties in atoms.

In this section we present the entanglement measure used in Chapter 5 to characterize the correlation properties of doubly excited states and nondispersive wave packets in planar helium.

2.5.1 Entanglement measure

For a pure state $|\Phi\rangle$ of two identical fermions, the Schmidt decomposition is given by [101, 102]

$$|\Phi\rangle = \sum_i \sqrt{\frac{\lambda_i}{2}} \left(|2i\rangle|2i+1\rangle - |2i+1\rangle|2i\rangle\right) , \tag{2.60}$$

where the λ_i are called the Schmidt coefficients, which satisfy $0 \leq \lambda_i \leq 1$ and $\sum_i \lambda_i = 1$. The decomposition (2.60) leads to a useful measure of the amount of entanglement exhibited by the two-fermion state, namely [102, 103]

$$\mathcal{E}(|\Phi\rangle) = 1 - \sum_i \lambda_i^2 = 1 - 2\mathrm{Tr}(\rho_1^2) , \tag{2.61}$$

where $\rho_1 = \mathrm{Tr}_2(|\Phi\rangle\langle\Phi|)$ is the single-particle reduced density matrix obtained by taking the trace over one of the particles. If the state $|\Phi\rangle$ can be expressed as a single Slater determinant, the entanglement measure (2.61) vanishes, i.e., the state has no entanglement [102–104]. For maximally entangled states $\mathcal{E}(|\Phi\rangle) = 1$.

In this work, we are interested in applying the measure (2.61) to a state of a two-electron system. To do that we consider states described by wave functions of the form

$$\Phi = \Psi(\vec{r}_1, \vec{r}_2)\chi(1,2) , \tag{2.62}$$

where $\Psi(\vec{r}_1, \vec{r}_2)$ and $\chi(1,2)$ correspond to the coordinate and spin wave functions, respectively. The corresponding density matrix reads

$$\rho = \rho^{(\mathrm{coord.})} \otimes \rho^{(\mathrm{spin})} . \tag{2.63}$$

Evaluating the entanglement measure (2.61) on the state described by (2.62), we obtain

$$\mathcal{E}(|\Psi\rangle) = 1 - 2\mathrm{Tr}\left[(\rho_1^{(\mathrm{coord.})})^2\right] \mathrm{Tr}\left[(\rho_1^{(\mathrm{spin})})^2\right] , \tag{2.64}$$

where $\rho_1^{(\mathrm{coord.})} = \mathrm{Tr}_2(\rho^{(\mathrm{coord.})})$ and $\rho_1^{(\mathrm{spin})} = \mathrm{Tr}_2(\rho^{(\mathrm{spin})})$. In order to evaluate (2.64) we need to consider separately the cases of a spin wave function describing parallel spins or antiparallel spins:

- In the case of parallel spins, the coordinate wave function is antisymmetric, and the spin wave function can be χ_{++} or χ_{--}, thus

$$\mathrm{Tr}\left[(\rho_1^{(\mathrm{spin})})^2\right] = 1 , \tag{2.65}$$

and the measure (2.64) reduces to

$$\mathcal{E}(|\Psi\rangle) = 1 - 2\int d\vec{r}_1{}' d\vec{r}_1 |\langle \vec{r}_1{}'|\rho_1^{(\mathrm{coord.})}|\vec{r}_1\rangle|^2 \,. \tag{2.66}$$

- If the spins are anti-parallel, the coordinate wave function is symmetric and the spin wave function is $\frac{1}{2}\left(\chi_{+-} - \chi_{-+}\right)$, or we have alternatively that the coordinate wave function is antisymmetric and the spin wave function is $\frac{1}{2}\left(\chi_{+-} + \chi_{-+}\right)$. In either case we have

$$\mathrm{Tr}\left[(\rho_1^{(\mathrm{spin})})^2\right] = \frac{1}{2}\,, \tag{2.67}$$

and

$$\mathcal{E}(|\Psi\rangle) = 1 - \int d\vec{r}_1{}' d\vec{r}_1 |\langle \vec{r}_1{}'|\rho_1^{(\mathrm{coord.})}|\vec{r}_1\rangle|^2 \,. \tag{2.68}$$

The expression for $\langle \vec{r}_1{}'|\rho_1^{(\mathrm{coord.})}|\vec{r}_1\rangle$ in (2.66) and (2.68) is given by

$$\langle \vec{r}_1{}'|\rho_1^{(\mathrm{coord.})}|\vec{r}_1\rangle = \int_{-\infty}^{\infty} d\vec{r}_2\, \Psi(\vec{r}_1{}', \vec{r}_2)\Psi^*(\vec{r}_1, \vec{r}_2)\,. \tag{2.69}$$

To calculate the entanglement measures (2.66) or (2.68), we need to evaluate the quantity $\mathrm{Tr}\left[(\rho_1^{(\mathrm{coord.})})^2\right]$ which is given by the 12-dimensional definite integral

$$\begin{aligned}
\mathrm{Tr}\left[(\rho_1^{(\mathrm{coord.})})^2\right] &= \int_{\mathbb{R}^6} d\vec{r}_1{}' d\vec{r}_1 \left| \int_{\mathbb{R}^3} d\vec{r}_2\, \Psi(\vec{r}_1{}', \vec{r}_2)\Psi^*(\vec{r}_1, \vec{r}_2)\right|^2 , \\
&= \int_{\mathbb{R}^{12}} d\vec{r}_1{}' d\vec{r}_1 d\vec{r}_2{}' d\vec{r}_2\, \Psi(\vec{r}_1{}', \vec{r}_2)\Psi^*(\vec{r}_1, \vec{r}_2)\Psi^*(\vec{r}_1{}', \vec{r}_2{}')\Psi(\vec{r}_1, \vec{r}_2{}')\,.
\end{aligned} \tag{2.70}$$

For the investigation of quantum entanglement in planar helium, the above expression corresponds to a 8-dimensional definite integral. We perform this calculation using the VEGAS algorithm included in the Cuba library[4] [105, 106]. VEGAS is widely used for Monte Carlo multidimensional numerical integration and is primarily based on importance sampling, but it also does some stratified sampling as a variance-reduction technique. The algorithm iteratively builds up a piecewise constant weight function, represented on a rectangular grid, which is refined after each iteration. Further details can be found in [107].

[4]The source code is available from http://feynarts.de/cuba.

Frozen planet states of helium

3

The basic properties of the classical frozen planet configuration are introduced in Section 3.1, followed by the identification of frozen planet states in the energy spectrum of planar and three-dimensional helium in Section 3.2. In particular we present results for singlet and triplet states with total angular momentum $L = 0$ and $L = 1$ in the energy regime up to the 7th ionization threshold.

3.1 Classical frozen planet configuration

The classical *frozen planet configuration* (FPC) is an asymmetric configuration where both electrons are located on the same side of the nucleus (Figure 3.1 (left)). In this highly asymmetric configuration, which is dynamically stable [21, 34, 108], the inner electron precesses on highly eccentric ellipses and the outer electron remains nearly “frozen" around some equilibrium distance.

The phase space of the frozen planet configuration presented in Figure (3.1) (right), is visualized within a Poincaré surface of section obtained by plotting the position x_1 and the momentum p_1 of the outer electron every time the inner electron reaches the nucleus. The numerical computation of the classical dynamics is achieved by previous regularization of the equations of motion by Kustaanheimo-Stiefel transformations [109, 110].

Within the formalism of adiabatic invariants [111], the fast Kepler oscillations of the inner electron define an effective attractive potential which describes the dynamics of the outer electron. From the shape of this potential, we can extract the intrinsic frequency and amplitude scales which determine the effect of an external driving field on the configuration [37, 112]. The position $x_{\min}$ of the minimum of the effective potential, the minimum energy $E_{\min}$, the intrinsic frequency scale ω_{I}, and the intrinsic field strength F_{I} for the FPC, in atomic units, are,

$$\begin{aligned} x_{\min} &= 2.6S^2\,, & \omega_{\mathrm{I}} &= 0.3S^{-3}\,, \\ E_{\min} &= -2.22S^{-2}\,, & F_{\mathrm{I}} &= 0.03S^{-4}\,, \end{aligned} \tag{3.1}$$

where $S = \frac{1}{2\pi}\oint p_2 dx_2$ is the action integral over one cycle of the Kepler oscillation of the inner electron, with x_2 and p_2 its position and momentum, respectively. The natural scale F_{I} for the field strength is given by the maximum slope of the effective potential and defines the minimum static field necessary to ionize the configuration. The frequency

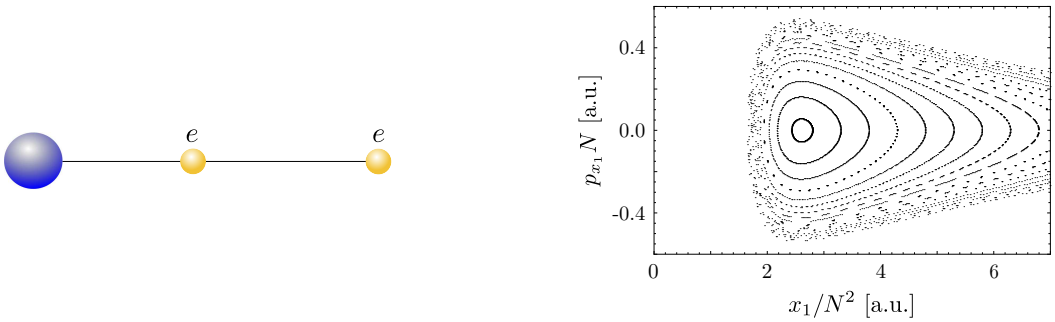


Figure 3.1.: Collinear frozen planet configuration of helium (left). Phase space of the outer electron in the frozen planet configuration (right).

scale ω_{I} is given by the curvature of the potential at its minimum. This is the frequency of small oscillations around the equilibrium position.

In a quantum description, the action S is replaced by the effective quantum number of the inner electron, and the scaled quantities (3.1) take the form

$$x_{\min} = 2.6(N-\delta)^2\,, \tag{3.2}$$
$$\omega_{\mathrm{I}} = 0.3(N-\delta)^{-3}\,, \tag{3.3}$$
$$E_N = -2.22(N-\delta)^{-2}\,, \tag{3.4}$$
$$F_{\mathrm{I}} = 0.03(N-\delta)^{-4}\,, \tag{3.5}$$

where $\delta = 0.5$ [73] and $\delta = 0$ for 2D and 3D helium, respectively.

The existence of *frozen planet states* (FPS) (which are the quantum counterpart of the FPC) have been demonstrate theoretically on 1D [37], 2D [39, 113] and 3D [35] helium for $N \geq 3$. However, these states have so far not been unambiguously identified in experiments, though sequential multiphoton excitation schemes [114–116] have successfully been used for the creation of planetary states [19] where highly excited electrons move in different regions of space ($\langle \vec{r}_2 \rangle < \langle \vec{r}_1 \rangle$).

Identification of frozen planet states

Frozen planet states are localized along a collinear configuration, thus for these states, the expectation value of the cosine of the angle θ_{12} between the two electrons has to be close to unity ($\langle \cos\theta_{12} \rangle \simeq 1$). In addition, FPS have long lifetimes compared to other resonances in the same energy regime. In this way, we can use the decay rates and the expectation value of $\cos\theta_{12}$ to identify quantum states along classical frozen planet trajectories in helium spectra. However, these two quantities do not fully characterize

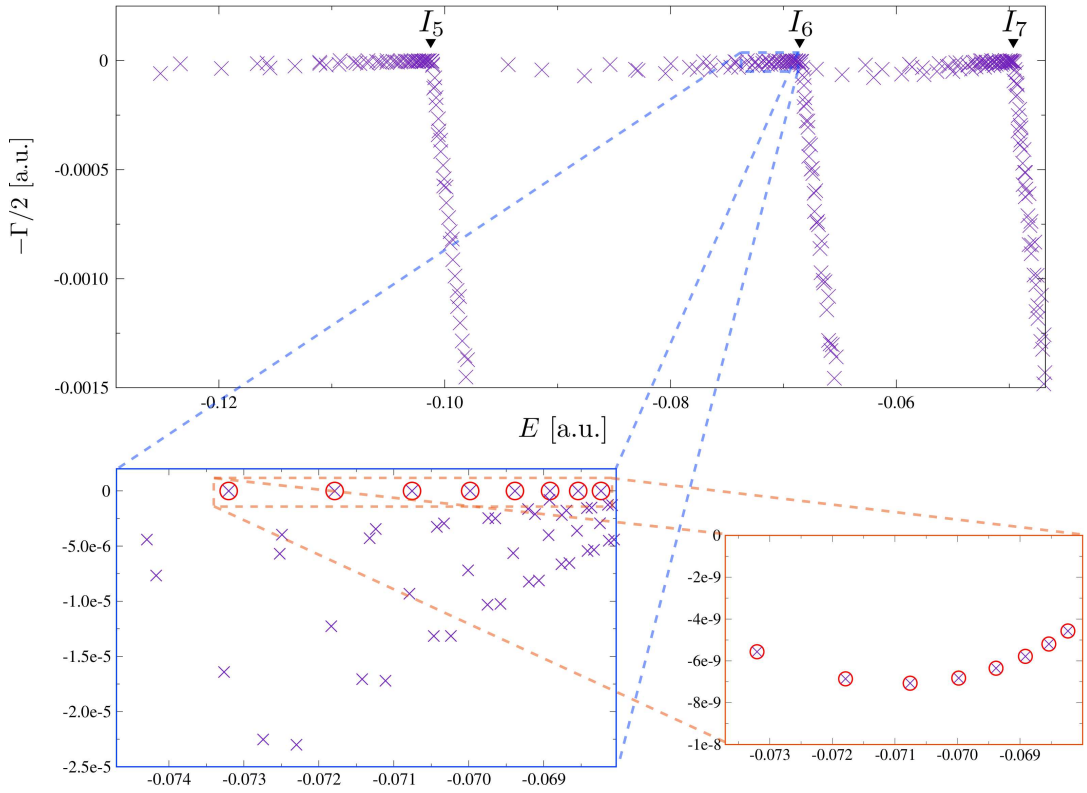


Figure 3.2.: Complex ^{3}S spectrum of the unperturbed planar helium atom in the energy region below the $N = 5, 6$ and 7 ionization thresholds. Frozen planet states of the 6th series are identified with red circles.

the FPS, and their unambiguous identification also requires the study of the localization properties of the electronic density in configuration space and phase space.

Due to the high dimensionality of the configuration and phase spaces, the visualization of the wave function requires the use of projections of the probability density. The visualization in configuration space is achieved using conditional probability distributions for $\theta_{12} = 0$ or one-electron probability densities, while for analysis of the electronic density in phase space we use Husimi distributions (see Appendix A.3).

3.2 Frozen planet states of 2D and 3D helium

Our principal interest is to study frozen planet states of helium under near resonant driving. In this direction, the first step is to identify the FPS in the spectrum of the unperturbed atom. Frozen planet states are organized in series converging to single ionization thresholds I_N and can be denoted by $\mathcal{F}^N_{n_F}$, where N corresponds to the

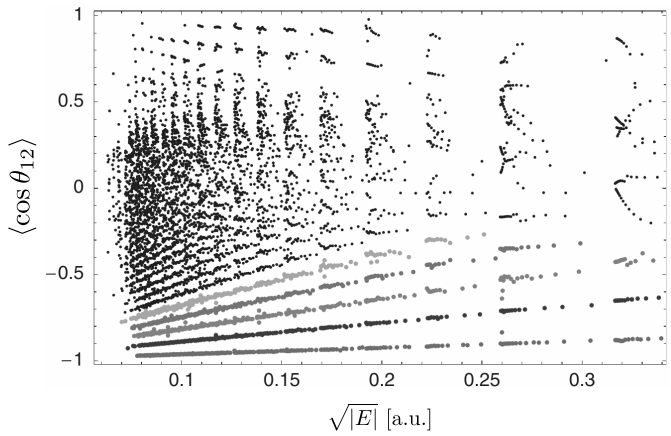


Figure 3.3.: Values of $\langle \cos\theta_{12} \rangle$ as a function of energy up to the 20th ionization threshold for ^{3}P states of planar helium. Taken from [117].

principal quantum number of the inner electron and n_F indicates the position of the FPS in the series.

We diagonalize the unperturbed Hamiltonian H_0 for planar and three-dimensional helium, in the energy region below the $N = 3, \ldots, 7$ ionization thresholds for angular momentum $L = 0$ and $L = 1$. In the energy spectrum obtained, we identify the lowest FPS of the series converging to each ionization threshold. Figure 3.2 shows the energy spectrum of the unperturbed planar helium in the energy region below the $N = 5, 6$ and 7 ionization thresholds for ^{3}S states. In the plot, frozen planet states of the $N = 6$ series are identified with red circles. As we can observe these states are characterized by small decay rates compared to the other resonances.

FPS are also characterized by the expectation value of the cosine of the angle θ_{12} between the two electrons. Figure 3.3 displays the values of $\langle \cos\theta_{12} \rangle$ as a function of $\sqrt{|E|}$ below I_4 up to I_{20} for ^{3}P states of planar helium. For $\langle \cos\theta_{12} \rangle \lesssim -0.5$, doubly excited states gather into series labeled by $F = N - K$, where N and K are approximate quantum numbers from Herrick's classification [75, 76, 80]. Furthermore, for highly doubly excited states we can also identify well defined series for the case of antisymmetric states ($\langle \cos\theta_{12} \rangle \gtrsim 0.5$). From the relation $K \to -N\langle \cos\theta_{12} \rangle$ [76, 118], the classical eZe configuration is associated with $K_{\max} = N - 1$ whereas that $K_{\min} = -(N - 1)$ is identified with the classical Zee configuration which corresponds to the frozen planet configuration.

In Table 3.1 we present the energies of the ground ($n_F = 1$) FPS compared with the semiclassical values obtained by Eq. (3.4). As N increases, quantum results are closer to the semiclassical energies. This is not surprising since the semiclassical regime of the Coulomb potential is located at energies close to the double ionization threshold

	2D			3D		
N	$-E_N$ [a.u.]	$-E(^1\mathrm{S})$ [a.u.]	$-E(^3\mathrm{S})$ [a.u.]	$-E_N$ [a.u.]	$-E(^1\mathrm{S})$ [a.u.]	$-E(^3\mathrm{S})$ [a.u.]
3	0.355 20	0.354 907 546	0.352 128 587	0.246 67	0.257 370 27	0.249 964 64
4	0.181 22	0.180 560 506	0.180 360 430	0.138 75	0.141 067 41	0.140 088 58
5	0.109 63	0.109 297 551	0.109 260 500	0.088 80	0.089 571 26	0.089 467 88
6	0.073 39	0.073 207 046	0.073 203 013	0.061 67	0.062 053 80	0.062 041 26
7	0.052 54	0.052 445 661	0.052 443 726	0.045 31	0.045 539 29	0.045 539 23

Table 3.1.: Energies of the ground $^1\mathrm{S}$ and $^3\mathrm{S}$ frozen planet states for $N = 3, \ldots, 7$ in planar and three-dimensional helium. The semiclassical values E_N are obtained from Eq. (3.4).

[119, 120]. In addition, the singlet-triplet energy splitting due to particle exchange effects which is not considered in the semiclassical prediction decreases exponentially with N [113].

Table 3.2 shows the energies, decay rates and $\langle \cos\theta_{12} \rangle$ for the first four singlet 2D and 3D frozen planet states for $L = 0, 1$ and $N = 3, \ldots, 7$, while Table 3.3 gives the same quantities for triplet frozen planet states. The decay rates of the 2D and 3D FPS have comparable values, while the values of $\langle \cos\theta_{12} \rangle$ are larger in the planar case, which is expected as the restriction to the plane reduces the possible transverse deviations from the collinear configuration. In both 2D and 3D cases, for $N \geq 5$ the $L = 0$ FPS posses small decay rates and largest value of $\langle \cos\theta_{12} \rangle$ compared with $L = 1$ FPS. We observe also that $\langle \cos\theta_{12} \rangle$ increases with N and n_F, consistent with the semiclassical character of the highly doubly excited states.

In Figure 3.4 we present the conditional ($\theta_{12} = 0$) probability density [1] of the lowest ^1S FPS below the $N = 4$ single ionization threshold for planar and three-dimensional helium. The inner electron labeled by the index 2 is close to the nucleus while the outer electron labeled by the index 1 is far from the nucleus. For the ground FPS, the maximum of the probability density is localized near the equilibrium position $x_{\min}$ of the outer electron in the classical configuration given by Eq. (3.2). In the case of excited FPS, the maximum of the probability density along the inner electron axis remains at the same position whereas that the maximum along the outer electron axis increases with n_F.

Each plot in Figure 3.5 is composed of two parts. The left part corresponds to the inner electron density for a fixed position of the outer electron, while the right part shows the outer electron density for a fixed position of the inner electron. The value for the

[1] From the rotational invariance of the helium atom, the probability distributions depend only on the relative position of the electrons. Thus, for a given angle θ_{12} it is always possible to choose r_1 to be the Cartesian coordinate x_1, what automatically determines r_2. In particular, for $\theta_{12} = 0$ the conditional probability is obtained from the general electronic density (A.5) by substituting $r1 = x1$ and $r2 = x2$, with $x_1 \geq 0$, $x_2 \geq 0$, and $y_1 = y_2 = 0$.

N	n_F	$-E$ [a.u.]		$\Gamma/2$ [a.u.]		$\langle\cos\theta_{12}\rangle$	
		2D	3D	2D	3D	2D	3D
				^{1}S states			
3	1	0.354 907 546	0.257 370 27	0.000 003 373	0.000 007 12	0.672	0.352
	2	0.342 496 485	0.244 323 59	0.000 0004 76	0.000 020 27	0.676	0.448
	3	0.335 495 095	0.237 310 39	0.000 000 073	0.000 016 42	0.680	0.469
	4	0.331 264 862	0.233 173 07	0.000 000 071	0.000 011 94	0.681	0.484
4	1	0.180 560 506	0.141 067 41	0.000 000 877	0.000 010 79	0.788	0.534
	2	0.175 705 103	0.137 091 40	0.000 001 483	0.000 001 77	0.785	0.552
	3	0.172 615 385	0.134 230 69	0.000 001 593	0.000 002 29	0.782	0.573
	4	0.170 535 543	0.132 214 01	0.000 001 452	0.000 003 04	0.781	0.584
5	1	0.109 297 551	0.089 571 26	0.000 003 748	0.000 002 07	0.772	0.712
	2	0.106 832 792	0.087 561 17	0.000 000 062	0.000 006 12	0.853	0.540
	3	0.105 139 500	0.086 099 22	0.000 000 179	0.000 000 60	0.862	0.608
	4	0.103 925 428	0.085 007 53	0.000 000 337	0.000 000 53	0.864	0.607
6	1	0.073 207 046	0.062 053 80	0.000 010 180	0.000 000 54	0.950	0.747
	2	0.071 801 931	0.060 840 80	0.000 006 145	0.000 000 92	0.902	0.740
	3	0.070 770 672	0.059 938 86	0.000 002 634	0.000 001 26	0.884	0.749
	4	0.069 994 857	0.059 247 33	0.000 001 482	0.000 000 92	0.882	0.783
7	1	0.052 445 661	0.045 539 29	0.000 001 443	0.000 000 07	0.888	0.780
	2	0.051 561 367	0.044 762 80	0.000 002 240	0.000 001 44	0.894	0.782
	3	0.050 887 178	0.044 172 97	0.000 001 949	0.000 005 89	0.895	0.656
	4	0.050 361 468	0.043 697 51	0.000 001 562	0.000 003 39	0.898	0.701
				^{1}P states			
3	1	0.348 950 783	0.245 517 49	0.000 000 088	0.000 000 04	0.616	0.496
	2	0.338 858 835	0.238 061 59	0.000 000 055	0.000 000 08	0.608	0.515
	3	0.333 238 049	0.233 663 16	0.000 000 035	0.000 000 08	0.599	0.520
	4	0.329 797 285	0.230 864 50	0.000 000 024	0.000 000 07	0.591	0.520
4	1	0.179 248 594	0.138 613 88	0.000 001 534	0.000 000 40	0.693	0.600
	2	0.174 807 889	0.135 102 26	0.000 001 010	0.000 000 14	0.691	0.617
	3	0.171 980 605	0.132 774 21	0.000 000 669	0.000 000 04	0.690	0.625
	4	0.170 073 973	0.131 159 88	0.000 000 465	0.000 000 02	0.688	0.628
5	1	0.108 773 791	0.088 845 26	0.000 005 206	0.000 002 91	0.680	0.672
	2	0.106 479 587	0.086 939 07	0.000 002 816	0.000 001 70	0.716	0.694
	3	0.104 884 000	0.085 578 31	0.000 002 000	0.000 001 31	0.732	0.699
	4	0.103 734 973	0.084 576 54	0.000 001 206	0.000 000 46	0.741	0.696
6	1	0.073 044 134	0.061 734 15	0.000 002 573	0.000 007 67	0.818	0.735
	2	0.071 713 237	0.060 593 31	0.000 007 305	0.000 006 37	0.762	0.757
	3	0.070 726 659	0.059 735 22	0.000 009 997	0.000 004 05	0.722	0.756
	4	0.069 972 887	0.059 075 38	0.000 010 269	0.000 003 08	0.703	0.759
7	1	0.052 351 581	0.045 366 34	0.000 000 361	0.000 002 76	0.869	0.728
	2	0.051 498 957	0.044 626 42	0.000 001 302	0.000 004 31	0.867	0.721
	3	0.050 846 645	0.044 056 63	0.000 003 033	0.000 003 57	0.848	0.759
	4	0.050 336 417	0.043 601 08	0.000 004 942	0.000 002 57	0.823	0.770

Table 3.2.: Energies, decay rates and $\langle\cos\theta_{12}\rangle$ for the four lowest ^{1}S and ^{1}P frozen planet states for $N = 3, \ldots, 7$ in planar and three-dimensional helium.

N	n_F	$-E$ [a.u.]		$\Gamma/2$ [a.u.]		$\langle\cos\theta_{12}\rangle$	
		2D	3D	2D	3D	2D	3D
				^{3}S states			
3	1	0.352 128 587	0.249 964 64	0.000 001 529	0.000 006 77	0.427	0.402
	2	0.340 903 255	0.240 314 51	0.000 001 835	0.000 003 46	0.468	0.488
	3	0.334 395 783	0.234 969 60	0.000 000 992	0.000 002 02	0.531	0.526
	4	0.330 517 901	0.231 692 13	0.000 000 601	0.000 001 28	0.563	0.547
4	1	0.180 360 430	0.140 088 58	0.000 000 418	0.000 004 39	0.760	0.507
	2	0.175 457 936	0.135 975 61	0.000 001 558	0.000 001 74	0.613	0.570
	3		0.133 329 31		0.000 001 33		0.565
	4		0.131 533 78		0.000 001 08		0.555
5	1	0.109 260 500	0.089 467 88	0.000 000 021	0.000 000 18	0.839	0.707
	2	0.106 794 314	0.087 357 10	0.000 000 037	0.000 000 25	0.838	0.705
	3	0.105 099 702	0.085 868 25	0.000 000 046	0.000 000 27	0.835	0.701
	4	0.103 887 667	0.084 784 66	0.000 000 049	0.000 000 28	0.832	0.694
6	1	0.073 203 013	0.062 041 26	0.000 000 006	0.000 000 03	0.869	0.757
	2	0.071 788 666	0.060 811 30	0.000 000 007	0.000 000 07	0.871	0.761
	3	0.070 756 000	0.059 894 51	0.000 000 007	0.000 000 10	0.872	0.761
	4	0.069 980 757	0.059 194 97	0.000 000 007	0.000 000 09	0.872	0.761
7	1	0.052 443 726	0.045 539 23	0.000 000 130	0.000 000 39	0.888	0.794
	2	0.051 557 442	0.044 756 85	0.000 000 088	0.000 000 11	0.891	0.798
	3	0.050 882 036	0.044 151 06	0.000 000 065	0.000 000 06	0.893	0.801
	4	0.050 355 907	0.043 673 21	0.000 000 049	0.000 000 05	0.895	0.802
				^{3}P states			
3	1	0.349 389 074	0.246 059 66	0.000 000 130	0.000 000 17	0.690	0.528
	2	0.339 211 003	0.238 512 99	0.000 000 135	0.000 000 11	0.726	0.576
	3	0.333 485 926	0.233 991 44	0.000 000 101	0.000 000 07	0.745	0.601
	4	0.329 971 022	0.231 100 33	0.000 000 072	0.000 000 05	0.755	0.616
4	1	0.179 424 139	0.138 884 13	0.000 008 708	0.000 041 22	0.775	0.594
	2	0.174 965 590	0.135 339 62	0.000 001 044	0.000 003 18	0.801	0.640
	3	0.172 105 472	0.132 957 76	0.000 000 312	0.000 000 93	0.818	0.679
	4	0.170 170 487	0.131 302 66	0.000 000 143	0.000 000 44	0.829	0.699
5	1	0.108 873 521	0.091 868 72	0.000 006 070	0.000 001 27	0.776	0.409
	2	0.106 618 280	0.088 990 76	0.000 007 045	0.000 001 98	0.585	0.561
	3	0.104 979 719	0.087 026 81	0.000 003 584	0.000 005 47	0.777	0.541
	4	0.103 806 525	0.085 745 64	0.000 001 699	0.000 005 40	0.821	0.553
6	1	0.073 024 843	0.061 679 97	0.000 003 008	0.000 000 62	0.836	0.605
	2	0.071 671 979	0.060 523 13	0.000 006 616	0.000 000 88	0.833	0.582
	3	0.070 675 246	0.059 665 06	0.000 009 262	0.000 000 87	0.780	0.569
	4		0.059 011 26		0.000 000 64		0.559
7	1	0.052 349 313	0.0453 35 27	0.000 001 742	0.000 000 40	0.657	0.647
	2	0.051 493 345	0.0445 91 38	0.000 003 555	0.000 000 65	0.881	0.646
	3	0.050 837 398	0.0440 16 35	0.000 004 744	0.000 000 78	0.892	0.641
	4	0.050 324 264	0.0435 62 70	0.000 004 666	0.000 000 77	0.887	0.638

Table 3.3.: Energies, decay rates and $\langle\cos\theta_{12}\rangle$ for the four lowest ^{3}S and ^{3}P frozen planet states for $N = 3, \ldots, 7$ in planar and three-dimensional helium. In the case of $N = 4$ only two ^{3}S FPS have been identified for planar helium.

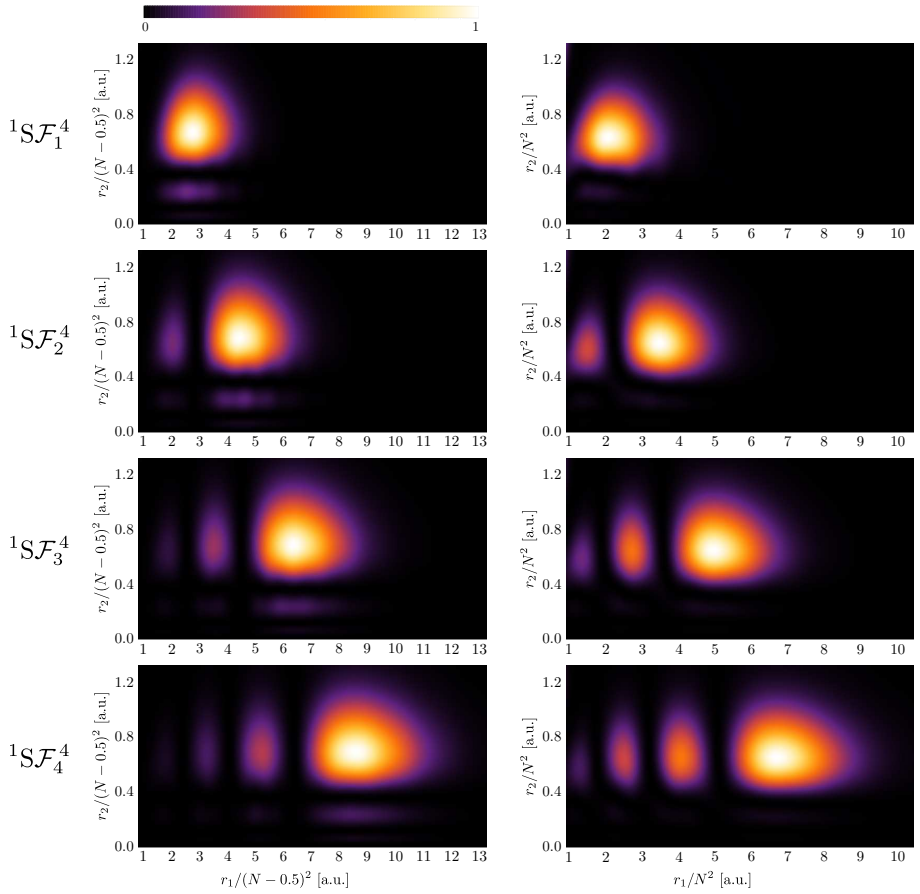


Figure 3.4.: Conditional probability density ($\theta_{12} = 0$) of the lowest $^1\mathrm{S}$ frozen planet states of the $N = 4$ series in planar (left) and three-dimensional helium (right). For the ground FPS, the maximum of the probability density is localized near the equilibrium position $x_{\min}$ of the outer electron in the classical configuration (Eq. (3.2)). For excited FPS, the maximum of the probability density along the inner electron axis r_2 remains at the same position while the maximum along the outer electron axis r_1 increases with n_F.

position of the fixed electron is given by the maximum of the conditional probability density of Figure 3.4 for the respective electron.

Figure 3.6 displays the Husimi distributions (see Appendix A.3) of the first four $^1\mathrm{S}$ FPS converging to the 6th series for planar and three-dimensional helium. Comparing these plots with the classical configuration, we observe that the maximum of the probability density of the ground state is localized at the equilibrium position of the outer electron in the classical FPC given by Eq. (3.2). On the other hand, excited FPS are localized along periodic orbits with higher energy of the classical configuration.

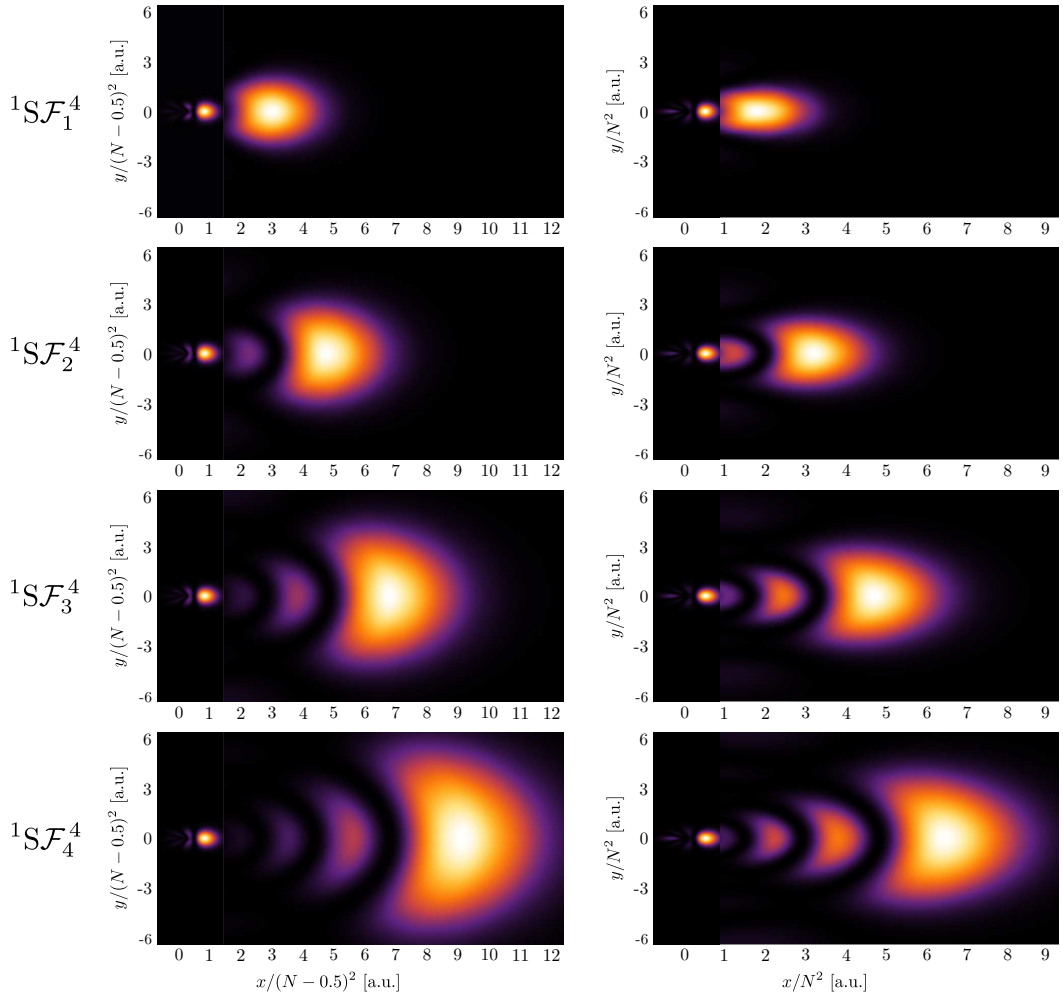


Figure 3.5.: Projections in configuration space for the electronic density of the $^1\mathrm{S}$, $N = 4$ frozen planet states in planar (left) and three-dimensional helium (right). In each plot, the left part corresponds to the inner electron density for a fixed position of the outer electron, while the right part shows the outer electron density for a fixed position of the inner electron. The value for the position of the fixed electron is given by the maximum of the conditional probability density of Figure 3.4 for the respective electron.

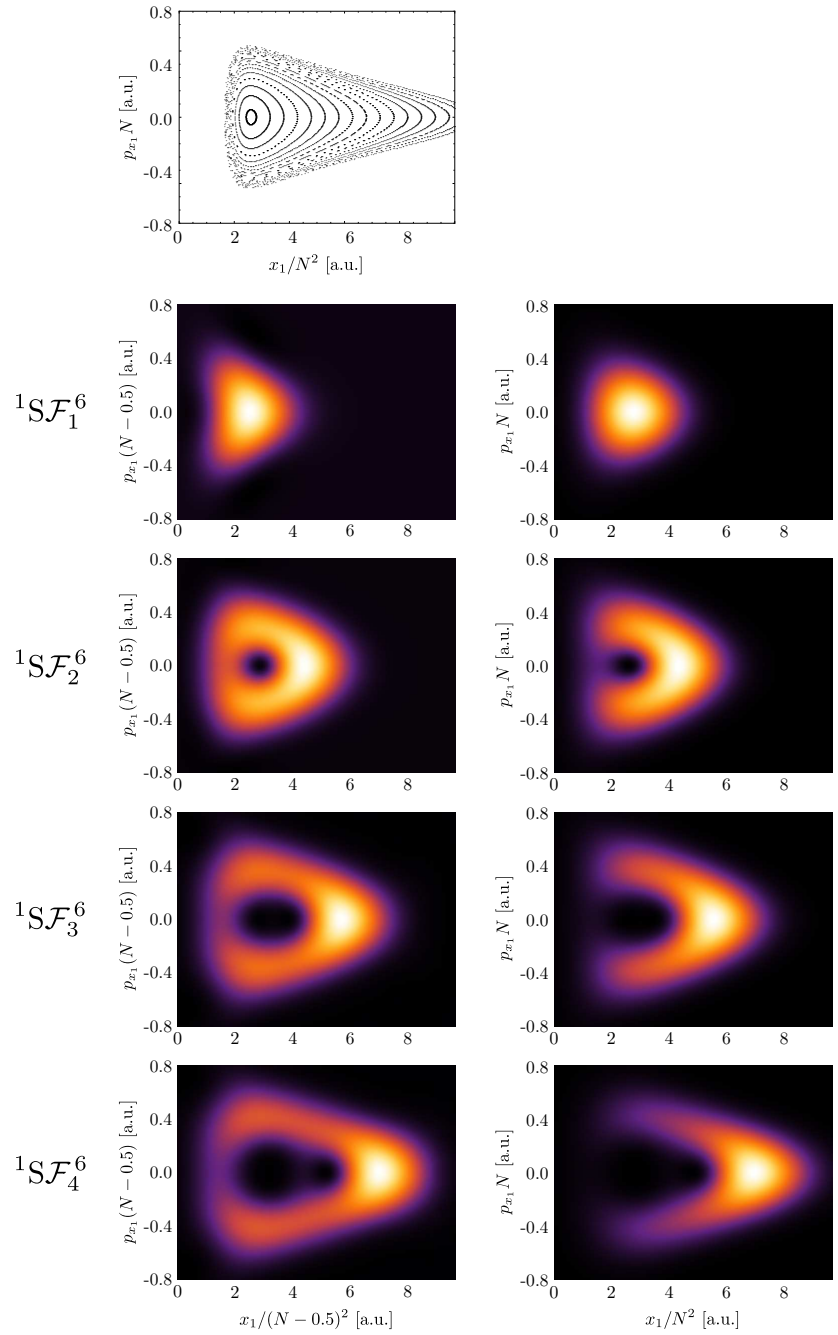


Figure 3.6.: Projections in phase space for the electronic density of the $^1\mathrm{S}$ frozen planet states of the $N = 6$ series in planar (left) and three-dimensional (right) helium. For comparison, we show the classical phase space structure (top). For the ground FPS $^1\mathrm{S}\mathcal{F}_1^6$ the maximum of the probability density is localized at the equilibrium position of the outer electron in the classical FPC, while for excited FPS, the maximum of the probability density is localized along periodic orbits with higher energy of the classical configuration.

4 Nondispersive wave packets (NDWP) in helium

In this chapter, we study the dynamics of driven frozen planet states of helium and the formation of nondispersive wave packets. In Section 4.1 a general description of the driven frozen planet configuration is presented. In Section 4.2, we characterize nondispersive wave packets in planar helium, identifying the principal ingredients involved in their formation. Finally, in Section 4.3 we give for first time theoretical evidence of the existence of nondispersive wave packets in three-dimensional helium, including a brief discussion related to their experimental identification.

4.1 Driven frozen planet configuration

In the presence of an external time-periodic electromagnetic field, the dynamics of the collinear frozen planet configuration takes place in a five-dimensional phase space described by the positions and momenta of the electrons, and by the phase ωt of the driving field.

For near resonant driving $\omega \approx \omega_{\rm I} = 0.3(N-\delta)^{-3}$ of amplitude $F < F_{\rm I} = 0.03(N-\delta)^{-4}$, which do not affect in a sensitive way the frozen planet dynamics, the time scale separation between the fast Kepler oscillations of the inner electron and the slow motion of the outer electron makes possible to map the phase space structure onto a two-dimensional surface by a two-step Poincaré section method [36, 108]. The first Poincaré section is obtained by plotting the position x_1 and momentum p_1 of the outer electron each time the inner electron hits the nucleus at $x_2 = 0$. The resulting points, which describe the slow outer electron's oscillation are connected by cubic interpolation to construct a continuous trajectory, used to perform a second Poincaré section by fixing the phase of the driving field $\omega t = \phi_0 \,(\mathrm{mod}\, 2\pi)$.

In Figure 4.1 is depicted the two-step Poincaré surface of section obtained for fixed field frequency $\omega = 0.2N^{-3}$ a.u. and different field amplitudes. In the left plot, the field amplitude is $F = 0$, and we have the same regular phase space of Figure 3.1 (right). For field amplitude $F = 0.001N^{-4}$ a.u. in the center plot, the phase space becomes mixed with regular and chaotic regions. At the position $x_1 = 4.8N^2$ a.u., we can identify a substructure which corresponds to the 1:1 resonance. At larger field amplitude in the right plot ($F = 0.005N^{-4}$ a.u.), the induced resonance separates from the rest of the

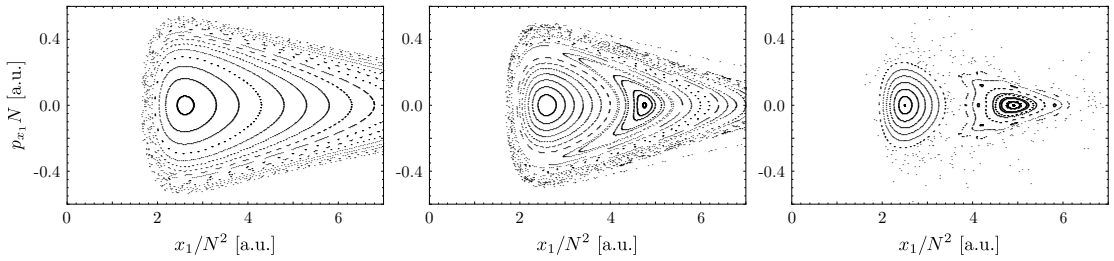


Figure 4.1.: Phase space of the driven frozen planet configuration for fixed field frequency $\omega = 0.2N^{-3}$ a.u. and three different field amplitudes: $F = 0$ a.u. (left), $F = 0.001N^{-4}$ a.u. (center) and $F = 0.005N^{-4}$ a.u. (right).

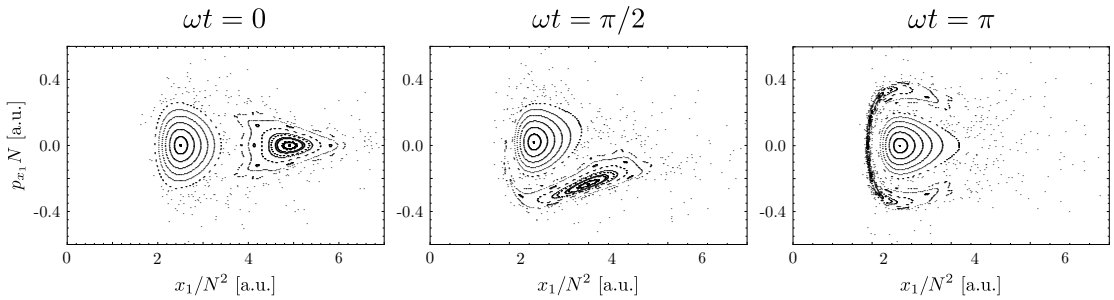


Figure 4.2.: Phase space of the driven frozen planet configuration for field amplitude $F = 0.005N^{-4}$ a.u., frequency $\omega = 0.2N^{-3}$ a.u. and variable driving field phases ωt.

regular domain and the phase space exhibits two regular islands: the *intrinsic* island and the *resonance* island, which are embedded into the chaotic sea and are localized at the positions $x_1 = 2.5N^2$ a.u. and $x_1 = 4.9N^2$ a.u., respectively.

Figure 4.2 shows the classical phase space structure for field amplitude $F = 0.005N^{-4}$ a.u. and frequency $\omega = 0.2N^{-3}$ a.u., for three different field phases ωt. The intrinsic island remains basically unaffected by the field while the resonance island oscillates around the intrinsic island with the same field frequency.

4.2 Nondispersive wave packets in 2D helium

4.2.1 Identification of NDWP below the 6th ionization threshold

In this section, we study doubly excited states of planar helium under periodic driving. The main interest is to verify the applicability of the method presented in Section 2.4.2 to investigate driven frozen planet states and to identify nondispersive wave packets in helium.

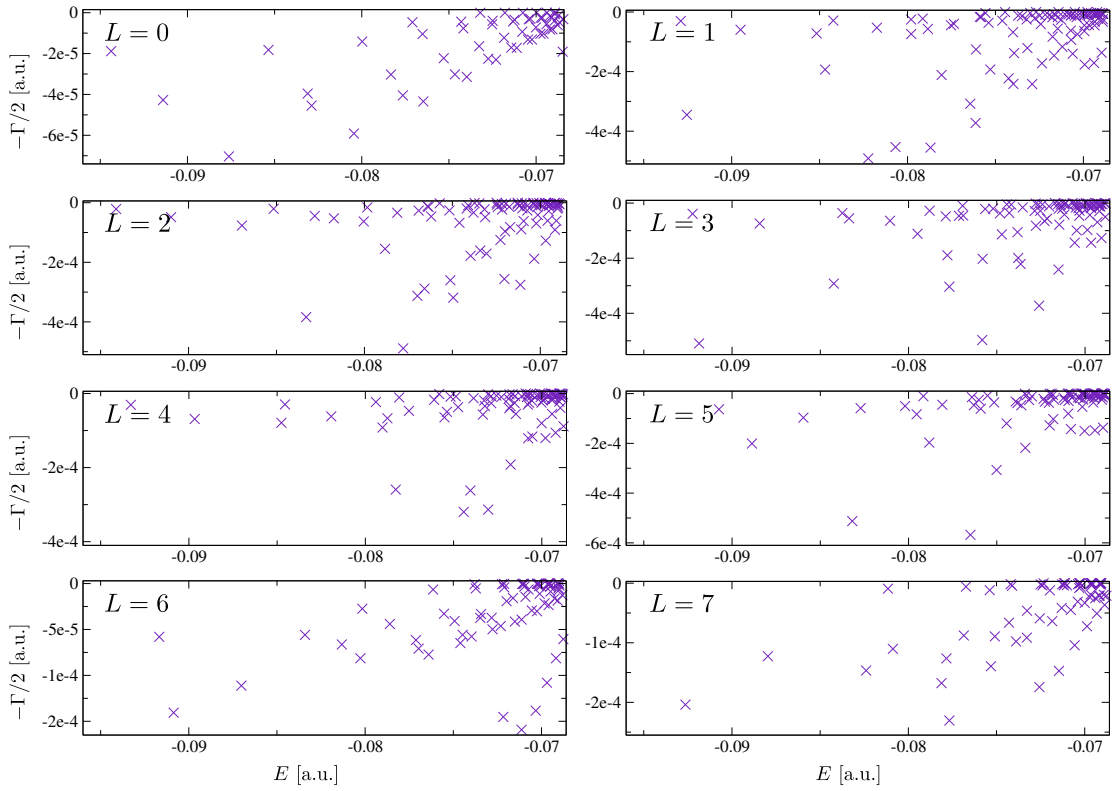


Figure 4.3.: Complex energy spectrum of the unperturbed helium atom for triplet states in the energy region below the 6th ionization threshold, obtained after diagonalization of (2.21) for $n_{\mathrm{base}} = 250$ and different angular momenta.

There is evidence for the existence of nondispersive wave packets in the energy region below the $N = 6$ ionization threshold of planar helium [39]. Hence, we start our study of driven frozen planet states precisely in that energy region, with special attention on the lowest triplet (^{3}S) FPS of the $N = 6$ series (Table 3.3). The same analysis presented in this section leads to the description of NDWP for other symmetries and ionization thresholds. The results are discussed in Section 4.2.4.

As mentioned in Section 2.4.2, our approach is based on two principal steps. First, we diagonalize the unperturbed Hamiltonian for $L = 0, \ldots, L_{\mathrm{max}}$ (each one of these calculations is performed independently since for the unperturbed atom the angular momentum is a conserved quantity). Figure 4.3 displays the complex spectrum for triplet states converging to the 6th ionization threshold obtained by diagonalization of Eq. (2.21), for $n_{\mathrm{base}} = 250$ and $L = 0, \ldots, 7$.

In the second step, the numerical investigation of the driven atom is achieved by solving the eigenvalue problem (2.59). The matrix to diagonalize is expressed in the atomic basis (2.58), which is build up using the states in Figure 4.3 and 15 Floquet blocks

($k_{\min} = -7$ and $k_{\max} = 7$), i.e., we study the dynamics of the atomic states obtained in the previous step, under the action of the external field. For the electromagnetic driving, we use the field frequency $\omega = 0.0012$ a.u. and field amplitude $F = 5.5 \times 10^{-6}$ a.u., which induce the well pronounced 1:1 resonance and intrinsic island in the classical phase space in Figure 4.1 (right). The result was tested for convergence by repeating the calculations for atomic bases obtained with different values of the complex rotation angle θ and the dilation parameter α as in Section 2.2.4. In particular we use the sets (θ, α): $(0.25, 0.45)$, $(0.30, 0.45)$, $(0.35, 0.40)$ and $(0.40, 0.35)$.

The Floquet eigenstates obtained by diagonalization of Eq. (2.59), are given by a superposition of atomic states. Hence, we can identify the states for which the greatest contribution in the atomic basis is given by a frozen planet state $\mathcal{F}_j^N$, i.e., the Floquet states $|\psi\rangle$ with the largest overlap $|\langle \mathcal{F}_j^N | \psi \rangle|^2$. We denote them by $\mathcal{W}_j^N$.

Figure 4.4 shows the projected Husimi distributions of the Floquet eigenstates with the largest overlap with the lowest $(^3\mathrm{S})$ FPS in the sixth series of the field free atom. The state $\mathcal{W}_1^6$ follows the same oscillation of the intrinsic island in the classical structure (bottom). On the other hand, the states $\mathcal{W}_2^6$ and $\mathcal{W}_3^6$, anchored to the hyperbolic and elliptic fixed points of the 1:1 resonance, respectively, oscillate around the intrinsic island with the same field frequency.

Figure 4.5 shows the electronic density in configuration space for the Floquet states $\mathcal{W}_1^6$, $\mathcal{W}_2^6$ and $\mathcal{W}_3^6$. In the three cases, we observe that the probability density of the inner electron is not affected by the field, while the probability density of the outer electron oscillates with the driving frequency.

The above results reproduce the dynamics of the nondispersive wave packets identified in reference work [39, 95], where, the dynamics of the lowest triplet $(^3\mathrm{S})$ FPS of the $N = 6$ series under periodic driving was studied by solving Eq. (2.53) for $k_{\min} = -2$, $k_{\max} = 4$ and $L_{\max} = 3$ in a harmonic oscillator basis of 521 795 elements. It is worth to mention that despite the large size of the basis used, they have not been able to obtain a converged value of the wave packets decay rates, while we obtained converged values (presented in Table 4.2) with a small basis of only 4 366 elements. One of the advantages of our method is that we can identify the atomic states that contribute to the formation of the NDWP. This will be clear in the next section.

4.2.2 Principal characteristics of NDWP below the 6th ionization threshold

In the previous section, we have seen that it is possible to study the dynamics of FPS under electromagnetic driving in an efficient way, using an expansion in a basis set of a

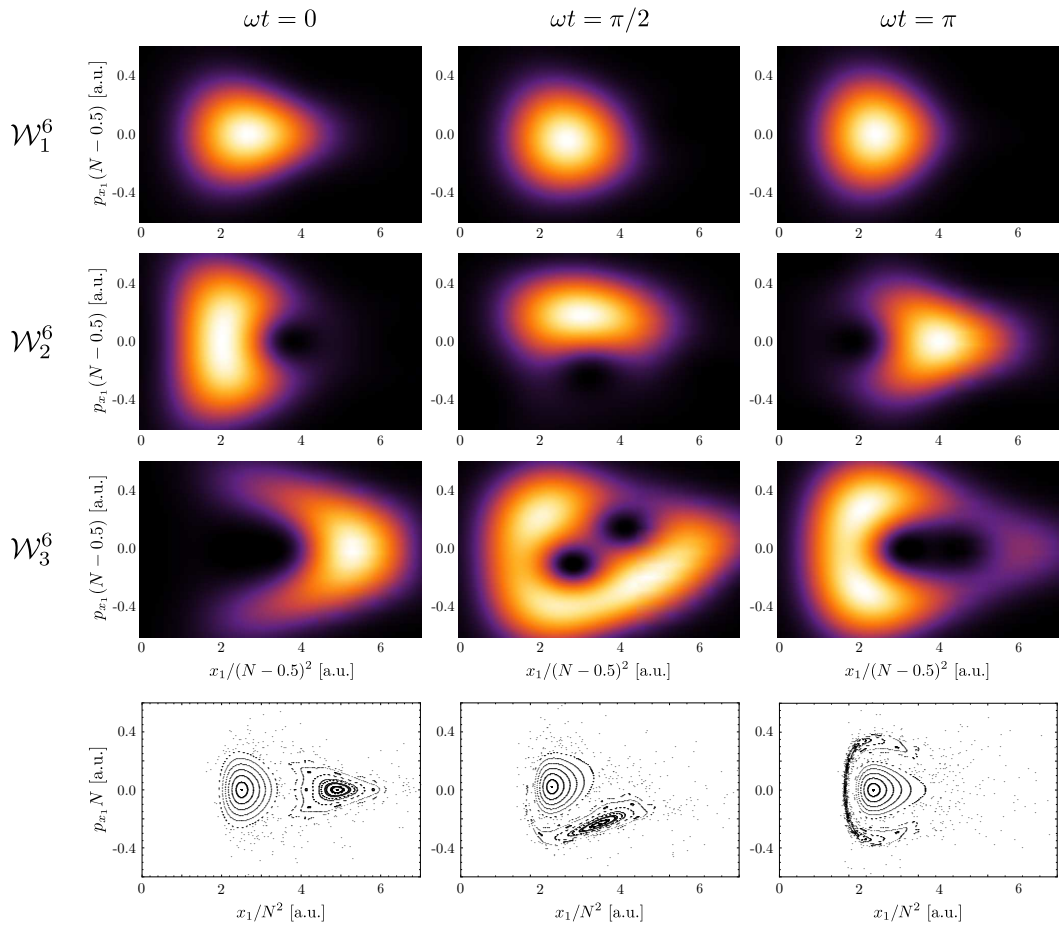


Figure 4.4.: Husimi distributions of the triplet wave packets $\mathcal{W}_1^6$, $\mathcal{W}_2^6$ and $\mathcal{W}_3^6$ obtained for field parameters $F = 5.5 \times 10^{-6}$ a.u. and $\omega = 0.0012$ a.u., depicted for different phases of the driving field. For comparison, we show the classical phase space structure obtained for the same field parameters (bottom).

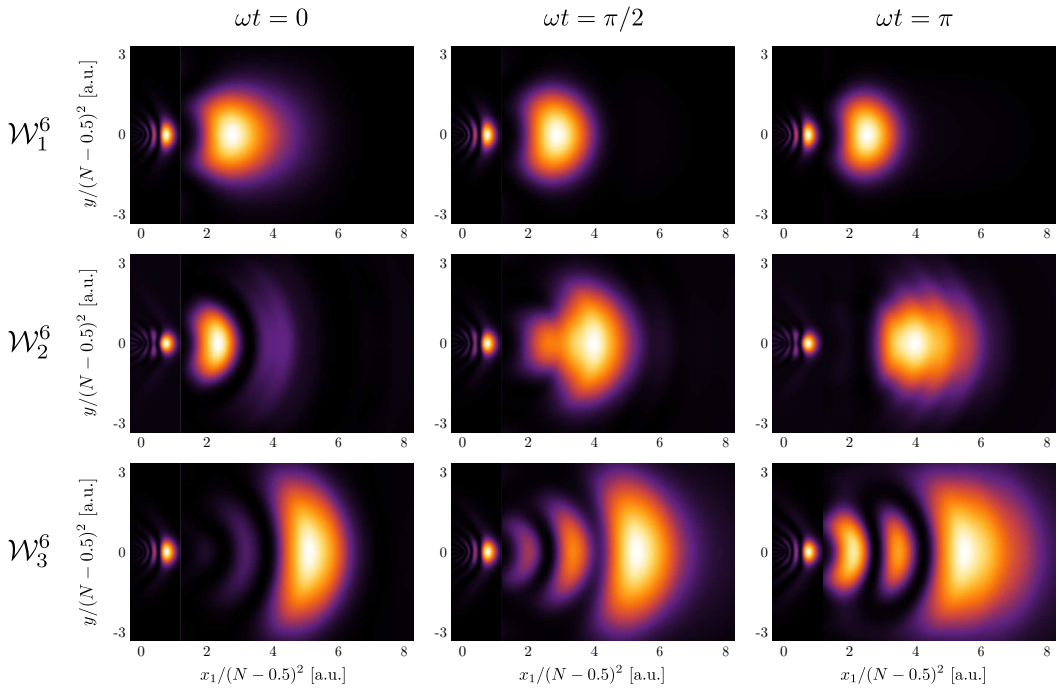


Figure 4.5.: Projections in configuration space of the electronic density of the same wave packets presented in Figure 4.4. In each plot, the left part shows the inner electron density, while the right part shows the outer electron density.

relatively small number of atomic eigenstates. Here, we study in more detail the NDWP identified in the previous section, with the aim of determining which of the atomic states have the most relevant participation in the process of formation of NDWP in helium.

Following the notation introduced in Section 4.2.1, we identify the Floquet eigenstates with the largest overlap with the lowest ^{3}S FPS in the 6th series of the field free atom as $\mathcal{W}_j^6$. In order to quantify the contribution of the atomic eigenstates $|\varphi_i^{L,k}\rangle$ in the basis (2.58) to each wave packet $\mathcal{W}_j^6$, we calculate the overlaps $|\langle\varphi_i^{L,k}|\mathcal{W}_j^6\rangle|^2$, i.e., the square modulus of the components of the Floquet eigenstate $\mathcal{W}_j^6$. Here, we present our analysis for the wave packet $\mathcal{W}_2^6$. The results for the wave packets $\mathcal{W}_1^6$ and $\mathcal{W}_3^6$ are qualitatively similar.

Figure 4.6 shows the overlaps for the wave packet $\mathcal{W}_2^6$ and the basis elements for field amplitude $F = 5.5 \times 10^{-6}$ a.u. and frequency $\omega = 0.0012$ a.u.. In the top figures, we observe that the principal contribution comes from the atomic states with lower angular momentum. In particular, the Floquet state $\mathcal{W}_2^6$ has the largest overlap with the frozen planet states $^3\mathrm{S}\mathcal{F}_2^6$ (63%) and $^3\mathrm{P}\mathcal{F}_1^6$ (27%). The overlaps decrease with L. In particular, the contributions from $L = 7$ angular momentum states are eight orders of magnitude

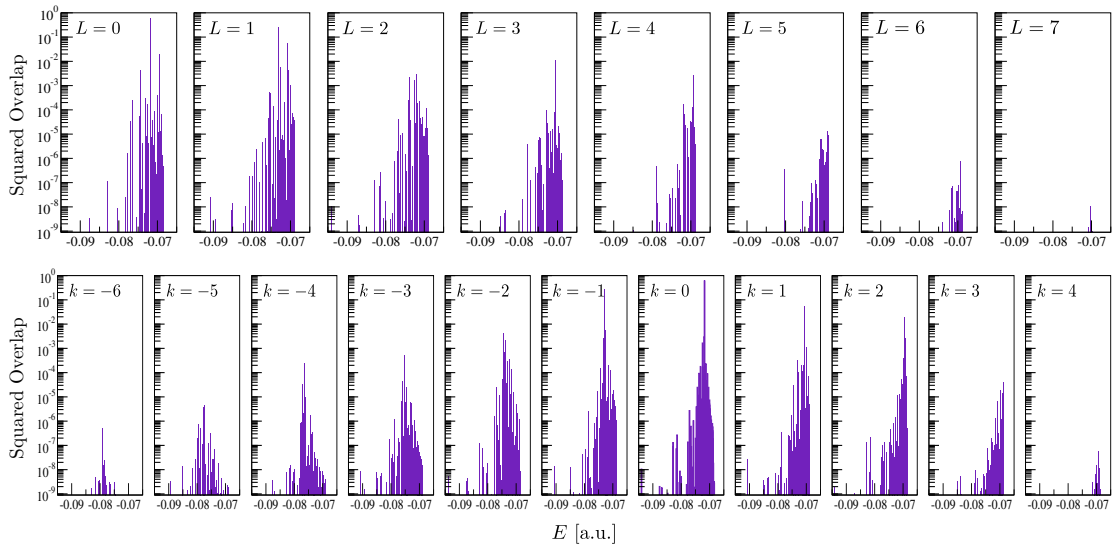


Figure 4.6.: Overlaps of the wave packet $\mathcal{W}_2^6$ with the states of the atomic basis organized according to angular momentum L (top) and the Floquet number k (bottom). Driving field parameters: $F = 5.5 \times 10^{-6}$ a.u. and $\omega = 0.0012$ a.u..

smaller than for $L = 0$. Thus, we do not expect significant contribution for atomic states of angular momentum $L = 8$ or greater.

In Figure 4.6 (bottom), the overlaps are organized according to the Floquet number k and we see that the main contribution is given by the atomic states in the Floquet blocks from $k = -2$ to $k = 2$. In addition, we observe that the contribution from atomic states in the Floquet block $k = 4$ is seven orders of magnitude smaller than for $k = 0$, which is expected since the number of photons to reach the 6th ionization threshold from the frozen planet state ${}^3\mathrm{S}\mathcal{F}_2^6$ is four.

In Figure 4.7, we present the energies (left) and decay rates (right) of the Floquet spectrum as a function of the field amplitude F for fixed field frequency $\omega = 0.0012$ a.u.. In the limit $F = 0$, the Floquet eigenstates correspond to unperturbed states with energy E shifted by $k\omega$. By increasing the field amplitude, the Floquet eigenstates are given by a superposition of atomic states and energy levels shift due to the repulsion between coupled Floquet states. Green, blue and red circles identify the states $\mathcal{W}_1^6$, $\mathcal{W}_2^6$ and $\mathcal{W}_3^6$, respectively. In the left plot, for $F > 2 \times 10^{-6}$ a.u., the energy of the states $\mathcal{W}_1^6$ and $\mathcal{W}_2^6$ exhibit a pronounced shift at positive slope, which is associated to a large dipole moment of the electronic density in configuration space[1]. In the right plot, we show the imaginary part of the Floquet spectrum, which corresponds to the half of the decay rates Γ. In this plot, we observe that the decay rate of the Floquet eigenstate $\mathcal{W}_3^6$ remains approximately

[1] According to the Hellmann–Feynman theorem [122, 123], the slope is proportional to the expectation value of the electronic dipole $\langle x_1 + x_2 \rangle$.

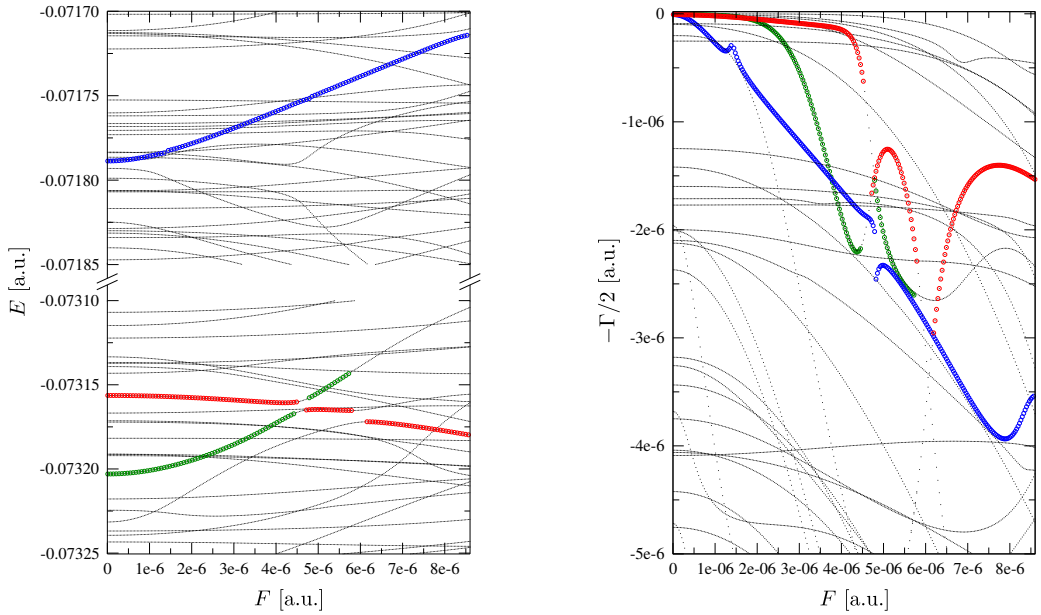


Figure 4.7.: Behaviour of the energies E (left) and decay rates Γ (right) as a function of the field amplitude F, for driving frequency $\omega = 0.0012$ a.u.. Green, blue and red circles identify the wave packets $\mathcal{W}_1^6$, $\mathcal{W}_2^6$ and $\mathcal{W}_3^6$, respectively. For field amplitudes $F > 5.7 \times 10^{-6}$ a.u., there are no Floquet eigenstates with the largest overlap with the FPS ${}^3\mathrm{S}\mathcal{F}_1^6$.

constant for $F < 4 \times 10^{-6}$ a.u., and for field amplitudes around $F = 5 \times 10^{-6}$ a.u. and $F = 7 \times 10^{-6}$ a.u., the decay rate exhibits abrupt changes due to avoided crossings. For the case of the states $\mathcal{W}_1^6$ and $\mathcal{W}_2^6$, the decay rates show a pronounced shift at negative slope. Thus, the tendency of these decay rates is to increase with the field amplitude.

Figure 4.8 shows the overlaps between the wave packet $\mathcal{W}_2^6$ and the elements in the basis for different field parameters. The green region identifies the intervals for the field amplitude (left) and frequency (right), where the Floquet state $\mathcal{W}_2^6$ exhibits the nondispersive behaviour. To establish this region, we calculated the Husimi distributions of the triplet wave packet $\mathcal{W}_2^6$ for the different field parameters, verifying that the dynamics shown in Figure 4.4 was reproduced. Similar results were observed for the wave packets $\mathcal{W}_1^6$ and $\mathcal{W}_3^6$. However, this is not conclusive, since by varying the field frequency (amplitude) the green region in the left (right) plot can change. Thus, the complete characterization of the wave packet behaviour in terms of the field parameters requires the simultaneous variation of F and ω.

In the left plot in Figure 4.8, the overlaps are calculated as a function of the field amplitude F for fixed frequency $\omega = 0.0012$ a.u.. There, we observe that in the limit $F = 0$ the overlap with the frozen planet state ${}^3\mathrm{S}\mathcal{F}_2^6$ is equal to one, which means that the Floquet state $\mathcal{W}_2^6$ has only one component in the atomic basis, given by the

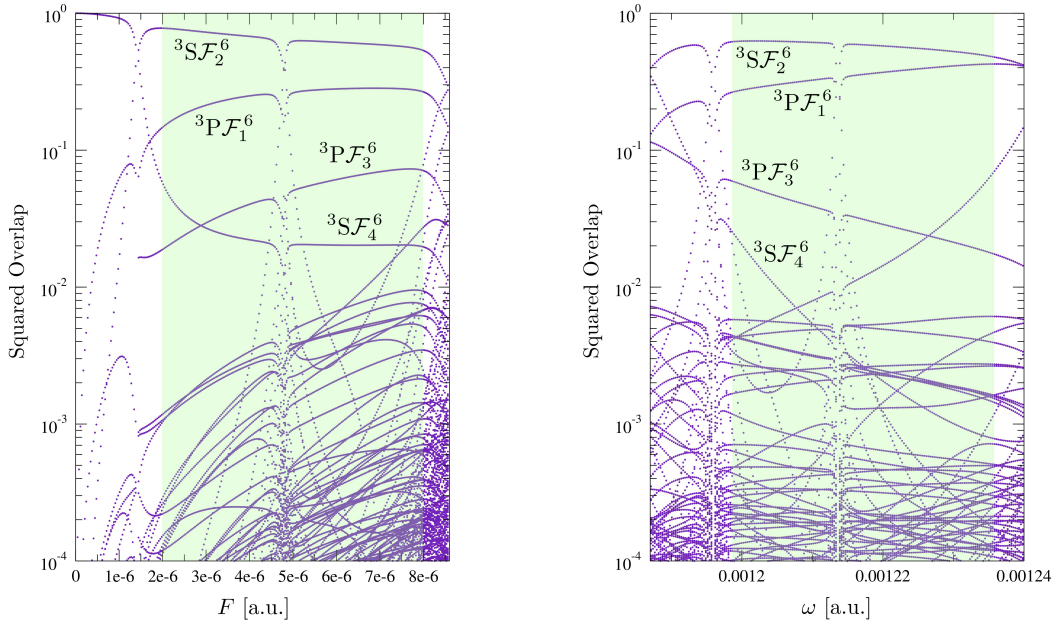


Figure 4.8.: Overlaps between the triplet wave packet $\mathcal{W}_2^6$ and the elements in the basis. The left plot shows the overlaps as a function of the field amplitude F for fixed frequency $\omega = 0.0012$ a.u., while in the right plot we present the overlaps as a function of the field frequency ω for fixed amplitude $F = 5.5 \times 10^{-6}$ a.u.. The green regions identify the field amplitude (left) and frequency (right) intervals for which the Husimi distribution of the wave packet $\mathcal{W}_2^6$ is the same displayed in Figure 4.4.

unperturbed state $^3S\mathcal{F}_2^6$. By increasing the field amplitude, the overlaps with the other elements in the basis become different from zero and in particular we observe that the principal contribution comes from the frozen planet states $^3S\mathcal{F}_2^6$, $^3P\mathcal{F}_1^6$, $^3P\mathcal{F}_3^6$ and $^3S\mathcal{F}_4^6$. The small perturbations observed for the values $F = 1.5 \times 10^{-6}$ a.u. and $F = 4.8 \times 10^{-6}$ a.u., correspond to avoided crossings between Floquet states (see Figure 4.7). The right plot displays the overlaps as a function of the field frequency ω for fixed amplitude $F = 5.5 \times 10^{-6}$ a.u.. Again, the main contribution to the wave packet is from a few S and P frozen planet states. For $\omega = 0.00124$ a.u., the contribution from the unperturbed states $^3S\mathcal{F}_2^6$ and $^3P\mathcal{F}_1^6$ is the same because this frequency correspond to the resonant value $\omega = |E(^3S\mathcal{F}_2^6) - E(^3P\mathcal{F}_1^6)|$.

To conclude this section, let us remark that we have performed our computations employing only the resonances of the subseries converging to the $N = 6$ ionization threshold. To illustrate the fact that this basis is enough to study the formation of NDWP, we repeated the computations including the resonances of $L = 0, \ldots, 8$ below the $N = 5, 6$ and 7 ionization thresholds with their respective continua and 51 Floquet blocks ($k_{\min} = -25$ and $k_{\max} = 25$) in the construction of the atomic basis (2.58). In that case, the number of basis elements was 114 319 which still remains smaller than the

	^{3}S		^{3}P	
	$-E$ [a.u.]	$\Gamma/2$ [a.u.]	$-E$ [a.u.]	$\Gamma/2$ [a.u.]
$\mathcal{G}_1^6$			0.074 452 683	0.000 000 202
$\mathcal{F}_1^6$	0.073 203 013	0.000 000 006	0.073 024 843	0.000 003 008
$\mathcal{F}_2^6$	0.071 788 666	0.000 000 007	0.071 671 979	0.000 006 616
$\mathcal{F}_3^6$	0.070 756 000	0.000 000 007		

Table 4.1.: Energies and decay rates of the atomic states needed to reproduce the dynamics of the wave packets $\mathcal{W}_2^6$, $\mathcal{W}_3^6$ and $\mathcal{W}_4^6$ presented in Section 4.2.1. The state $\mathcal{G}_1^6$ corresponds to the ground state of a series of FPS-like states.

basis of 521 795 elements used in [39]. However, with the inclusion of more states on the basis we do not observe any improvement in the convergence for the wave packets energies and decay rates, and the behaviour of Figures 4.7 and 4.8 remains the same. This was expected, since at least 22 photons are necessary to couple the frozen planet state $^3\mathrm{S}\mathcal{F}_2^6$ to states below the 5th ionization threshold and 20 photons to reach the 7th ionization threshold. This supports the fact that in our initial calculation we actually include all the relevant states and that in the dynamics of the driven frozen planet states, single ionization is the dominant decay process [39].

4.2.3 Basic ingredients in the formation of NDWP

The results in Figure 4.6 suggest that by removing from the atomic basis (2.58) the states of negligible overlap with the wave packets $\mathcal{W}_1^6$, $\mathcal{W}_2^6$ and $\mathcal{W}_3^6$, and considering only a small number of Floquet blocks, the dynamics of the driven FPS should not be affected considerably. On the other hand, if we remove from the basis one of the atomic states with greater contribution to the wave packets, we wait for an observable modification of the wave packets dynamics, i.e., in the electronic density projections in Figures 4.4 and 4.5. In such a way, we can identify the atomic states that play the fundamental role in the formation of NDWP in helium.

For this purpose, we remove progressively from the basis, the resonances of the unperturbed atom with the lowest overlap with the wave packets $\mathcal{W}_1^6$, $\mathcal{W}_2^6$ and $\mathcal{W}_3^6$, in order to keep only the minimum number of atomic states and Floquet blocks that must be plugged into the model to reproduce the dynamics showed in Figure 4.4. This procedure leaves us with the six atomic states in Table 4.1 and Floquet blocks from $k_{\min} = -1$ to $k_{\max} = 2$. In other words, if we construct the basis (2.58) only with these six states for $k_{\min} = -1$ to $k_{\max} = 2$ and solve (2.59) for the field parameters $F = 5.5 \times 10^{-6}$ a.u. and $\omega = 0.0012$ a.u., we identify Floquet eigenstates $\mathcal{W}_1^6$, $\mathcal{W}_2^6$ and $\mathcal{W}_3^6$ that exhibit the same Husimi distributions displayed in Figure 4.4.

	(a)		(b)	
m	$-E$ [a.u.]	$\Gamma/2$ [a.u.]	$-E$ [a.u.]	$\Gamma/2$ [a.u.]
1	0.073 149 52	0.000 001 24	0.073 165 98	0.000 000 03
2	0.071 743 79	0.000 002 56	0.071 748 71	0.000 001 87
3	0.070 766 20	0.000 000 58	0.070 772 79	0.000 000 38

Table 4.2.: Energies and decay rates of the triplet wave packets $\mathcal{W}_m^6$ obtained after diagonalization of Eq. (2.59) for driving field parameters $F = 5.5 \times 10^{-6}$ a.u. and $\omega = 0.0012$ a.u.. In (a) the results using the atomic basis which includes the states of Figure 4.3 with $k_{\min} = -7$, $k_{\max} = 7$. In (b) values obtained with the few level model for $k_{\min} = -1$ and $k_{\max} = 2$.

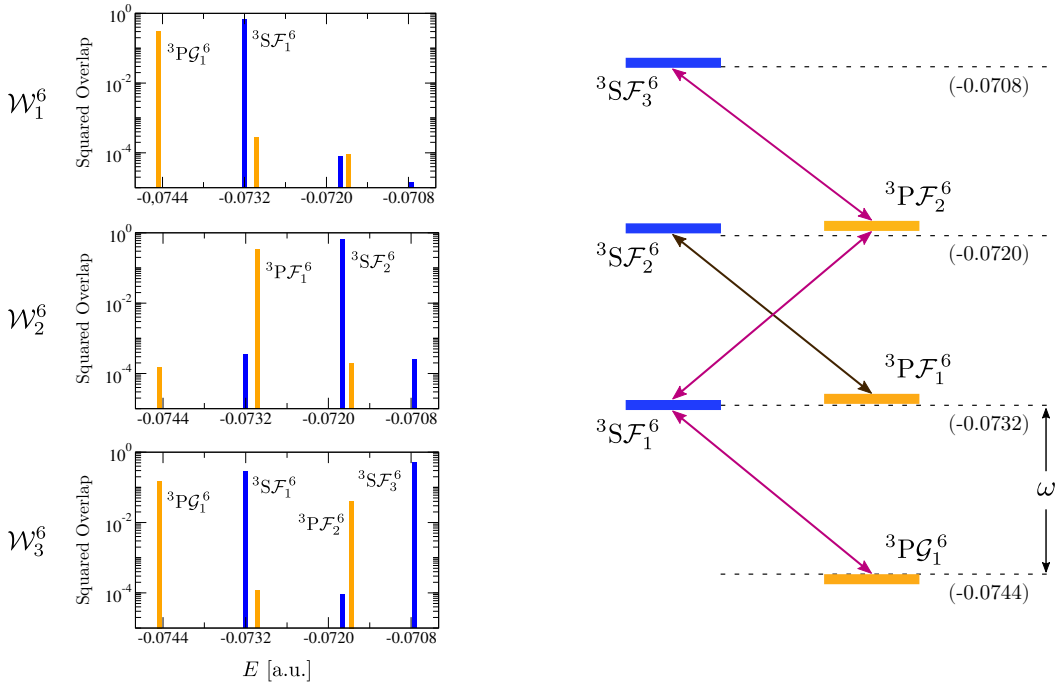


Figure 4.9.: Left plots display the overlaps between the wave packets obtained with the few level model and the atomic states in Table 4.1. In the right plot, we present the scheme of the essential states involved in the formation of the NDWP $\mathcal{W}_2^6$, $\mathcal{W}_3^6$ and $\mathcal{W}_4^6$. The dashed lines are separated by ω, with energies (in atomic units) indicated in parentheses. ^{3}S (^{3}P) states are highlighted in blue (orange).

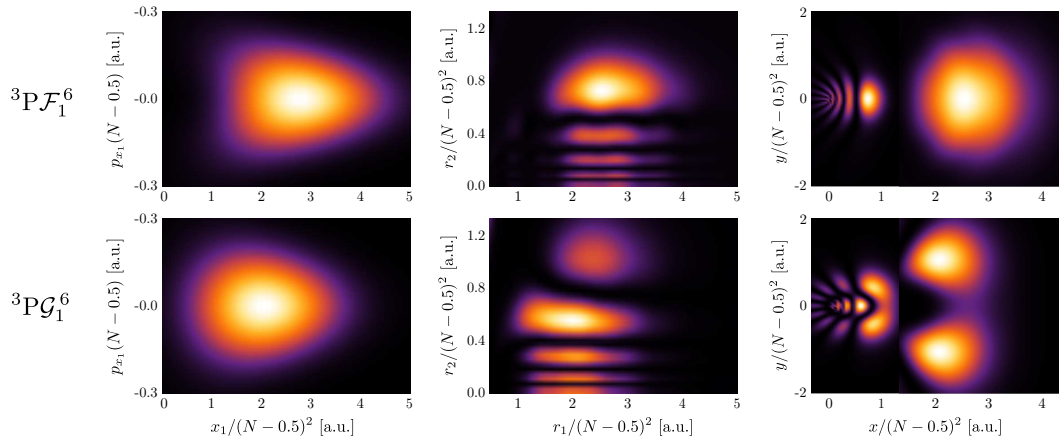


Figure 4.10.: Comparison between the unperturbed states $^3\mathrm{P}\mathcal{F}_1^6$ and $^3\mathrm{P}\mathcal{G}_1^6$. The left plots show the projections of the electronic density in phase space, while the projections of the electronic density in configuration space are depicted as function of the distances r_1 and r_2 (for $\theta_{12} = 0$) in the center plots, and for the x and y coordinates (as in Figure 3.5) in the right plots.

In Table 4.2 column (b), we present the values for the energy and decay rate for the wave packets $\mathcal{W}_1^6$, $\mathcal{W}_2^6$ and $\mathcal{W}_3^6$ obtained with the *few level model* [2]. The values for the energy obtained with the atomic basis of 4 366 elements of Section 4.2.1 and the few level model in columns (a) and (b), respectively, are the same up to the fourth decimal position. The decay rate of the wave packet $\mathcal{W}_1^6$ obtained with the few level model is two orders of magnitude smaller than the actual value in (a), while for the wave packets $\mathcal{W}_2^6$ and $\mathcal{W}_3^6$, the order of magnitude in (a) and (b) is the same. This result implies that there are resonances with non-negligible overlap with the wave packets which have significant contribution to the decay rates and have not been included in the model.

Figure 4.9 (left) shows the overlaps between the wave packets and the elements in the basis. Analizing these overlaps it is easy to identify the specific couplings that produce the nondispersive wave packets (Figure 4.9 (right)): the wave packet $\mathcal{W}_1^6$ is produced by a direct coupling between the states $^3\mathrm{S}\mathcal{F}_1^6$ and $^3\mathrm{P}\mathcal{G}_1^6$, the wave packet $\mathcal{W}_2^6$ is also produced by a direct coupling, but in this case between the frozen planet states $^3\mathrm{S}\mathcal{F}_2^6$ and $^3\mathrm{P}\mathcal{F}_1^6$, and finally, the wave packet $\mathcal{W}_3^6$ is produced by an indirect coupling between the states $^3\mathrm{S}\mathcal{F}_3^6$ and $^3\mathrm{P}\mathcal{G}_1^6$.

All the atomic states in the model are frozen planet states except the state we have denoted by $^3\mathrm{P}\mathcal{G}_1^6$. However, this state corresponds to the ground state of a series of FPS-like states that share most of the properties with the FPS (as we observe in Figure

[2] In the few level model the atomic basis (2.58) includes only the unperturbed states in Table 4.1.

4.10), but with lower expectation value of $\cos(\theta_{12})$. For instance, the value of $\langle\cos(\theta_{12})\rangle$ for the state ${}^3\mathrm{P}\mathcal{F}_1^6$ is 0.836, while for the state ${}^3\mathrm{P}\mathcal{G}_1^6$ is 0.592.

"Hyperbolic" and "elliptic" NDWP

By looking at the Husimi distributions in Figure 4.4, a question arises: why the wave packet $\mathcal{W}_2^6$ is anchored to the hyperbolic fixed point of the resonance, whereas the wave packet $\mathcal{W}_3^6$ is anchored to the elliptic fixed point of the resonance?

As we can see in Figure 4.9, the wave packet $\mathcal{W}_2^6$ is produced by the coupling between the states ${}^3\mathrm{S}\mathcal{F}_2^6$ and ${}^3\mathrm{P}\mathcal{F}_1^6$, and its largest overlap is with the state ${}^3\mathrm{S}\mathcal{F}_2^6$. However, there is a Floquet eigenstate which is also produced by the coupling between the same two atomic states, but with the largest overlap with the state ${}^3\mathrm{P}\mathcal{F}_2^6$. When we analyze their electronic density in phase space, we find that this Floquet state corresponds to a wave packet anchored to the elliptic fixed point of the resonance, as we show in Figure 4.11.

Figure 4.12 shows the energy of the two wave packets $\mathcal{W}_2^6$ (top) and the overlaps of the hyperbolic wave packet $\mathcal{W}_2^6$ with the elements in the basis[3] (bottom), as a function of the field parameters. In the left plots, the energy and overlaps are depicted against the field amplitude F for fixed frequency $\omega = 0.0012$ a.u.. For field amplitudes $F > 2 \times 10^{-6}$ a.u. (for which the contribution of the states ${}^3\mathrm{S}\mathcal{F}_2^6$ and ${}^3\mathrm{P}\mathcal{F}_1^6$ to the wave packet $\mathcal{W}_2^6$ remains nearly constant) the wave packet energies exhibit slopes of similar magnitude with opposite sign. In the right plot, where the energy and overlaps are given as a function of the frequency ω for fixed field amplitude $F = 5.5 \times 10^{-6}$ a.u., we observe that, for driving frequency $\omega < 0.00124$ a.u. (before the avoided crossing), the hyperbolic wave packet $\mathcal{W}_2^6$ has the largest overlap with the state ${}^3\mathrm{S}\mathcal{F}_2^6$, while, for frequency $\omega > 0.00124$ a.u. (after the avoided crossing), the largest overlap is with the state ${}^3\mathrm{P}\mathcal{F}_2^6$. The opposite for the elliptic wave packet.

The previous results suggest that the coupling between a FPS of $L = 0$ and a FPS of $L = 1$ produces two NDWP, one of them anchored to the hyperbolic fixed point of the resonance and the other one anchored to the elliptic fixed point of the resonance. Which one of the coupled states has the largest overlap with the wave packet depends on the driving field parameters as we observe in Figure 4.12.

4.2.4 Identification of NDWP below other ionization thresholds

In this section, we study the dynamics of the driven frozen planet states below the $N = 3, \ldots, 7$ ionization thresholds. Based on the results of the previous section, here we look for elliptic wave packets $\mathcal{W}_2^N$ produced by the direct coupling between the

[3] The overlaps of the hyperbolic and elliptic wave packets $\mathcal{W}_2^6$ with the elements in the basis are the same by exchanging the states ${}^3\mathrm{S}\mathcal{F}_2^6$ and ${}^3\mathrm{P}\mathcal{F}_1^6$.

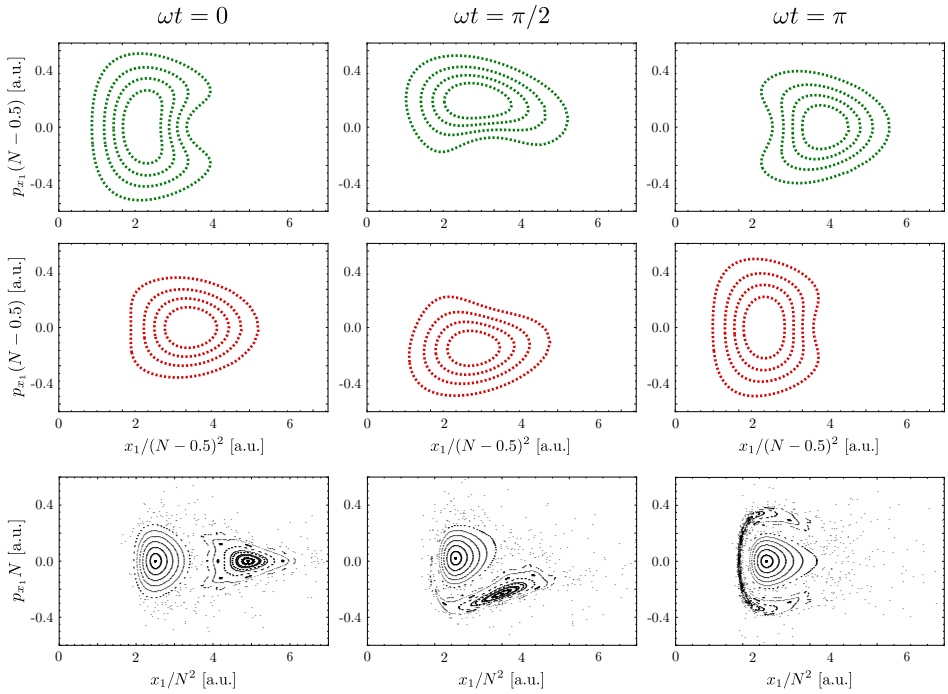


Figure 4.11.: Husimi distributions of the “hyperbolic" (green) and “elliptic" (red) wave packets $\mathcal{W}_2^6$ for electromagnetic driving at frequency $\omega = 0.0012$ a.u. and amplitude $F = 5.5 \times 10^{-6}$ a.u., depicted for different phases of the driving field.

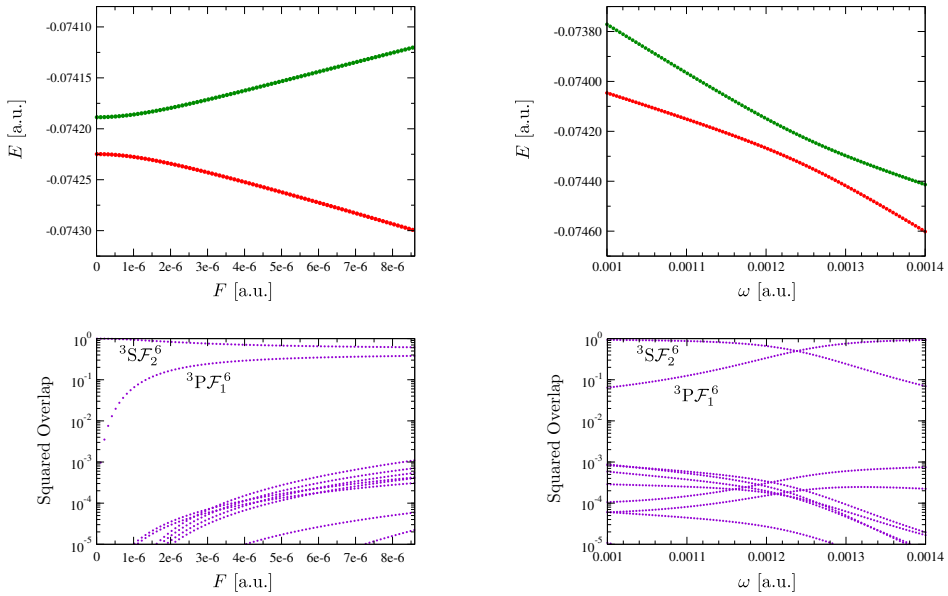


Figure 4.12.: Energy of the “hyperbolic" (green) and “elliptic" (red) wave packets $\mathcal{W}_2^6$ obtained with the few level model (top). Overlaps between the hyperbolic wave packet $\mathcal{W}_2^6$ and the elements in the atomic basis (bottom). The results are presented for variable field amplitude with fixed frequency $\omega = 0.0012$ a.u. (left) and variable field frequency with fixed amplitude $F = 5.5 \times 10^{-6}$ a.u. (right).

N	ω [a.u.]	F [a.u.]	$-E$ [a.u.]	$\Gamma/2$ [a.u.]
		Singlet states		
3	0.006 60	2.0×10^{-5}	0.329 338 5	0.000 000 5
4	0.003 60	1.0×10^{-5}	0.175 724 3	0.000 002 2
5	0.002 40	2.0×10^{-5}	0.106 898 2	0.000 004 2
6	0.001 25	1.5×10^{-6}	0.071 813 9	0.000 003 9
7	0.000 80	2.0×10^{-6}	0.051 580	0.000 002
		Triplet states		
3	0.008 50	5.0×10^{-5}	0.341 003	0.000 001
4	0.004 10	4.0×10^{-5}	0.175 471 2	0.000 002 6
5	0.002 10	1.2×10^{-5}	0.106 866 5	0.000 001 4
6	0.001 24	1.5×10^{-6}	0.071 801 4	0.000 000 9
7	0.000 80	2.0×10^{-6}	0.051 575 5	0.000 000 6

Table 4.3.: Driving field parameters and converged values for the energies and decay rates of the wave packets $\mathcal{W}_2^N$.

frozen planet states $\mathrm{S}\mathcal{F}_2^N$ and $\mathrm{P}\mathcal{F}_1^N$. In each case, we construct the atomic basis (2.58) including only the resonances converging to the ionization threshold of interest for $L = 1, \ldots, 5$ and 11 Floquet blocks ($k_{\min} = -5$ and $k_{\max} = 5$). In this basis we solve the eigenvalue problem (2.59) for driving field frequency $\omega \approx |E(\mathrm{S}\mathcal{F}_2^N) - E(\mathrm{P}\mathcal{F}_1^N)|$ and field amplitude $F < F_{\mathrm{I}}$.

In Table 4.3 we present the field parameters used in each calculation and the converged values for the energy and decay rates of the elliptic wave packets $\mathcal{W}_2^N$ identified in the Floquet spectrum. As we described in Section 4.2.2, there is an interval for the field amplitude F and frequency ω where the wave packet exhibits the nondispersive behaviour. Thus, the values in Table 4.3 should be taken as reference values, since by changing the field parameters, the wave packet energy and decay rate can also change.

Figure 4.13 shows the Hussimi distributions of the triplet wave packets for three different phases of the driving field. The Hussimi distributions for the singlet wave packets are qualitatively similar and are not presented. The wave packets are more localized by increasing N. Same behaviour was observed for NDWP in one-dimensional helium [37].

4.3 Nondispersive wave packets in 3D helium

The direct numerical treatment of the full three-dimensional helium atom driven by a laser field is computationally a very complicated task. This has made difficult the search of NDWP beyond planar helium. However, the study of driven frozen planet states in previous sections shows that nondispersive wave packets can be identified with low computational cost by the solution of the time-dependent Schrödinger equation

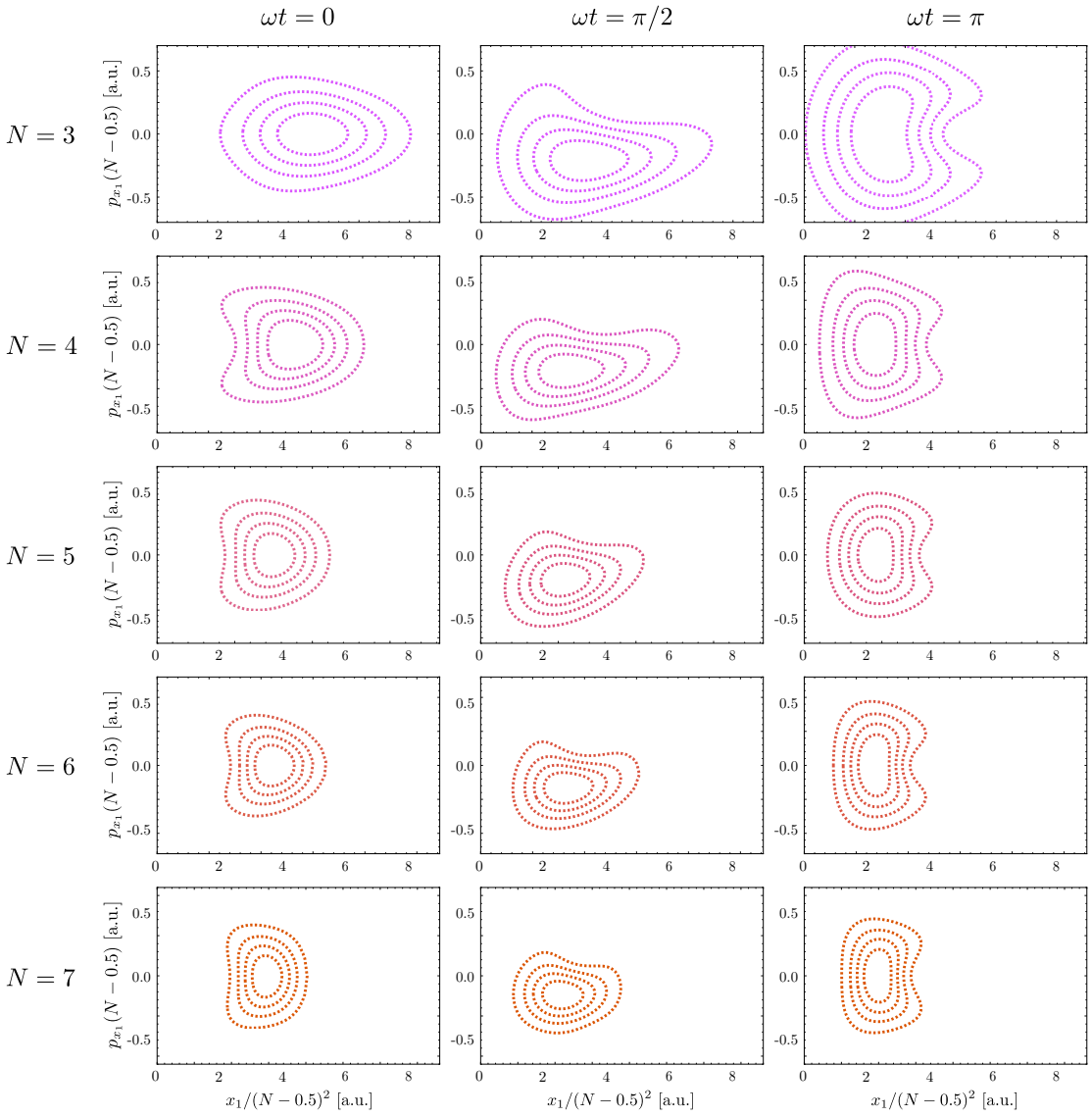


Figure 4.13.: Contour plot of the Husimi distribution of the triplet elliptic wave packets $\mathcal{W}_2^N$, obtained by diagonalization of Eq. (2.59) for the field parameters in Table 4.3, at different phases of the driving field.

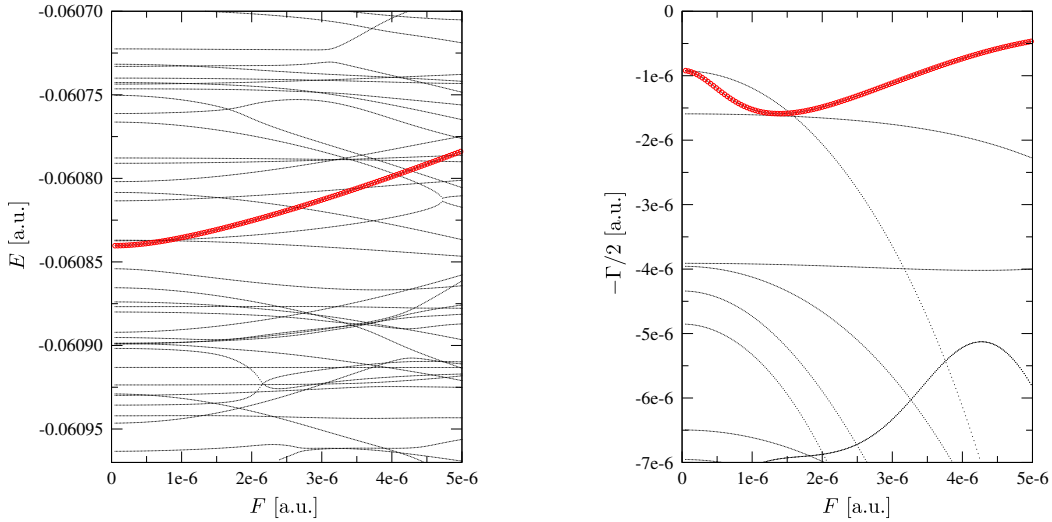


Figure 4.14.: Evolution of the energies E (left) and decay rates Γ (right) as a function of the field amplitude F, for driving frequency $\omega = 0.0008$ a.u.. Red circles identify the wave packet $\mathcal{W}_2^6$.

in the atomic basis, i.e., the basis in which the unperturbed Hamiltonian is diagonal. This approach allowed us to characterize NDWP in planar helium, identifying the key ingredients in the formation of this kind of states. Concretely, we found that the quasi-resonant coupling between frozen planet states of angular momentum $L = 0$ and $L = 1$ could produce nondispersive wave packets.

Here, the idea is to study driven frozen planet states in three-dimensional helium using the same approach of Section 4.2.1. With this in mind, we solve the unperturbed Hamiltonian (2.2) looking for singlet states of angular momentum $L = 0, \ldots, 5$ in the energy region below the $N = 6$ ionization threshold. Those states are used in the construction of the atomic basis (2.58) including 13 Floquet blocks ($k_{\min} = -6$ and $k_{\max} = 6$). Then, we solve the eigenvalue problem (2.59) for field parameters $F < F_{\mathrm{I}} = 0.03N^{-4}$ and $\omega \approx \omega_{\mathrm{I}} = 0.3N^{-3}$ for $N = 6$.

Figure 4.14 shows the real (left) and imaginary parts (right) of the Floquet spectrum as a function of the field amplitudes for fixed frequency $\omega = 0.0008$ a.u.. Red circles identify the Floquet state $\mathcal{W}_2^6$ which has the greatest overlap with the unperturbed frozen planet state ${}^1\mathrm{S}\mathcal{F}_2^6$.

In Figure 4.15 we present the Husimi distribution of the singlet state $\mathcal{W}_2^6$ obtained for driving field parameters $F = 3.9 \times 10^{-6}$ a.u. and $\omega = 0.00088$ a.u.. For comparison we also show the classical configuration for the same field parameters. The above state

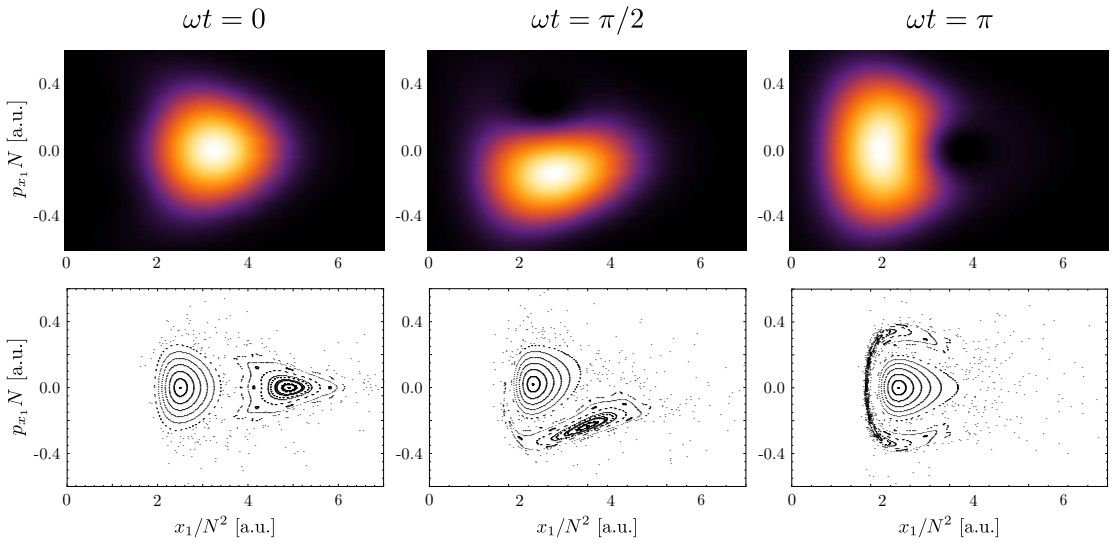


Figure 4.15.: Husimi distribution of the elliptic wave packet $\mathcal{W}_2^6$ obtained for field parameters $F = 3.9 \times 10^{-6}$ a.u. and $\omega = 0.00088$ a.u., for different phases of the driving field (top). Classical configuration for the same field parameters (bottom).

corresponds to a wave packet associated with the elliptic fixed point of the 1:1 resonance.

Figure 4.16 displays the overlaps between the wave packet $\mathcal{W}_2^6$ and the elements in the basis as a function of the field amplitude (left) and frequency (right). Green regions identify the intervals for the field parameters where the Floquet state $\mathcal{W}_2^6$ exhibit the nondispersive behaviour of Figure 4.15. At field amplitude $F = 3.9 \times 10^{-6}$ a.u. and frequency $\omega > 0.000894$ a.u. this wave packet has the greatest overlap with the state ${}^1\mathrm{S}\mathcal{F}_2^6$, but for frequency $\omega < 0.000894$ a.u. the greatest overlap is with the state ${}^1\mathrm{P}\mathcal{F}_1^6$. In both plots, we observe that the main contribution to the wave packet is given by the frozen planet states ${}^1\mathrm{S}\mathcal{F}_2^6$ and ${}^1\mathrm{P}\mathcal{F}_1^6$, in agreement with the results of Section 4.2.3 for planar helium.

4.3.1 Some comments on the experimental identification of NDWP

As we mentioned before, there are only non-conclusive experimental evidence of the existence of FPS [114–116]. Previous results on planar helium [124, 125], show that the frozen planet states are not detected in the photoionization cross section from the ground state of the atom. However, they are rather strongly coupled to some excited bound states. These observations open a door in the direction of preparation of the so

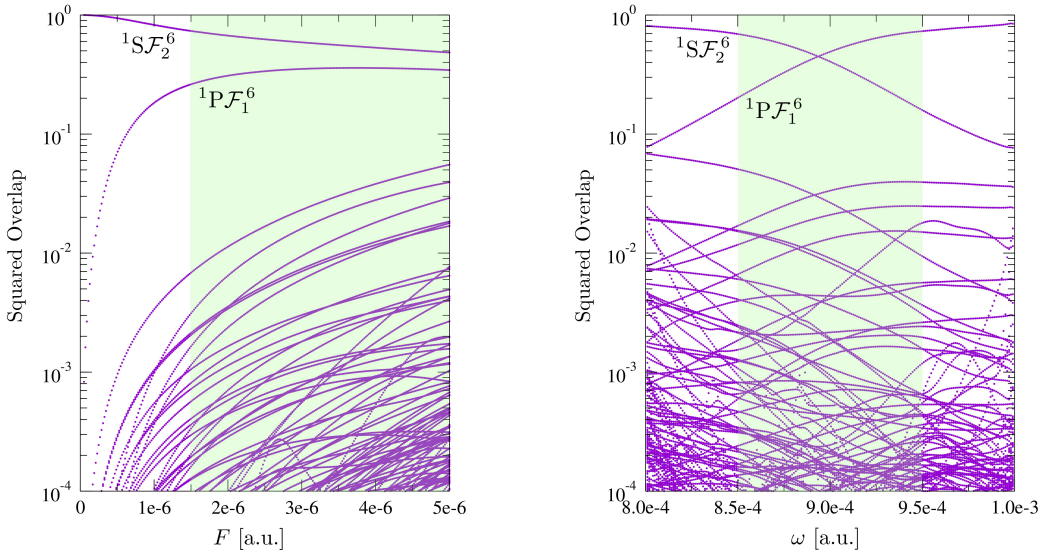


Figure 4.16.: Overlaps between the elliptic wave packet $\mathcal{W}_2^6$ and the elements in the basis, as a function of the field amplitude F for fixed frequency $\omega = 0.00088$ a.u. (left), and as a function of the field frequency ω for fixed amplitude $F = 3.9 \times 10^{-6}$ a.u. (right).

far unobserved frozen planets states using a two-photon transition from the ground state mediated by single or doubly excited states.

Figure 4.17 shows two possible schemes to populate the frozen planet state $^1S\mathcal{F}_2^6$ by a two-photon process followed by the near resonant coupling with the state $^1P\mathcal{F}_1^6$ to produce a NDWP. The frequencies required for the electronic transitions to obtain the FPS can be estimated, being in the far ultraviolet region. Although for this energy range different types of lasers can be found, the spectroscopic precision has not been achieved yet.

Finally, in Figure 4.14 we have seen that the energy of the state $\mathcal{W}_2^6$ present a pronounced shift at positive slope. This behaviour was also observed in the planar case in Figure 4.7, and is associated to a large dipole moment of the electronic density in configuration space. Figure 4.18 shows the expectation value of the electronic dipole $\langle x_1 + x_2 \rangle$ for the Floquet states obtained after diagonalization of Eq. (2.59) for field parameters $F = 3.9 \times 10^{-6}$ a.u. and $\omega = 0.00088$ a.u.. The expectation value of the electronic dipole for the wave packet $\mathcal{W}_2^6$ (indicated by the red line) which has the largest value in this energy region could be a useful quantity for the experimental identification of this state.

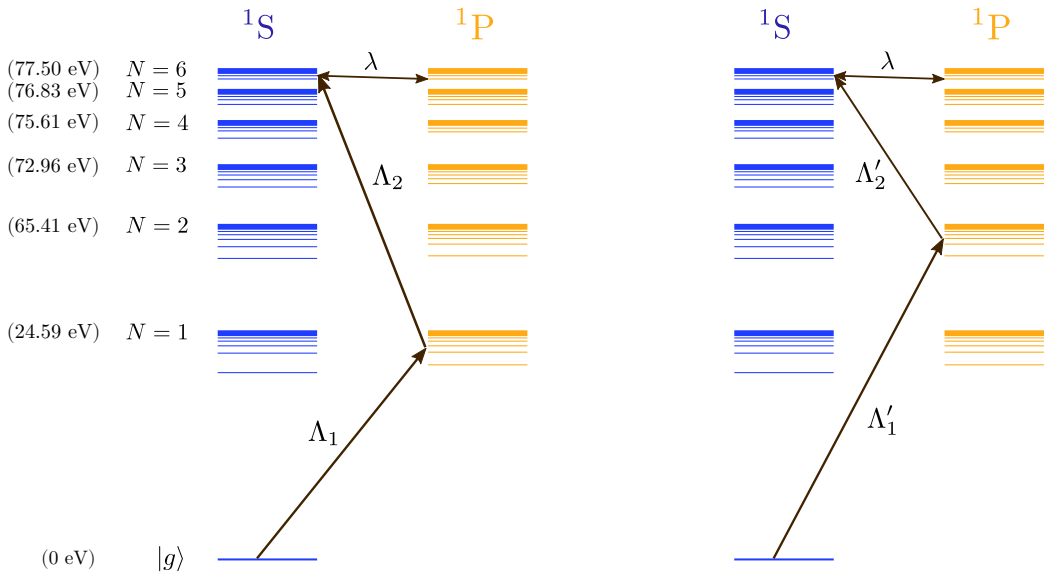


Figure 4.17.: Two-photon transition scheme from the ground state to the frozen planet state $^1\mathrm{S}\mathcal{F}_2^6$ with energy $E = -0.06084080$ a.u. (77.355 eV) mediated by a single excited state (left) and a doubly excited state (right). The wavelengths involved in the transitions are: $50.4\,\mathrm{nm} \leq \Lambda_1 \leq 58.4\,\mathrm{nm}$, $22.1\,\mathrm{nm} \leq \Lambda_2 \leq 23.5\,\mathrm{nm}$, $19.0\,\mathrm{nm} \leq \Lambda'_1 \leq 19.3\,\mathrm{nm}$ and $93.7\,\mathrm{nm} \leq \Lambda'_2 \leq 103.8\,\mathrm{nm}$. After population of the FPS $^1\mathrm{S}\mathcal{F}_2^6$, the near resonant coupling with the state $^1\mathrm{P}\mathcal{F}_1^6$ is produced at $\lambda = 51776.5\,\mathrm{nm}$.

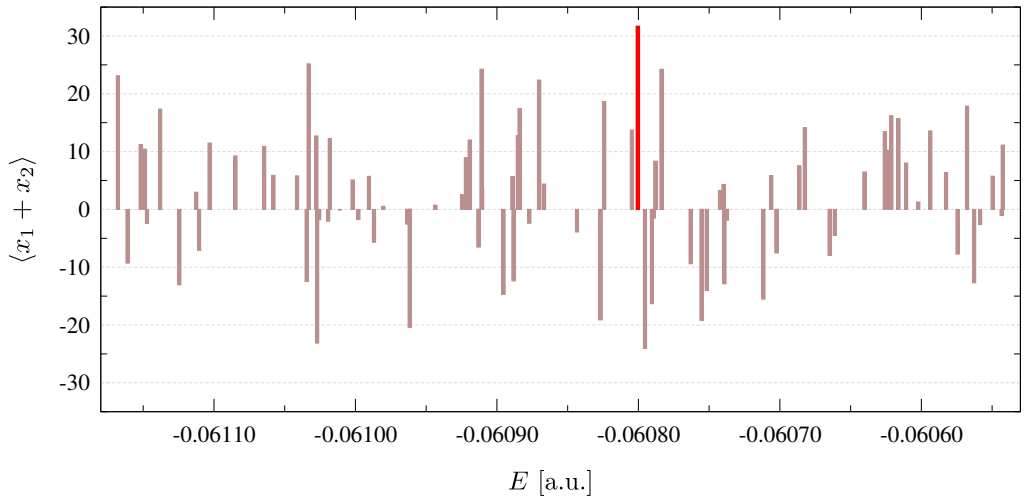


Figure 4.18.: Expectation value of the electronic dipole along the x direction for the Floquet states obtained after diagonalization of Eq. (2.59) for field amplitude $F = 3.9 \times 10^{-6}$ a.u. (intensity 1.4×10^{11} W cm^{-2}) and frequency $\omega = 0.00088$ a.u. ($\lambda = 51776.5$ nm). Red line indicates the value for the elliptic wave packet $\mathcal{W}_2^6$ with energy $E = -0.060800$ a.u. (77.357 eV).

5 Quantum entanglement in planar helium

Entanglement is one of the most significant characteristics in the quantum mechanical description of multipartite systems [96] and represents a key ingredient in quantum information theory [**?**]. In this sense, it is of great interest to investigate the entanglement properties of atomic systems and the controlled manipulation of entangled states for possible applications in quantum information processes [**?**, **?**]. Previous studies have considered entanglement properties of bound levels of artificial model systems [126–131] and for the case of two-electron atoms, the investigations have focused on ground states and singly excited states [129, 132–134]. More recently, entanglement measures have been calculated for doubly excited states below the second ionization threshold in helium [135, 136].

In this chapter, we present entanglement measures for bound and doubly excited singlet states below the second, third and fourth ionization thresholds for planar helium. We also compute the entanglement of nondispersive wave packets produced by the near-resonant coupling between two frozen planet states. For that purpose we use the methods described in Section 2.5.

5.1 Entanglement in bound and doubly excited states

We calculate the amount of entanglement for the lowest bound and doubly excited $^1\mathrm{S}$ and $^1\mathrm{P}$ states below the $N = 2, 3$ and 4 ionization thresholds.

As mentioned in Section 2.5, the integral appearing in the entanglement measure (2.68) is evaluated using Monte Carlo numerical integration. As we observe in Figure 5.1, the region of integration increases with the excitation of the outer electron which makes the computations very time consuming for highly excited states since the number of integrand evaluations needs to be increased to reach the desired accuracy. For instance, to calculate the entanglement measure for the ground and third single excited states we use $5\,000\,000$ (two hours of computation) and $200\,000\,000$ (two days of computation) integrand evaluations, respectively[1].

[1] Calculations have been carried out on a Workstation DELL PRECISION T610 (64GB RAM, 20 processors Intel(R) Xeon(R) at 2.5GHz).

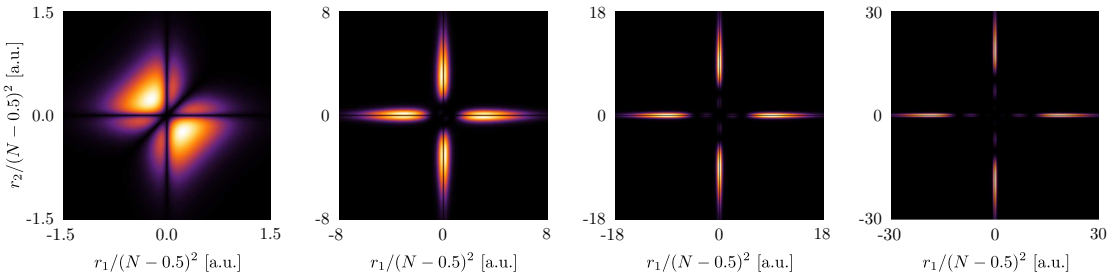


Figure 5.1.: From left to right, probability density of the ground and lowest three singly excited ^{1}S states. The integration volume to compute the entanglement measures increases with increasing excitation of the outer electron.

	^{1}S		^{1}P	
N, n	$-E$ [a.u.]	$\mathcal{E}$	$-E$ [a.u.]	$\mathcal{E}$
1, 1	11.899 822 343	0.010 8		
1, 2	8.250 463 875	0.696 7	8.211 542 09	0.999 99
1, 3	8.085 842 793	0.750 1	8.077 637 33	0.958 80
1, 4	8.042 911 011	0.751 0	8.039 947 88	0.751 43
1, 5	8.025 668 310	0.752 4	8.024 280 94	0.752 6

Table 5.1.: Energies and entanglement of the lowest bound ^{1}S and ^{1}P states of planar helium.

In table 5.1, we present the amount of entanglement for the lowest bound ^{1}S and ^{1}P states of planar helium, evaluated using the measure (2.68).

Figure 5.2 displays the amount of entanglement as a function of energy for bound ^{1}S (left plot) and ^{1}P (right plot) states. In the left plot, we observe that the ground state exhibit the minimum entanglement value and the tendency of the amount of entanglement of singly excited states is to increase with energy. The opposite situation is found for bound ^{1}P states in the right plot, where the entanglement decrease with energy. These results are consistent with the entanglement behaviour observed in previous works in three-dimensional helium for low lying excited states [132, 135].

Now, we want to study the entanglement properties of doubly excited states (DES) below the $N = 2, 3$ and 4 ionization thresholds. In Tables 5.2 and 5.3 we present the amount of entanglement for doubly excited ^{1}S and ^{1}P states, respectively. Additionally we include the expectation value of $\cos\theta_{12}$ and we identify the lowest FPS of the series converging to the third and fourth ionization thresholds.

In the case of DES, it can be observed that the amount of entanglement have different behaviour according to their value of $\langle\cos\theta_{12}\rangle$. In Fig 5.3 (top panels) we present the amount of entanglement as a function of the energy for doubly excited ^{1}S states. The results are organized in series that can be related to the value of $\langle\cos\theta_{12}\rangle$ as we observe

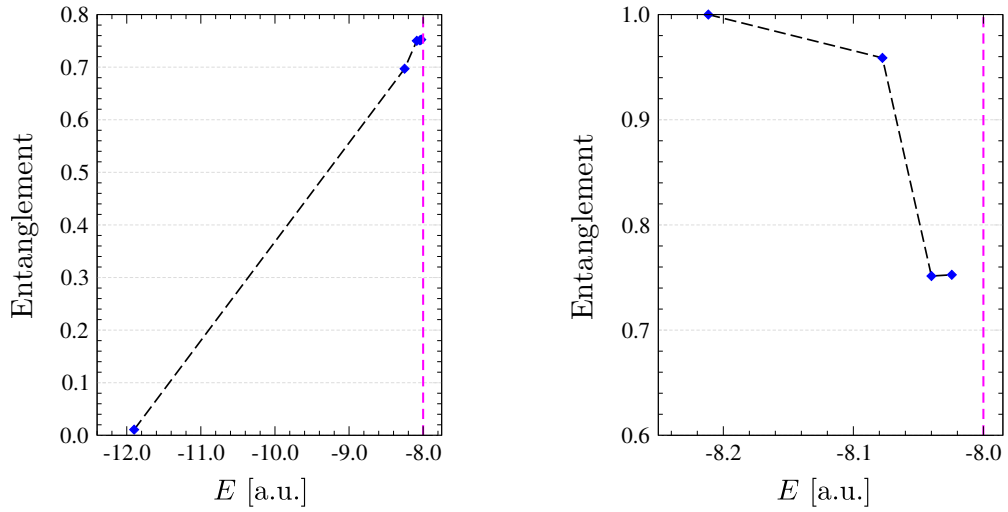


Figure 5.2.: Entanglement against energy for helium ground and singly excited ^{1}S (left) and ^{1}P (right) states. Dashed vertical lines indicate the position of the $N = 1$ single ionization threshold.

in the bottom panels of Fig 5.3, where we show the expectation values of $\cos\theta_{12}$ as a function of the energy. Similar behaviour is presented for doubly excited ^{1}P states in Figure 5.4.

In our results for DES below the $N = 2$ ionization threshold, the amount of entanglement in the different series increases to reach a maximum value and then decreases, with exception of the ^{1}P states with $\langle\cos\theta_{12}\rangle \approx 0.5$. This tendency is also exhibited by reported results in three-dimensional helium [135]. For DES below the $N = 3$ ionization threshold in Figs. 5.3 and 5.4 (center), the maximum entanglement values correspond to FPS (marked with blue squares), while the minimum values correspond to the states associated with the classical eZe configuration (marked with red circles). In the case of DES below the $N = 4$ ionization threshold, Figs. 5.3 and 5.4 (right), the FPS (blue squares) does not have the maximum entanglement values, however, their values are above 0.92, which is still large compared with other series of states and confirms the high degree of correlations in FPS.

By considering only the results for frozen planet states we observed that: below each ionization threshold, entanglement values for ^{1}P states are greater than for ^{1}S states, and the amount of entanglement increases with N.

As mentioned in Section 3.2, symmetric and antisymmetric highly doubly excited states a decomposition into series can be identified for the values of $\langle\cos\theta_{12}\rangle$. Thus, the above results suggest that the entanglement values could be used to classify this kind of highly

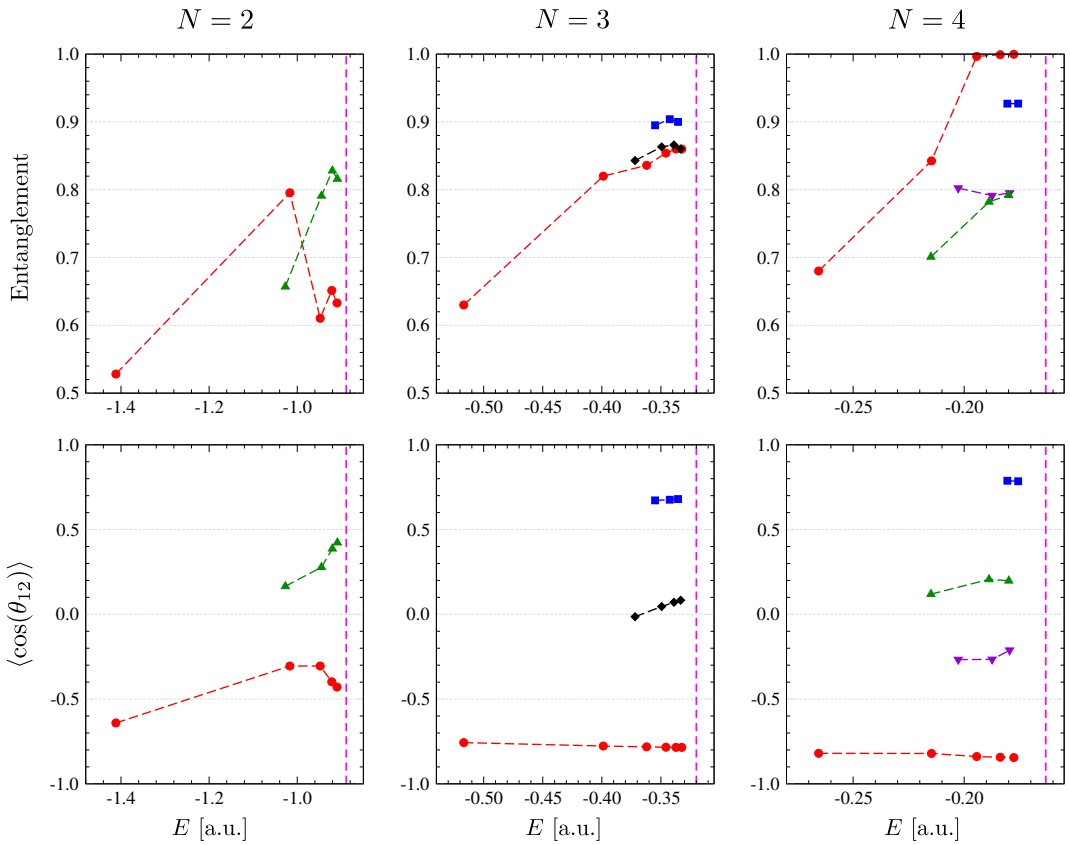


Figure 5.3.: Entanglement (top) and $\langle\cos\theta_{12}\rangle$ (bottom) against energy for the lowest ^{1}S doubly excited states below the Nth single ionization threshold (indicated by vertical dashed lines). The results are organized according to the values of $\langle\cos\theta_{12}\rangle$.

doubly excited states. However, this assumption needs to be verified with entanglement calculations for higher excitations in planar and three-dimensional helium.

5.2 Quantum entanglement in NDWP

In this section, we study the amount of entanglement of driven frozen planet states below the third and fourth ionization thresholds. To solve the time-dependent Schrödinger equation we follow the approach of Section 2.4.2. We include in the atomic basis (2.58) only the frozen planet states $^1\mathrm{S}\mathcal{F}_2^N$ and $^1\mathrm{P}\mathcal{F}_1^N$ and two Floquet blocks ($k_{\min} = -1$ and $k_{\max} = 0$).

In the Floquet spectrum obtained by solving the eigenvalue problem (2.59), we identify the elliptic wave packet $\mathcal{W}_2^N$ which has the greatest overlap with the unperturbed state $^1\mathrm{S}\mathcal{F}_2^N$. For $N = 3$ we use the field parameters $F = 4 \times 10^{-5}$ a.u. and $\omega = 0.0066$ a.u.. The wave packet $\mathcal{W}_2^3$ has energy $E = -0.3426101$ a.u. and decay rate $\Gamma = 8 \times 10^{-7}$ a.u.

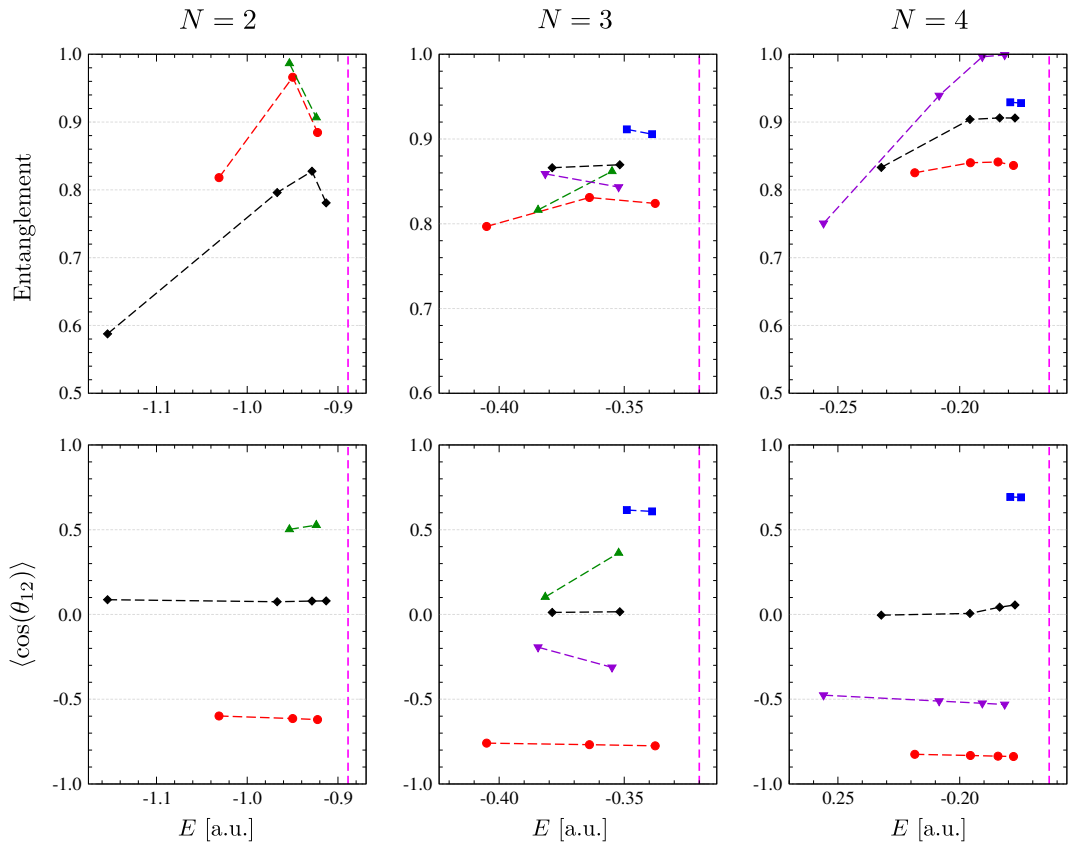


Figure 5.4.: Entanglement (top) and $\langle\cos\theta_{12}\rangle$ (bottom) against energy for the lowest ^{1}P doubly excited states below the Nth single ionization threshold (indicated by vertical dashed lines). The results are organized according to their value of $\langle\cos\theta_{12}\rangle$.

		$-E$ [a.u.]	$\Gamma/2$ [a.u.]	$\langle\cos\theta_{12}\rangle$	$\mathcal{E}$
$N=2$		1.411 496 33	0.001 241 73	−0.641	0.528 1
		1.027 047 55	0.000 251 80	0.165	0.657 0
		1.016 821 16	0.000 106 49	−0.305	0.795 5
		0.947 988 02	0.000 103 36	−0.305	0.610 4
		0.945 091 77	0.000 003 69	0.278	0.791 0
		0.921 743 53	0.000 044 79	−0.398	0.651 4
		0.920 365 12	0.000 000 49	0.387	0.828 1
		0.909 741 13	0.000 022 96	−0.429	0.633
		0.908 994 46	0.000 000 12	0.423	0.816
$N=3$		0.516 872 10	0.001 165 79	−0.757	0.625
		0.398 739 59	0.000 524 76	−0.777	0.819
		0.371 886 03	0.000 684 06	−0.014	0.843 0
		0.362 061 79	0.000 219 92	−0.782	0.836
	$\mathcal{F}_1^3$	0.354 907 55	0.000 003 37	0.672	0.895 0
		0.349 336 28	0.000 311 35	0.046	0.863 2
		0.345 721 87	0.000 106 60	−0.784	0.854
	$\mathcal{F}_2^3$	0.342 496 48	0.000 000 48	0.676	0.904
		0.338 947 12	0.000 166 03	0.071	0.866
		0.337 233 25	0.000 058 60	−0.785	0.865
	$\mathcal{F}_3^3$	0.335 495 10	0.000 000 07	0.680	0.897
		0.333 257 83	0.000 098 48	0.083	0.864
		0.332 312 68	0.000 035 37	−0.785	0.859
$N=4$		0.265 531 28	0.000 774 57	−0.820	0.680 1
		0.214 973 81	0.000 509 11	0.119	0.700 96
		0.214 716 02	0.000 436 21	−0.821	0.842 5
		0.202 676 79	0.001 395 54	−0.267	0.802 3
		0.194 378 58	0.000 222 19	−0.839	0.996 541
		0.188 805 39	0.000 108 16	0.206	0.782 13
		0.187 411 99	0.000 791 48	−0.266	0.791 3
		0.183 759 94	0.000 116 31	−0.843	0.999 083
	$\mathcal{F}_1^4$	0.180 560 51	0.000 000 88	0.788	0.926 9
		0.179 914 71	0.000 034 17	0.198	0.792
		0.179 550 43	0.000 480 43	−0.212	0.795
		0.177 663 08	0.000 065 86	−0.845	0.999 736
	$\mathcal{F}_2^4$	0.175 705 10	0.000 001 48	0.785	0.927

Table 5.2.: Energies and entanglement of the lowest ^{1}S doubly excited states below the Nth single ionization threshold. Decay rates and the expectation value of $\cos\theta_{12}$ are also shown.

	N	$-E$ [a.u.]	$\Gamma/2$ [a.u.]	$\langle\cos\theta_{12}\rangle$	$\mathcal{E}$
$N=2$		1, 153 941 04	0.000 128 21	0.087	0.587 60
		1, 031 093 30	0.000 000 11	−0.599	0.818 05
		0.966 997 08	0.000 019 51	0.075	0.796 0
		0.953 526 23	0.000 000 03	0.502	0.986 61
		0.949 895 59	0.000 000 03	−0.614	0.966 12
		0.928 609 96	0.000 007 46	0.079	0.827 5
		0.923 888 21	0.000 000 01	0.527	0.906 7
		0.922 496 28	0.000 000 01	−0.620	0.884 6
		0.912 996 73	0.000 003 61	0.080	0.780 8
$N=3$		0.405 019 34	0.000 007 35	−0.759	0.796 8
		0.384 454 91	0.002 026 90	−0.193	0.816 3
		0.381 575 84	0.000 334 31	0.103	0.858 9
		0.378 800 09	0.000 008 63	0.012	0.866 1
		0.363 904 50	0.000 004 31	−0.768	0.831 0
		0.354 875 71	0.000 955 57	−0.312	0.861 9
		0.352 224 93	0.000 051 40	0.363	0.843 3
		0.351 767 14	0.000 001 53	0.016	0.869 6
	$\mathcal{F}_1^3$	0.348 950 78	0.000 000 09	0.616	0.911 4
	$\mathcal{F}_2^3$	0.338 858 83	0.000 000 05	0.608	0.905 7
		0.337 615 38	0.000 001 42	−0.775	0.824
$N=4$		0.255 897 52	0.001 860 37	−0.476	0.750 6
		0.232 202 03	0.001 559 25	−0.004	0.833 1
		0.218 440 49	0.000 014 26	−0.825	0.825 2
		0.208 447 47	0.001 062 86	−0.511	0.939 1
		0.195 795 98	0.000 711 42	0.006	0.903 9
		0.195 593 04	0.000 010 61	−0.832	0.840 0
		0.190 708 33	0.000 553 64	−0.524	0.996 26
		0.184 272 34	0.000 006 82	−0.836	0.841 1
		0.183 600 48	0.000 394 56	0.043	0.906 1
		0.181 531 26	0.000 298 62	−0.531	0.998 99
	$\mathcal{F}_1^4$	0.179 248 59	0.000 001 53	0.693	0.929 2
		0.177 914 28	0.000 004 41	−0.838	0.836
		0.177 295 39	0.000 239 32	0.056	0.906
	$\mathcal{F}_2^4$	0.174 807 89	0.000 001 01	0.691	0.928

Table 5.3.: Energies and entanglement of the lowest ^{1}P doubly excited states below the Nth single ionization threshold. Decay rates and the expectation value of $\cos\theta_{12}$ are also shown.

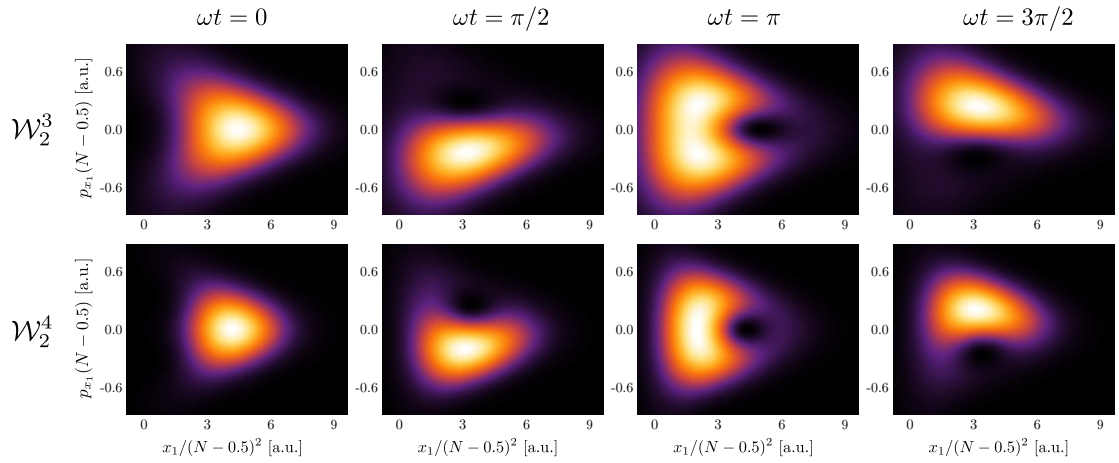


Figure 5.5.: Husimi distribution of the wave packets $\mathcal{W}_2^3$ (top) and $\mathcal{W}_2^4$ (bottom) for different phases of the driving field.

For the case of $N = 4$ the field parameters are $F = 2 \times 10^{-5}$ a.u. and $\omega = 0.0036$ a.u., and the energy and decay rate wave of the packet $\mathcal{W}_2^4$ are $E = -0.1757698$ a.u. and $\Gamma = 4.5 \times 10^{-6}$ a.u., respectively. Figure 5.5 displays the Husimi distribution of wave packets $\mathcal{W}_2^3$ and $\mathcal{W}_2^4$ for different phases of the driving field.

In Figure 5.6 we show the amount of entanglement for the two wave packets calculated as a function of the driving field phase. For comparison, we also show the amount of entanglement for the FPS involved in the formation of the wave packets and the time-average entanglement $\bar{\mathcal{E}}$ over one period defined by

$$\bar{\mathcal{E}} = \frac{1}{T} \int_0^T dt\, \mathcal{E}(t)\,, \tag{5.1}$$

where $\mathcal{E}(t)$ is given by (2.68), and $T = 2\pi/\omega$ is the field period.

For the wave packet $\mathcal{W}_2^3$, the time-average entanglement $\bar{\mathcal{E}}$ presented in Figure 5.6 (top) is approximately the mean value between the amount of entanglement of the frozen planet states ${}^1\mathrm{S}\mathcal{F}_2^3$ and ${}^1\mathrm{P}\mathcal{F}_1^3$ (see Tables 5.2 and 5.3). More interesting is the case of the wave packet $\mathcal{W}_2^4$ displayed in Figure 5.6 (bottom) This wave packet exhibit a time-average entanglement which is greater than the entanglement values of the two unperturbed frozen planet states involved in its formation. This enhancement of entanglement produced by the driving field was also identified in a more simple system of two qubits under periodic driving [137], however, in our case it is necessary to verify these results on wave packets below other ionization thresholds and also in the three-dimensional system.

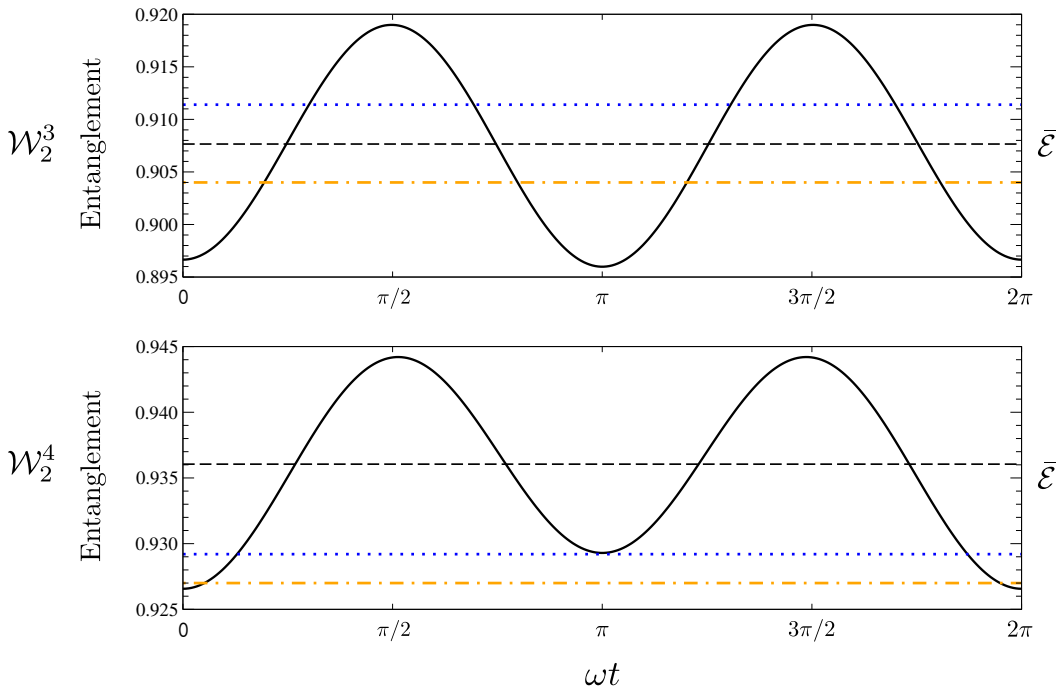


Figure 5.6.: Entanglement of the wave packets $\mathcal{W}_2^3$ (top) and $\mathcal{W}_2^4$ (bottom) as a function of the driving field phase ωt (solid curves). Dotted-dashed and dotted lines correspond to the entanglement measures of the ${}^1\mathrm{S}\mathcal{F}_2^N$ and ${}^1\mathrm{P}\mathcal{F}_1^N$ FPS, respectively. Dashed lines indicate the time-average $\bar{\mathcal{E}}$. In both cases, $N = 3$ and $N = 4$, the maximum values for the wave packet entanglement are exhibited for the driving field phases $\omega t = \pi/2$ and $\omega t = 3\pi/2$.

Summary and outlook

6

6.1 Summary

In the present thesis, we have studied the dynamics of driven doubly excited states of planar and three-dimensional helium, and the formation of two-electron nondispersive wave packets.

In Chapter 2, we introduced the theoretical and numerical framework for the description of the unperturbed and driven helium atom. Our planar approach presented in Section 2.2, is based on the *ab initio* method developed in [38, 39] which gives an accurate description of the system combining complex dilation, and the representation of the Hamiltonian in suitably chosen coordinates without adjustable parameters. The method for the treatment of three-dimensional helium (given in Section 2.3), uses an expansion of the two-electron wave function in a configuration interaction basis [25, 70, 71] where the radial one electron functions are Coulomb-Sturmian functions with different nonlinear parameters for the description of each electron. For the description of the helium atom under the action of a periodic driving, we introduced a numerical treatment which combines an spectral method with Floquet theory. The method, presented in Section 2.4, is based on the solution of the time-dependent Schrödinger equation in a basis set composed of eigenstates of the unperturbed Hamiltonian.

In Chapter 3, we discussed the basic properties of the classical frozen planet configuration, followed by the identification of frozen planet states of planar and three-dimensional helium for singlet and triplet symmetry with total angular momentum $L = 0$ and $L = 1$, in the energy regime up to the 7th ionization threshold.

Starting with a general description of the driven frozen planet configuration, our approach to solve the TDSE has been applied in Chapter 4 to the investigation of DES of helium under periodic driving. With this method, we have achieved a significant reduction of the size of the matrices involved in the computations. This allowed us in Section 4.2, to characterize nondispersive wave packets in planar helium. We identified singlet and triplet NDWP below the the $N = 3, \ldots, 7$ ionization thresholds. In particular we performed a detailed study of triplet NDWP below the 6th ionization threshold. We calculated their energies and decay rates as a function of the driving field parameters and we analyzed their overlaps with the elements of the basis. The results obtained showed that the main contribution to the wave packets is given by a small number of

atomic states of low angular momentum. Indeed, we have been able to reduce the system to its very basic ingredients, finding that the coupling between a FPS of $L = 0$ and a FPS of $L = 1$ produces two NDWP, one of them anchored to the hyperbolic fixed point of the 1:1 resonance island in the phase space of the classical driven frozen planet configuration and the other one anchored to the elliptic fixed point of the resonance. In Section 4.3, Our approach has then successfully been applied to the investigation of three-dimensional helium under periodic driving in the energy region below the 6th ionization threshold, and we give for first time theoretical evidence of the existence of nondispersive wave packets in three-dimensional helium. We also presented a brief discussion about their experimental identification.

Finally, in Chapter 5, we calculated entanglement measures for $^1\mathrm{S}$ and $^1\mathrm{P}$ bound and doubly excited states below the second, third and fourth ionization thresholds for planar helium. We also computed the entanglement of nondispersive wave packets below the third and fourth ionization thresholds, produced by the near-resonant coupling between two frozen planet states. The wave packet below the fourth ionization threshold exhibited a time-average entanglement greater than the entanglement values of the two unperturbed frozen planet states involved in its formation.

6.2 Outlook

One of the main results of this thesis is our efficient treatment of multiphoton processes achieved with a spectral method combined with Floquet theory. With the implementation of advanced time propagation methods [138–140], our approach should be suitable for the investigation of the atom-light interaction and the controlled electronic dynamics not only with time-periodic external fields but also with laser pulses.

In this work we have identified nondispersive wave packets in three-dimensional helium, however, a complete characterization of these objects including their entanglement properties is required within the three-dimensional model.

Appendix

A

A.1 Lanczos algorithm

In this thesis, we are interested in the calculation of specific eigenstates of a generalized eigenvalue problem. The dimensions of the matrices involved in our computations are typically large. However, for the purpose of this work, we only need to acces a given energy region of the He spectrum. In this sense, the Lanczos algorithm represents an appropriate tool for our requirements.

The Lanczos method is a very powerful fast convergence tool for extracting few extremal eigenvalues and eigenvectors of a large symmetric matrix [141, 142]. This method was later adapted for generalized symmetric eigenvalue problems $\mathbf{A}\mathbf{x} = \varepsilon\mathbf{B}\mathbf{x}$ [143]. By multiplication from the left by $\mathbf{A}^{-1}$, the GEVP is equivalent to the eigenvalue problem

$$\tilde{\mathbf{A}}\mathbf{x} = \mu\mathbf{x}\,, \tag{A.1}$$

where $\tilde{\mathbf{A}} = \mathbf{A}^{-1}\mathbf{B}$ and $\mu = 1/\varepsilon$. The Lanczos method gives good approximations mainly for the largest eigenvalues μ_i (i.e., $\varepsilon_i \simeq 0$). Hence, by shifting the matrix $\mathbf{A}$ before diagonalization $\mathbf{A} \to \mathbf{A} - \lambda\mathbf{B}$, we can obtain the eigenvalues in the vicinity of some value λ.

The main task in the Lanczos procedure is to generate a set of orthogonal vectors $\mathbf{q}_i$ to construct the orthogonal matrix[1] $\mathbf{Q} = (\mathbf{q}_1, \mathbf{q}_2, \ldots, \mathbf{q}_m)$, where $m <$ rank$(\tilde{\mathbf{A}})$. Then, using an orthogonal similarity transformation to the matrix $\tilde{\mathbf{A}}$, we obtain the tridiagonal matrix $\mathbf{T}$

$$\mathbf{T} = \begin{pmatrix} \alpha_1 & \beta_1 & & & & \\ \beta_1 & \alpha_2 & \beta_2 & & & \\ & \beta_2 & \alpha_3 & \ddots & & \\ & & \ddots & \ddots & & \\ & & & & & \beta_m \\ & & & & \beta_m & \alpha_m \end{pmatrix}, \tag{A.2}$$

where $\tilde{\mathbf{A}}\mathbf{Q} = \mathbf{T}\mathbf{Q}$. The similarity transformation preserves the eigenvalues of $\tilde{\mathbf{A}}$, thus, the eigenvalues of $\tilde{\mathbf{A}}$ can be computed from $\mathbf{T}$.

[1] Orthogonal with respect to $\mathbf{B}$, i.e., $\mathbf{Q}^t\mathbf{B}\mathbf{Q} = \mathbb{1}$.

The matrix elements α_i and β_i, and the vectors $\mathbf{q}_i$ are given by iterative relations [142, 144]

$$\begin{aligned} \alpha_i &= \mathbf{q}_i^t \mathbf{B} \tilde{\mathbf{A}} \mathbf{q}_i \,, \\ \beta_i &= ||\mathbf{r}_i^t \mathbf{B} \mathbf{r}_{i+1}|| \,, \\ \mathbf{q}_{i+1} &= \frac{1}{\beta_{i+1}} \mathbf{r}_{i+1} \,, \end{aligned} \tag{A.3}$$

where $\mathbf{r}_{i+1} = \tilde{\mathbf{A}}\mathbf{q}_i - \alpha_i \mathbf{q}_i - \beta_{i-1}\mathbf{q}_{i-1}$.

From these relations we note that the matrix $\tilde{\mathbf{A}}$ appears only in products of the type $\tilde{\mathbf{A}}\mathbf{q}$. It is therefore unnecessary to invert $\mathbf{A}$ for its calculation. Instead, using LL^t factorization of $\mathbf{A}$ [145] the vector $\mathbf{y} = \tilde{\mathbf{A}}\mathbf{q} = \mathbf{A}^{-1}\mathbf{B}\mathbf{q}$ can be found solving the linear system of equations $\mathbf{A}\mathbf{y} = \mathbf{B}\mathbf{y}$ by backward substitution [145]. Thus, we have the following algorithm:

1. The LL^t factorization of $\mathbf{A}$.
2. m iterations of the recursive expressions (A.3) in order to obtain $\mathbf{T}$.
3. Diagonalization of $\mathbf{T}$, which can be achieved by standard diagonalization routines like the QR-decomposition [145].

A.2 Electronic density in configuration space

With the help of the projector (2.8), the electronic density in configuration space is given by [146]

$$\begin{aligned} |\phi_E(\vec{r})|^2 &= \langle \vec{r}|\phi_E\rangle\langle\phi_E|\vec{r}\rangle \,, \\ &= \frac{1}{\pi}\mathrm{Im}\sum_i \frac{\langle\vec{r}|R(-\theta)|\Psi_{i,\theta}\rangle\langle\overline{\Psi_{i,\theta}}|R(\theta)|\vec{r}\rangle}{E_{i,\theta}-E} \,, \\ &= \frac{1}{\pi}\mathrm{Im}\sum_i \frac{\langle\vec{r}|R(-\theta)|\Psi_{i,\theta}\rangle^2}{E_{i,\theta}-E} \,, \end{aligned} \tag{A.4}$$

where $\vec{r}$ represents the coordinates of both electrons.

In the single pole approximation, valid when a long-lived isolated resonance $|\Psi_{i,\theta}\rangle$ with $E_{i,\theta} \simeq E$ and $|\mathrm{Re}\, E_{i,\theta} - \mathrm{Re}\, E_{j,\theta}| \gg |E_{i,\theta} - E|$, $\forall j \neq i$, gives the dominant contribution to the sum in (A.4), the electronic probability density reads

$$|\phi_E(\vec{r})|^2 \simeq \frac{1}{\pi|\mathrm{Im}\, E_{i,\theta}|}\mathrm{Re}\,\langle\vec{r}|R(-\theta)|\Psi_{i,\theta}\rangle^2 \,. \tag{A.5}$$

• *Planar helium.*
In the planar case, the expression for $\langle\vec{r}|R(-\theta)|\Psi_{i,\theta}\rangle$ in the basis (2.24) writes

$$\langle\vec{r}|R(-\theta)|\Psi_{i,\theta}\rangle = \sum_{n_1,n_2,n_3,n_4} \langle\vec{r}|n_1n_2n_3n_4\rangle^{+\epsilon_x\ +\epsilon_x}\langle n_1n_2n_3n_4|R(-\theta)|\Psi_{i,\theta}\rangle\,. \tag{A.6}$$

By virtue of definitions (2.23) and (2.24), the expression for the basis states $|n_1n_2n_3n_4\rangle^{+\epsilon_x}$ in the coordinate representation is derived in terms of the product states $|n_1n_2n_3n_4\rangle$. Therefore, it is necessary the evaluation of $\langle\vec{r}|n_1n_2n_3n_4\rangle = \langle x_+,y_+|n_1n_2\rangle\langle x_-,y_-|n_3n_4\rangle$, where [38]

$$\langle x_+,y_+|n_1n_2\rangle = \sqrt{\frac{n_+!}{\pi(n_++m_+)!}}\,e^{\mathrm{i}m_+\varphi_+}r_+^{m_+}e^{-r_+^2/2}L_{n_+}^{(m_+)}(r_+^2)\,, \tag{A.7}$$

with $n_+ = \min\{n_1,n_2\}$, $m_+ = |n_1-n_2|$, $L_n^{(m)}(r)$ the generalized Laguerre polynomial [89] and (r_+,φ_+) the polar transformation of the coordinates (x_+,y_+). The expression for $\langle x_-,y_-|n_3n_4\rangle$ has the same form.

The complex rotation operator $R(\theta)$ can be expressed as a product of two rotation operators $R_+(\theta)$ and $R_-(\theta)$, acting on the spaces (x_+,y_+) and (x_-,y_-), respectively. Thus, $\langle n_1n_2n_3n_4|R(-\theta)|n_1'n_2'n_3'n_4'\rangle = \langle n_1n_2|R_+(-\theta)|n_1'n_2'\rangle\langle n_3n_4|R_-(-\theta)|n_3'n_4'\rangle$, where [88]

$$\begin{aligned}\langle n_1n_2|R_+(-\theta)|n_1'n_2'\rangle = (-1)^{n_+'}&\sqrt{\begin{pmatrix} n_++m_+ \\ n_+\end{pmatrix}\begin{pmatrix} n_+'+m_+ \\ n_+'\end{pmatrix}}\mathrm{i}^{n_++n_p'}(\sin\theta)^{n_++n_p'}\\ &\times(\cos\theta)^{-(n_++n_+'+m_++1)}F\left(-n_+,-n_+',m_++1;-\frac{1}{\sin^2\theta}\right)\delta_{m_+,m_+'}\,,\end{aligned} \tag{A.8}$$

with $F(a,b,c;x)$ the hypergeometric function [89] (which reduces to a polynomial here). The matrix elements $\langle n_3n_4|R_-(-\theta)|n_3'n_4'\rangle$ have a similar expression.

• *Three-dimensional helium.*
The evaluation of $\langle\vec{r}|R(-\theta)|\Psi_{i,\theta}\rangle$ in the basis of the expansion (2.29) requires the use of complex backscaling, in which the complex rotation operator $R(\theta)$ acts on the basis. The calculations involving Coulomb-Sturmian functions with complex arguments are obtained by means of the recursion formula

$$\begin{aligned}\sqrt{n(n+l-1)(n+l)}S_{n,l}^{(\kappa)}(r) - 2\sqrt{n-1}(n-1-\kappa r)S_{n-1,l}^{(\kappa)}(r)\\ +\sqrt{(n-2)(n-l-2)(n+l-1)}S_{n-2,l}^{(\kappa)}(r) = 0\,,\end{aligned} \tag{A.9}$$

which is based on a recurrence relation for Kummer's functions [70, 71, 89].

A.3 Husimi distributions

For the study of the FPC, the projection of the electronic density of a quantum state $|\phi_E\rangle$ is given by the Husimi function [37, 147]

$$\begin{aligned} W_{\phi_E}(q,p) &= |\langle\phi_{q,p}|\phi_E\rangle|^2\,, \\ &= \int d\vec{r}\,d\vec{r}\,'\,\phi^*_{q,p}(\vec{r})\phi_{q,p}(\vec{r}\,')\langle\vec{r}|\phi_E\rangle\langle\phi_E|\vec{r}\,'\rangle\,, \end{aligned} \tag{A.10}$$

with $\phi_{q,p}$ the modified coherent state

$$\phi_{q,p}(\vec{r}) = \exp\left(-\frac{1}{2}\omega_s(x_1-q)^2 - ix_1p\right)\delta(x_2-x_2^0)\delta(y_1)\delta(z_1)\delta(y_2)\delta(z_2)\,, \tag{A.11}$$

centered at the point (p,q) in the phase space, where $x_0 \simeq 0$ and $\omega_s = \omega_I = 0.3(N-1/2)^{-3}$, i.e., the intrinsic frequency of the FPC.

In the single pole approximation and using the projector (2.8), the expression (A.10) writes

$$W_{\phi_E}(q,p) \simeq \frac{1}{\pi|\mathrm{Im}\,E_{j,\theta}|}\mathrm{Re}\int d\vec{r}\,\phi_{q,p}(\vec{r})\langle\vec{r}|R(-\theta)|\Psi_{j,\theta}\rangle\int d\vec{r}\,'\,\phi^*_{q,p}(\vec{r}\,')\langle\vec{r}\,'|R(-\theta)|\Psi_{j,\theta}\rangle\,. \tag{A.12}$$

A.4 Expectation value of $\cos\theta_{12}$

The expression for $\langle\cos\theta_{12}\rangle$ is given by

$$\langle\phi_E|\cos\theta_{12}|\phi_E\rangle = \int d\vec{r}\,\langle\vec{r}\,|\phi_E\rangle\langle\phi_E|\vec{r}\,\rangle\cos\theta_{12}\,. \tag{A.13}$$

Using the projector (2.8) and the single pole approximation, Eq. (A.13) reads

$$\langle\phi_E|\cos\theta_{12}|\phi_E\rangle \simeq \frac{1}{\pi|\mathrm{Im}\,E_{j,\theta}|}\mathrm{Re}\langle\overline{\Psi_{j,\theta}}|\cos\theta_{12}|\Psi_{j,\theta}\rangle\,. \tag{A.14}$$

In the planar case, the expression of $\cos\theta_{12}$ in Eq. (A.14) writes as polynomial function of the parabolic coordinates and can be represented in terms of the circular operators (2.17), resulting in 2088 monomial terms associated with 171 selection rules in the Fock basis [38], while for the three-dimensional helium, $\cos\theta_{12}$ is written in terms of spherical harmonics $Y_{l,m}(\hat{r})$, leading to an easily accessible matrix representation in terms of overlap integrals of Coulomb-Sturmian functions [71].

Appendix B

B.1 Unnatural parity states

In two-electron atomic systems it is possible to identify states for which the individual angular momenta of the electrons satisfy $(-1)^{l_1+l_2} = (-1)^L$ for natural parity states and $(-1)^{l_1+l_2} = (-1)^{L+1}$ for unnatural parity states, where L represents the total angular momentum.

As a consequence of the angular momentum and parity conservation, unnatural parity states below the $N = 2$ ionization threshold do not interact with the adjacent continuum. Nevertheless, by including relativistic interactions, these states acquire an autoionization lifetime which is several orders of magnitude longer than the mean radiative lifetime of the allowed electric dipole transitions [148]. Accurate calculations of the energy and lifetimes of unnatural parity states in helium and helium-like ions have been performed in several investigations [26, 27, 149–152].

The approach described in Section 2.3 is applied to the computation of doubly excited unnatural parity states of Li^+ for total angular momentum $L = 2, \ldots, 5$. Table B.1 shows results for $^3\mathrm{P}^\mathrm{e}$ states compared to reference data. In Tables B.2 and B.2, we present so far unreported spectral data for $^3\mathrm{F}^\mathrm{e}$, $^3\mathrm{G}^\mathrm{e}$ and $^3\mathrm{H}^\mathrm{e}$ states below the third and fourth ionization thresholds, respectively.

The energies and decay rates have been obtained after diagonalization of (2.45). In the basis expansion, we have considered 10 angular configurations (l_1, l_2), each one with 8 sets $\{\kappa_{1s}, N_{1s}^{\min}, N_{1s}^{\max}, \kappa_{2s}, N_{2s}^{\min}, N_{2s}^{\max}\}$. The results presented have been tested with respect to variation of the above parameters, for complex rotation angles $\theta = 0.15, 0.25,$ and 0.30. Only converged digits are presented.

B.2 Oscillator strengths

In this section, we calculate some oscillator strengths for the transitions between bound states in three-dimensional helium. These computations involve the dipole elements which are important in the construction of the matrix representation of the time-dependent Schrödinger equation in Section 2.4.2.

	This work		Ho and Bhatia [153]	
	$-E$ [a.u.]	$\Gamma/2$ [a.u.]	$-E$ [a.u.]	$\Gamma/2$ [a.u.]
$N=3$	0.831 281 3	0.002 664 4	0.831 281 4	0.002 664 4
	0.755 785 7	0.000 034 6	0.755 788 8	0.000 035 3
	0.661 038 5	0.001 291 7	0.661 038 6	0.001 291 7
	0.625 089 1	0.000 010 9	0.625 090 4	0.000 011 0
	0.598 310 3	0.000 620 5	0.598 105 0	0.000 620 5
	0.579 630 4	0.000 005 9	0.579 631 0	0.000 006 0
	0.566 065 5	0.000 329 8	0.566 065 0	0.000 329 5
	0.555 328 8	0.000 003 4	0.555 329 0	0.000 003 5
$N=4$	0.476 220 4	0.002 121 1	0.476 219 0	0.002 119 9
	0.409 147 0	0.000 048 7	0.409 139 5	0.000 051 7
	0.392 434 5	0.001 361 2	0.392 434 5	0.001 361 0
	0.374 205 2	0.001 633 5	0.374 205 2	0.001 633 5
	0.355 145 1	0.000 730 4	0.355 145 2	0.000 730 5
	0.355 043 1	0.000 020 1	0.355 042 5	0.000 021 2
	0.344 043 9	0.000 933 5	0.344 044 0	0.000 933 5
	0.333 717 3	0.000 389 6	0.333 720 0	0.000 391 5
	0.332 939 9	0.000 013 4	0.332 939 5	0.000 014 0
	0.326 714 9	0.000 535 9	0.326 714 5	0.000 536 0

Table B.1.: Energies and decay rates of doubly excited $^3\mathrm{P^e}$ states of Li^+ with unnatural parity. Reference data given in Ry were converted to a.u. dividing by 2.

The oscillator strengths in dipole approximation and length gauge are defined as [154]

$$f_{nm} = C(E_n - E_m)\,|\langle\psi_n|z_1 + z_2|\psi_m\rangle|^2 \tag{B.1}$$

where the constant C is equal to 2 and 5/3 respectively for $\mathrm{S} \to \mathrm{P}$ and $\mathrm{P} \to \mathrm{D}$ transitions from an initial state $|\psi_m\rangle$ to a final state $|\psi_n\rangle$.

Using Eq. (B.1) we calculate oscillator strengths for $\mathrm{S} \to \mathrm{P}$ and $\mathrm{P} \to \mathrm{D}$ transitions in singlet and triplet states. The obtained values are presented in Table B.4. The agreement between our results and the reference data guarantee the accurate computation of dipole matrix elements used in Section 4.3 to describe driven FPS and NDWP in 3D helium.

	$-E$ [a.u.]	$\Gamma/2$ [a.u.]	$-E$ [a.u.]	$\Gamma/2$ [a.u.]	$-E$ [a.u.]	$\Gamma/2$ [a.u.]
$L = 3$	0.646 515	0.000 278	0.533 968 2	0.000 022 9	0.516 434 9	0.000 000 1
	0.635 429	0.000 320	0.532 422 8	0.000 041 5	0.514 686 7	0.000 005 9
	0.591 186	0.000 121	0.530 988 4	0.000 000 3	0.514 239 7	0.000 011 6
	0.584 904	0.000 176	0.526 595 3	0.000 015 4	0.513 817 5	0.000 000 1
	0.578 735	0.000 001	0.525 517 1	0.000 028 6	0.512 461 1	0.000 004 8
	0.562 034	0.000 062	0.524 513 0	0.000 000 2	0.512 110 7	0.000 009 1
	0.558 341	0.000 102	0.521 384 7	0.000 010 9	0.511 778 8	0.000 000 1
	0.554 876	0.000 001	0.520 604	0.000 021	0.510 705 2	0.000 004 2
	0.544 885 7	0.000 036 3	0.519 872 7	0.000 000 2	0.510 425 7	0.000 007 9
	0.542 564 9	0.000 063 1	0.517 567	0.000 008	0.510 160 1	0.000 000 1
	0.540 410 5	0.000 000 3	0.516 983 5	0.000 015 3		
$L = 4$	0.630 88	0.000 07	0.531 976 9	0.000 013 9	0.516 431 3	0.000 000 1
	0.584 192	0.000 002	0.530 987 1	0.000 000 2	0.514 194 0	0.000 000 8
	0.582 835	0.000 050	0.525 413 0	0.000 001 5	0.514 112 0	0.000 004 1
	0.557 980	0.000 003	0.525 208 3	0.000 009 8	0.513 814 1	0.000 000 1
	0.557 220	0.000 032	0.524 509 6	0.000 000 1	0.512 074 4	0.000 000 6
	0.554 897 2	0.000 000 2	0.520 526 7	0.000 001 2	0.512 011	0.000 003
	0.542 345 3	0.000 002 2	0.520 380 5	0.000 007 2	0.511 775 8	0.000 000 1
	0.541 884 6	0.000 020 6	0.519 868 9	0.000 000 1	0.510 396 4	0.000 000 5
	0.540 415 2	0.000 000 2	0.516 925	0.000 001	0.510 345 7	0.000 002 6
	0.532 275 8	0.000 001 8	0.516 817 0	0.000 005 3	0.510 157 4	0.000 000 1
$L = 5$	0.583 166	0.000 005	0.525 306 3	0.000 001 7	0.514 155 7	0.000 000 8
	0.557 488	0.000 004	0.525 040 4	0.000 000 3	0.514 034 82	0.000 000 14
	0.556 770 9	0.000 000 4	0.524 543 44	0.000 000 05	0.513 827 70	0.000 000 03
	0.542 074 4	0.000 003 1	0.520 453 6	0.000 001 3	0.512 045 3	0.000 000 6
	0.541 569 5	0.000 000 4	0.520 253 5	0.000 000 2	0.511 948 90	0.000 000 12
	0.540 492 7	0.000 000 1	0.519 893 08	0.000 000 05	0.511 786 37	0.000 000 02
	0.532 111 7	0.000 002 3	0.516 872 8	0.000 000 9	0.510 373 76	0.000 000 51
	0.531 749 9	0.000 000 3	0.516 718 80	0.000 000 18	0.510 295 70	0.000 000 09
	0.531 036 88	0.000 000 04	0.516 449 10	0.000 000 03	0.510 165 81	0.000 000 02

Table B.2.: Energies and decay rates for $^3\mathrm{F}^\mathrm{e}$, $^3\mathrm{G}^\mathrm{e}$ and $^3\mathrm{H}^\mathrm{e}$ states of Li^+ below the $N = 3$ ionization threshold.

	$-E$ [a.u.]	$\Gamma/2$ [a.u.]	$-E$ [a.u.]	$\Gamma/2$ [a.u.]	$-E$ [a.u.]	$\Gamma/2$ [a.u.]
$L = 3$	0.389 267	0.000 027	0.330 619	0.000 017	0.309 706 8	0.000 016 6
	0.386 783	0.000 727	0.327 348	0.000 413	0.308 596 0	0.000 125 1
	0.376 030	0.001 277	0.324 806	0.000 070	0.307 310	0.000 022
	0.368 19	0.000 24	0.322 130	0.000 113	0.306 043 6	0.000 039 7
	0.361 82	0.000 25	0.320 167	0.000 072	0.305 127 4	0.000 044 8
	0.351 930	0.000 366	0.319 066 9	0.000 105 5	0.304 920 8	0.000 003 2
	0.351 203	0.000 035	0.318 024 7	0.000 011 9	0.303 615 3	0.000 096 4
	0.345 115	0.000 725	0.316 139	0.000 236	0.303 024 7	0.000 161 5
	0.340 100	0.000 119	0.314 395	0.000 042	0.302 311	0.000 052
	0.336 865	0.000 169	0.312 594	0.000 075	0.301 374	0.000 062
	0.333 57	0.000 09	0.311 293	0.000 058		
	0.331 706	0.000 199	0.310 766 1	0.000 044 3		
$L = 4$	0.389 660 3	0.000 044 2	0.322 366	0.000 009	0.306 117	0.000 008
	0.377 677 1	0.000 404 7	0.321 921	0.000 053	0.305 936	0.000 021
	0.370 612	0.000 952	0.320 533	0.000 018	0.305 256	0.000 015
	0.360 964	0.000 096	0.318 340 7	0.000 018 6	0.303 61	0.000 09
	0.351 741 0	0.000 037 3	0.316 314 3	0.000 084 3	0.302 806	0.000 088
	0.346 089 1	0.000 230 2	0.314 794	0.000 197	0.301 391	0.000 013
	0.341 907	0.000 562	0.312 727	0.000 009	0.301 291	0.000 053
	0.337 213	0.000 010	0.312 451	0.000 037	0.300 758	0.000 012
	0.336 490	0.000 075	0.311 503	0.000 017	0.299 742	0.000 091
	0.331 041	0.000 027	0.309 960	0.000 016	0.299 008	0.000 057
	0.327 809 8	0.000 135 6	0.308 616	0.000 055		
	0.325 340	0.000 332	0.307 633	0.000 115		
$L = 5$	0.375 8	0.001 6	0.328 12	0.000 36	0.314 596	0.000 043
	0.366 57	0.000 55	0.325 251	0.000 059	0.313 783	0.000 157
	0.346 12	0.000 72	0.323 888	0.000 242	0.312 53	0.000 05
	0.342 03	0.000 07	0.322 07	0.000 05	0.312 38	0.000 01
	0.339 62	0.000 37	0.321 890	0.000 007		
	0.336 72	0.000 06	0.316 606	0.000 199		

Table B.3.: Energies and decay rates for $^3\mathrm{F}^\mathrm{e}$, $^3\mathrm{G}^\mathrm{e}$ and $^3\mathrm{H}^\mathrm{e}$ states of Li^+ below the $N = 4$ ionization threshold.

		$m\,\mathrm{S} \to n\,\mathrm{P}$					$m\,\mathrm{P} \to n\,\mathrm{D}$		
m	n	This work	(a)	(b)	m	n	This work	(a)	(b)
				Singlet states					
1	2	0.276 177	0.276 17	0.276 164 7	2	2	0.539 086 6	0.539 1	0.539 086 1
	3	0.073 436	0.073 43	0.073 434 9		3	0.064 461 0	0.064 47	0.064 461 2
	4	0.029 863 5	0.029 861	0.029 862 9		4	0.025 768 8	0.025 76	0.025 768 9
	5	0.015 039 6	0.015 039	0.015 039 3		5	0.012 490 54	0.012 493	0.012 490 6
	6	0.008 627 8	0.008 627	0.008 627 7		6	0.006 982 15	0.006 981	0.006 982 2
2	2	0.376 392	0.376 48	0.376 440 3	3	2	0.208 536 1	0.208 52	0.208 535 9
	3	0.151 370	0.151 35	0.151 341 7		3	0.890 851 9	0.891 0	0.890 851 3
	4	0.049 161 8	0.049 15	0.049 154 9		4	0.050 083 1	0.050 06	0.050 083 3
	5	0.022 340 5	0.022 34	0.022 337 7		5	0.022 914 04	0.022 91	0.022 914 1
	6	0.012 135 4	0.012 136	0.012 134 0		6	0.011 993 32	0.011 985	0.011 993 3
				Triplet states					
2	3	0.710 181	0.710 17	0.710 164 1	2	3	0.610 225 6	0.610 24	0.610 225 2
	4	0.120 269 5	0.120 27	0.120 270 4		4	0.122 846 95	0.122 850	0.122 846 9
	5	0.043 256 83	0.043 28	0.043 257 6		5	0.047 007 10	0.047 0	0.047 007 1
	6	0.020 947 99	0.020 952	0.020 948 5		6	0.023 469 23	0.023 472	0.023 469 2
	7	0.011 896 67		0.011 897 0		7	0.013 563 82		0.013 563 8
3	3	0.021 162	0.021 1	0.021 140 1	3	3	0.112 099 7	0.112 2	0.112 100 4
	4	0.648 135 6	0.648 10	0.648 104 9		4	0.477 594 5	0.477 60	0.477 593 8
	5	0.141 304 7	0.141 32	0.141 302 7		5	0.124 553 32	0.124 531	0.124 553 2
	6	0.056 276 78	0.056 26	0.056 276 6		6	0.053 008 81	0.052 98	0.053 009 3
	7	0.028 896 00		0.028 896 1		7	0.028 158 71		0.028 158 7

Table B.4.: Helium oscillator strengths (in atomic units) for the selected transitions between the bound states $|\psi_m\rangle$ and $|\psi_n\rangle$. Comparisons are made to the results reported by (a) Cann and Thakkar [155], and (b) Drake [156].

Bibliography

[1] M. Ossiander *et al.*, Nature Phys. **13**, 280 (2017).

[2] D. Busto *et al.*, J. Phys. B: Atom. Mol. Opt. Phys. **51**, 044002 (2018).

[3] S. Beaulieu *et al.*, Science **358**, 1288 (2017).

[4] M. Nisoli, P. D. F. Calegari, A. Palacios, and F. Martín, Chem. Rev. **117**, 10760 (2017).

[5] M. Klinker *et al.*, Chem. Phys. Lett. **9**, 756 (2018).

[6] A. Schiffrin *et al.*, Nature **493**, 70 (2013).

[7] M. T. Hassan *et al.*, Nature **530**, 66 (2016).

[8] M. Schultze, Laser Science (pp. LW5F-1). Optical Society of America (2017).

[9] R. Pazourek, S. Nagele, and J. Burgdörfer, Rev. Mod. Phys. **87**, 765 (2015).

[10] F. Calegari *et al.*, Journal of Physics B: Atomic, Molecular and Optical Physics **49**, 062001 (2016).

[11] C. Ott *et al.*, Nature **516**, 374 (2014).

[12] A. Einstein, Verh. Dtsch. Phys. Ges. **19**, 82 (1917).

[13] K. Richter and D. Wintgen, J. Phys. B **26**, 3719 (1993).

[14] G. Tanner, K. Richter, and J. M. Rost, Rev. Mod. Phys. **72**, 497 (2000).

[15] N. Bohr, Phil. Mag. **26:1**, (1913).

[16] N. Bohr, Phil. Mag. **26:476**, (1913).

[17] M. C. Gutzwiller, J. Math. Phys. **8**, 1979 (1967).

[18] M. C. Gutzwiller, J. Math. Phys. **12**, 343 (1971).

[19] J. G. Leopold and I. C. Percival, J. Phys. B **13**, 1037 (1980).

[20] G. S. Ezra, K. Richter, G. Tanner, and D. Wintgen, J. Phys. B **24**, L413 (1991).

[21] D. Wintgen, K. Richter, and G. Tanner, Chaos **2**, 19 (1992).

[22] T. Grosges, B. Piraux, and H. Bachau, Phys. Rev. A **60**, 1371 (1999).

[23] B. Piraux, J. Bauer, S. Laulan, and H. Bachau, Phys. Rev. A **26**, 7 (2003).

[24] L. Argenti, Atomic Data and Nuclear Data Tables **94**, 903 (2008).

[25] J. Eiglsperger, B. Piraux, and J. Madroñero, Phys. Rev. A **80**, 022511 (2009).

[26] J. Eiglsperger, B. Piraux, and J. Madroñero, Phys. Rev. A **81**, 042527 (2010).

[27] J. Eiglsperger, B. Piraux, and J. Madroñero, Phys. Rev. A **81**, 042528 (2010).

[28] L. Malegat, H. Bachau, A. Hamido, and B. Piraux, J. Phys. B: Atom. Mol. Opt. Phys. **43**, 245601 (2010).

[29] J. Eiglsperger, M. Schönwetter, B. Piraux, and J. Madroñero, Atomic Data and Nuclear Data Tables **98**, 120 (2012).

[30] R. P. Madden and K. Codling, Phys. Rev. Lett. **10**, 516 (1963).

[31] C. W. Byun, N. N. Choi, M.-H. Lee, and G. Tanner, Phys. Rev. Lett. **98**, 113001 (2007).

[32] T. Ericson, Phys. Rev. Lett. **5**, 430 (1960).

[33] T. Ericson, Annals of Physics **23**, 390 (1963).

[34] K. Richter and D. Wintgen, Phys. Rev. Lett. **65**, 1965 (1990).

[35] K. Richter, J. S. Briggs, D. Wintgen, and E. A. Solovev, J. Phys. B **25**, 3929 (1992).

[36] P. Schlagheck and A. Buchleitner, Europhys. Lett. **46**, 24 (1999).

[37] P. Schlagheck and A. Buchleitner, Eur. Phys. J. D **22**, 401 (2003).

[38] J. Madroñero, Dissertation, Ludwig-Maximilians-Universität München, 2004.

[39] J. Madroñero and A. Buchleitner, Phys. Rev. A **77**, 053402 (2008).

[40] A. Buchleitner, D. Delande, and J. Zakrzewski, Phys. Rep. **368**, 409 (2002).

[41] J. Itatani *et al.*, Nature **432**, 867 (2004).

[42] S. Haessler *et al.*, Nature Phys. **6**, 200 (2010).

[43] P. Agostini and L. F. DiMauro, Rep. Prog. Phys. **67**, 813 (2004).

[44] K. L. Ishikawa, L. Kenichi, and T. Sato, IEEE Q. Electr. **21**, 1 (2015).

[45] K. J. Schafer, B. Yang, L. F. DiMauro, and K. C. Kulander, Phys. Rev. Lett. **70**, 1599 (1993).

[46] B. Yang *et al.*, Phys. Rev. A **71**, 3770 (1993).

[47] J. Parker, K. T. Taylor, C. W. Clark, and S. Blodgett-Ford, J. Phys. B: Atom. Mol. Opt. Phys. **29**, L33 (1996).

[48] E. S. Smyth, J. S. Parker, and K. Taylor, Comput. Phys. Commun. **114**, 1 (1998).

[49] J. Feist *et al.*, Phys. Rev. A **77**, 043420 (2008).

[50] A. Palacios, T. N. Rescigno, and C. W. McCurdy, Phys. Rev. A **79**, 033402 (2009).

[51] Z. Zhang *et al.*, Phys. Rev. A **84**, 043409 (2011).

[52] G. L. Kamta and A. F. Starace, Phys. Rev. Lett. **86**, 5687 (2001).

[53] G. L. Kamta and A. F. Starace, Phys. Rev. A **65**, 053418 (2002).

[54] E. Foumouo, G. L. Kamta, G. Edah, and B. Piraux, Phys. Rev. A **74**, 063409 (2006).

[55] L. A. A. Nikolopoulos and P. Lambropoulos, J. Phys. B **40**, 1347 (2007).

[56] E. Foumouo, P. Antoine, H. Bachau, and B. Piraux, New J. Phys. **10**, 025017 (2008).

[57] D. A. Varschalovich, A. N. Moskalev, and V. K. Khersonskii, *Quantum Theory of Angular Momentum* (World Scientific, Singapore, 2008).

[58] M. Rotenberg, Adv. At. Mol. Phys. **6**, 233 (1970).

[59] E. Huens, B. Piraux, A. Bugacov, and M. Gajda, Phys. Rev. A **55**, 2132 (1997).

[60] C. D. Boor, *A practical guide to splines* (Springer Verlag, New York, 1978).

[61] H. Bachau *et al.*, Rep. Prog. Phys. **64**, 1815 (2001).

[62] J. Caillat *et al.*, Phys. Rev. A **65**, 012712 (2005).

[63] T. T. Nguyen-Dang, M. Peters, S. M. Wang, and F. Dion, Chem. Phys. **336**, 71 (2009).

[64] T. T. Nguyen-Dang and J. Viau-Trudel, J. Chem. Phys. **139**, 244102 (2013).

[65] R. P. Miranda, A. J. Fisher, L. Stella, and A. P. Horsfield, J. Chem. Phys. **134**, 244101 (2011).

[66] T. Sato and K. L. Ishikawa, Phys. Rev. A **88**, 023402 (2013).

[67] T. Sato *et al.*, Phys. Rev. A **94**, 023405 (2016).

[68] M. G. Floquet, Annales de l'École Normale Supérieure **12**, 47 (1883).

[69] J. H. Shirley, Phys. Rev. **138**, B979 (1965).

[70] G. L. Kamta, Ph.D. thesis, Universite Nationale du Benin, 1999.

[71] J. Eiglsperger, Dissertation, Technische Universität München, 2010.

[72] B. H. Bransden, C. Joachain, and T. J. Plivier, *Physics of atoms and molecules* (Pearson Education, India, 2003).

[73] L. Hilico *et al.*, Phys. Rev. A **66**, 022101 (2002).

[74] D. R. Herrick and M. E. Kellman, Phys. Rev. A **21**, 418 (1980).

[75] D. R. Herrick and O. Sinanoğlu, Phys. Rev. A **11**, 97 (1975).

[76] D. Herrick, Adv. Chem. Phys. **52**, 1 (1983).

[77] M. E. Kellman and D. R. Herrick, Phys. Rev. A **22**, 1536 (1980).

[78] D. R. Herrick, M. E. Kellman, and R. D. Poliak, Phys. Rev. A **22**, 1517 (1980).

[79] A. Bürgers, D. Wintgen, and J. M. Rost, J. Phys. B **28**, 3163 (1995).

[80] O. Sinanoğlu and D. Herrick, J. Chem. Phys. **62**, 886 (1975).

[81] E. Balslev and J. M. Combes, Commun. Math. Phys. **22**, 280 (1971).

[82] Y. K. Ho, Phys. Rep. **99**, 1 (1983).

[83] W. P. Reinhardt, An. Rev. Phys. Chem. **33**, 223 (1982).

[84] B. Grémaud, Ph.D. thesis, Université Pierre et Marie Curie (Paris 6), 1997.

[85] A. Buchleitner, D. Delande, and J. Gay, J. Opt. Soc. Am. B **12**, 505 (1994).

[86] A. Buchleitner, Ph.D. thesis, Université Pierre et Marie Curie (Paris 6), 1993.

[87] R. Loudon, *The quantum theory of light* (Clarendon Press, Oxford, 1984).

[88] D. Delande, *Atomes de Rydberg en champ statiques intenses* (Thèse d'état, Université Pierre et Marie Curie (Paris 6), Paris, 1988).

[89] M. Abramowitz and I. Stegun, *Handbook of mathematical functions* (Dover Publications, Inc., New York, 1972).

[90] J. Zamastil *et al.*, J. Math. Phys. **45**, 2674 (2004).

[91] J. Zamastil, F. Vinette, and M. Simanek, Phys. Rev. A **75**, 022506 (2007).

[92] T. Kato, Commun. Appl. Math. **10**, 151 (1957).

[93] C. C. J. Roothaan and A. W. Weiss, Rev. Mod. Phys. **32**, 194 (1960).

[94] D. Delande and J. Zakrzewski, Phys. Rev. A **58**, 466 (1998).

[95] J. Madroñero *et al.*, Adv. At. Mol. Opt. Phys. **53**, 33 (2006).

[96] M. C. Tichy, F. Mintert, and A. Buchleitner, J. Phys. B **44**, 192001 (2011).

[97] O. Osenda and P. Serra, Phys. Rev. A **75**, 042331 (2007).

[98] M. A. Nielsen and I. L. Chuang, *Quantum computation and quantum information* (Cambridge University Press, Cambridge, 2000).

[99] D. S. Naik *et al.*, Phys. Rev. Lett. **84**, 4733 (2000).

[100] M.-J. Zhao, S.-M. Fei, and X. Li-Jost, Phys. Rev. A **85**, 054301 (2012).

[101] J. Schliemann *et al.*, Phys. Rev. A **64**, 022303 (2001).

[102] J. Naudts and T. Verhulst, Phys. Rev. A **75**, 062104 (2007).

[103] A. R. Plastino, D. Manzano, and J. S. Dehesa, Europhys. Lett. **86**, 20005 (2009).

[104] L. Amico, L. Fazio, A. Osterloh, and V. Vedral, Rev. Mod. Phys. **80**, 517 (2008).

[105] T. Hahn, Comput. Phys. Commun. **168**, 78 (2005).

[106] T. Hahn, Comput. Phys. Commun. **176**, 712 (2007).

[107] G. P. Lepage, J. Comp. Phys. **27**, 192 (1978).

[108] P. Schlagheck, Ph.D. thesis, Technische Universität München, 1999.

[109] P. Kustaanheimo and E. Stiefel, J. Math. Bd **218**, 27 (1965).

[110] S. J. Aarseth and K. Zare, Celest. Mech. **10**, 185 (1974).

[111] A. Lichtenberg and M. A. Lieberman, *Regular and Stochastic Motion* (Springer-Verlag, New York, 1983).

[112] V. N. Ostrovsky and N. V. Prudov, J. Phys. B **28**, 4435 (1995).

[113] J. Madroñero *et al.*, Europhys. Lett. **70**, 183 (2005).

[114] U. Eichmann, V. Lange, and W. Sandner, Phys. Rev. A **64**, 274 (1990).

[115] K. D. Heber *et al.*, Phys. Rev. A **56**, 1255 (1997).

[116] P. Camus *et al.*, Phys. Rev. A **62**, 2365 (1989).

[117] J. Eiglsperger and J. Madroñero, Phys. Rev. A **80**, 022512 (2009).

[118] Y. H. Jiang *et al.*, Phys. Rev. A **78**, 021401 (2008).

[119] H. Friedrich and J. Trost, Phys. Rep. **397**, 359 (2004).

[120] H. Friedrich, *Theoretical atomic physics* (Springer, Berlin, 2006).

[121] J. Madroñero *et al.*, Europhys. Lett. **70**, 183 (2005).

[122] R. P. Feynman, Phys. Rev. **56**, 340 (1939).

[123] H. Hellmann, *Hans Hellmann: Einführung in Die Quantenchemie: Mit Biografischen Notizen von Hans Hellmann* (Springer-Verlag, New York, 2015).

[124] I. Guzmán, Undergraduate thesis, Universidad del Valle, 2015.

[125] A. González, I. Guzmán, and J. Madroñero, J. Phys. Conf. Ser. **635**, 092088 (2015).

[126] J. Pipek and I. Nagy, Phys. Rev. A **79**, 052501 (2009).

[127] A. Ferrón, O. Osenda, and P. Serra, Phys. Rev. A **79**, 032509 (2009).

[128] R. J. Yáñez, A. R. Plastino, and J. S. Dehesa, Eur. Phys. J.D **56**, 141 (2010).

[129] D. Manzano, A. R. Plastino, J. S. Dehesa, and T. Koga, J. Phys. A **43**, 275301 (2010).

[130] P. A. Bouvrie *et al.*, Eur. Phys. J.D **66**, 15 (2012).

[131] S. Schröter, H. Friedrich, and J. Madroñero, Phys. Rev. A **87**, 042507 (2013).

[132] J. S. Dehesa *et al.*, J. Phys. B **45**, 015504 (2012).

[133] G. Benenti, S. Siccardi, and G. Strini, Eur. Phys. J.D **67**, 83 (2013).

[134] Y. C. Lin, C. Y. Lin, and Y. K. Ho, Phys. Rev. A **87**, 022316 (2013).

[135] J. P. Restrepo Cuartas and J. L. Sanz-Vicario, Phys. Rev. A **91**, 052301 (2015).

[136] A. Kuroś, P. Kościk, and J. K. Saha, Few-body Syst. **57.12**, 1147 (2016).

[137] S. Sauer, F. Mintert, C. Gneiting, and A. Buchleitner, J. Phys. B: Atom. Mol. Opt. Phys. **45**, 154011 (2012).

[138] J. Madroñero and B. Piraux, Phys. Rev. A **80**, 033409 (2009).

[139] A. Hamido *et al.*, Phys. Rev. A **84**, 013422 (2011).

[140] A. L. Frapiccini *et al.*, Phys. Rev. A **89**, 023418 (2014).

[141] C. Lanczos, J. Res. Natl. Bur. Stand. **45**, 225 (1950).

[142] B. N. Parlett and D. S. Scott, Math. Comput. **33**, 217 (1979).

[143] T. Ericsson and A. Ruhe, Math. Comput. **35**, 1251 (1980).

[144] A. Krug, Dissertation, Ludwig-Maximilians-Universität München, 2001.

[145] G. H. Golub and C. F. Loan, *Matrix Computations* (The John Hopkins University Press, Baltimore, Maryland, 1996).

[146] A. Buchleitner, B. Grémaud, and D. Delande, J. Phys. B **27**, 2663 (1994).

[147] K. Richter, Ph.D. thesis, Albert-Ludwigs-Universität Freiburg, 1991.

[148] J. Eiglsperger, B. Piraux, and J. Madroñero, Phys. Rev. A **81**, 042527 (2010).

[149] J. K. Saha, S. Bhattacharyya, T. K. Mukherjee, and P. Mukherjee, J. Chem. Phys. **132**, 134107 (2010).

[150] Z. Jiang, S. Kar, and Y. K. Ho, Physika Scripta **85**, 065304 (2012).

[151] S. Kar, Y. Wang, W. Q. Li, and X. D. Sun, Few-body Syst. **56**, 651 (2015).

[152] S. Dutta, A. N. Sil, J. K. Saha, and T. K. Mukherjee, Int. J. Quantum Chem. **e25577**, (2017).

[153] Y. K. Ho and A. K. Bhatia, Phys. Rev. A **47**, 2628 (1993).

[154] H. A. Bethe and E. E. Salpeter, in *Handbuch der Physik*, edited by S. Flügge (Springer-Verlag, Berlin, 1957), Vol. XXXV, pp. 88–436.

[155] N. M. Cann and A. J. Thakkar, Phys. Rev. A **46**, 5397 (1992).

[156] G. W. F. Drake, *Springer handbook of atomic, molecular, and optical physics* (Springer, New York, 2006).